ARTICLE

Defect Engineering in Thermoelectric Materials: What Have we Learned?

vacaReceived 00th January 20xx,
Accepted 00th January 20xx

DOI: 10.1039/x0xx00000x

Yun Zheng,[a,b†] Tyler J. Slade,[c†] Lei Hu,[d] Xian Yi Tan,[d] Yubo Luo,[c,d] Zhong-Zhen Luo,[c,d] Jianwei Xu,[b*] Qingyu Yan,[d*] and Mercouri G. Kanatzidis [c*]

Thermoelectric energy conversion is an all solid-state technology that relies on exceptional semiconductor materials that are generally optimized through sophisticated strategies involving the engineering of defects in their structure. In this review, we summarize the recent advances of defect engineering to improve the thermoelectric (TE) performance and mechanical properties of inorganic materials. First, we introduce the various types of defects categorized by dimensionality, i.e. point defects (vacancies, interstitials, and antisites), dislocations, planar defects (twin boundaries, stacking faults and grain boundaries), and volume defects (precipitation and voids). Next, we discuss the advanced methods for characterizing defects in TE materials. Subsequently, we elaborate on the influences of defect engineering on the electrical and thermal transport properties as well as mechanical performance of TE materials. In the end, we discuss the outlook for the future development of defect engineering to further advance the TE field.

1. Introduction

Thermoelectric (TE) energy harvesting is among the most promising technologies for improving the management of energy produced from traditional fossil fuels and may aid in increasing global energy efficiency and reducing the emission of carbon dioxide. Based on the Seebeck effect, thermoelectric generators (TEG) hold promise for their ability to directly convert waste heat into useful electricity. Examples of current TEG applications include but are not limited to TEG appliances designed for areas with a shortage of electricity,[1] waste heat recovery from vehicles and cargo vessels,[2-5] power supplies for wireless sensors and wearable devices,[6, 7] and the radioisotope TEG adopted in spacecrafts by NASA.[8] The relatively niche market for TEG is mainly ascribed to the low TE energy conversion efficiency,[9] high cost of TE materials, and slow progress of reliable module development.[10] Therefore, it is essential to develop advanced-concepts, high-performance and reliable TE materials, as well as robust processing technologies to accelerate the pace of TEG applications.

The maximum power generation efficiency of a TE material, η, is defined by Equation 1,

$$\eta = \frac{T_H - T_C}{T_H}\left[\frac{\sqrt{1+ZT_{ave}}-1}{\sqrt{1+ZT_{ave}}+\frac{T_C}{T_H}}\right] \quad (1)$$

where T_H and T_C correspond to the temperatures of the hot and cold sides, respectively.[11] ZT_{ave} is the device figure of merit value between T_H and T_C, and the dimensionless figure of merit, ZT, is defined by, $ZT=S^2\sigma T/\kappa$, where S, σ, and κ are the Seebeck coefficient, electrical conductivity and thermal conductivity of a TE material at a specific temperature (T). Materials with high ZT values across the whole operating temperature range are required to ensure favorable output power for the TEG.[10] However, the adverse interdependence between the transport parameters (S, σ and κ) makes it difficult to improve any individual property without degrading the others.[12] Effective approaches to increase the ZT values center upon learning how to decrease this interdependence and target either to maximize the power factor ($PF=S^2\sigma$) or to decrease the thermal conductivity κ, which consists of both electronic (κ_e) and lattice (κ_L) contributions.

Recent years witnessed great successes in increasing the ZT values, from unity to over 2.0, by synergistic optimization of both electrical and thermal transport properties.[13] Strategies such as band structure engineering,[14] morphology manipulation,[15] discovery of materials with intrinsically low κ_L,[16] and defect engineering,[17] were successfully implemented, advancing the TE performance of materials. Band structure engineering is realized by controlling the alloying concentration or stoichiometry to tune the electronic band structure, energetically converge unique band extrema, or introduce resonant levels near the Fermi level. Typically, band

[a.] Key Laboratory of Optoelectronic Chemical Materials and Devices, Ministry of Education, Jianghan University, Wuhan 430056, China.
[b.] Institute of Materials Research and Engineering, A*STAR (Agency for Science, Technology and Research), 2 Fusionopolis Way, Innovis #08-03, Singapore 138634, Singapore.
[c.] Department of Chemistry, Northwestern University, Evanston, IL 60208, USA.
[d.] School of Materials Science and Engineering, Nanyang Technological University, 50 Nanyang Avenue, 639798, Singapore.
* Email: jw-xu@imre.a-star.edu.sg, alexyan@ntu.edu.sg, m-kanatzidis@northwestern.edu
† These authors contributed equally to this work.

convergence can improved Seebeck coefficient or weighted mobility in p-type lead chalcogenides,[18] n-type $Mg_2(Si_{1-x}Sn_x)$ solid solutions,[19] and p-type Cd-doped GeTe.[13] Resonant doping to raise the density of states near the Fermi level successfully enhances Seebeck coefficient in Tl-doped p-type PbTe, Al-doped n-type PbSe, In-doped SnTe,[20] and Sn-doped Bi_2Te_3.[21,22-24]

Moreover, a myriad of advanced processing techniques have been developed to modify the microstructures of TE materials to enhance phonon scattering. Such techniques introduce defects at different lengths scales and include nanostructuring by mechanical alloying[25] or spinodal decomposition,[26] multiscale structural design by melt-spinning and rapid sintering,[27] self-propagating high-temperature synthesis,[15, 28] or hot deformation.[29] Finally, development of materials with intrinsically low κ_L offers an effective way to decouple the electron and phonon transport.[16] For instance, the cubic I-V-VI_2 compounds, i.e. $AgSbTe_2$, $AgBiSe_2$, inherently exhibit low κ_L due to their strong lattice anharmonicity.[30] The liquid-like thermal conduction in $AgCrSe_2$ and Cu_2Se compounds furthermore gives glasslike κ_L and has provoked widespread investigation.[31, 32]

Deviation of atoms from their ideal sites in the crystal structures produces defects. The prevalence of defects in crystals has important consequences, and defect engineering is crucial for controlling the physical properties of solids. For example, defect chemistry plays an important role in determining the electronic, thermal, optical, magnetic, catalytic, and mechanical properties of materials,[33] and increasing attention is being directed to the application of defect engineering in the fields of catalysis,[34-37] metallurgy,[38, 39] energy storage[40, 41] and energy conversion.[17, 42, 43]

Because defects strongly impact both the electronic and thermal properties of solids, defect engineering is ubiquitous in the field of thermoelectrics. Introducing point defects by doping and alloying is the historically most important and robust approach for tuning the charge carrier concentration and reducing κ_L (by scattering high-frequency phonons)[44] Recently, vacancy-induced dislocation networks proved effective in scattering mid-frequency phonons in PbSe-based materials, leading to a significant reduction in κ_L.[45] Furthermore, the introduction of pores or nanoinclusions in ceramics and TE materials can arrest or deflect cracks, leading to improved mechanical response.[46, 47] To this end, defect engineering demonstrates great potential for enhancing both TE and mechanical properties of materials. Arguably, it is the most critical part of the arsenal for optimizing the performance of the materials.

In view of the critical role of defect engineering in thermoelectrics, researchers have utilized various useful models to predict or validate the effects of different incorporated defects on the TE properties of materials, including Zintl compounds,[48] half-Heuslers,[49] $CdIn_2Te_4$,[50] and BiTeI.[51] For example, $CdIn_2Te_4$ was first discovered as the promising TE candidate by using the high-throughput material screening method.[50] The high formation energies of cation vacancies (i.e. 2.315 eV for Cd vacancy and 2.996 eV for In vacancy) estimated from theoretical calculations result in the low hole concentration in pristine $CdIn_2Te_4$. Upon a suitable amount of Cu intercalation, the $CdIn_2Te_4$-based compound exhibits a significant improvement in the hole concentration due to the generation of Cu vacancies (with the formation energy of 0.402 eV). Therefore, a peak *ZT* of above 1.0 at 875 K can be attained for $Cd_{1.6}Cu_{3.4}In_3Te_8$ as manifested experimentally. In addition, high TE performances have been obtained in some p-type Zintl compounds, such as $Ca_5Al_2Sb_6$, $Yb_{14}MnSb_{11}$, and $CaZn_2Sb_2$, ascribed to their self-doping nature with relatively large hole concentrations and complex crystal structures which produce low κ_L. However, the n-type Zintl counterparts are seldom reported mainly reflecting the difficulty in achieving n-type doping. Despite the fact the computational predictions can accelerate the discovery of n-type Zintl compounds (such as $KAlSb_4$) with promising TE properties,[52] in the absence of synthetic breakthroughs on how to prepare such samples in the laboratory, this will remain a challenge. Moreover, the recently developed chemical replacements in structure prototype (CRISP) approach has proven "informative" in searching favourable n-type ABX Zintl candidates (A is group IA elements, B mainly refers to group IVA and IIB elements, and C is group VA elements).[53] KSnBi and RbSnBi phases are predicted to be promising n-type materials with considerable electron concentrations which benefit from the formation of native acceptor defects (i.e. Sn_{Bi}' antisite defects formed under the growth condition of excess K).[54] This finding is in sharp contrast to the intrinsic p-type conduction behaviour of other well-known Zintl pnictides, such as Mg_3Sb_2, where cation vacancies have the lowest formation energy and thereby serve as acceptor defects. These computational approaches can facilitate the determination of dominant defects and dopability of certain TE materials, thereby providing significant promise for the exploration of new TE materials.[48, 54, 55]

Many recently published reviews summarize the advances in state-of-the-art TE materials, such as tellurides,[56-62] selenides,[59, 63-69] sulfides,[63, 70] oxides,[71, 72] silicides,[73-75] antimonides,[76] half-Heusler,[77, 78] Zintl phases,[79] clathrates,[80] organics,[81-86] carbon nanotubes,[87, 88] materials with 2D structures,[89-92] and nanowire-based TE materials.[93] Other comprehensive reviews discuss the strategies for optimizing the TE properties from the perspective of chemical bonding,[16, 94] band engineering,[14] valleytronics,[95] phonon transport manipulation,[96] microstructure manipulation,[15, 97, 98] panascopic approach,[99] and practical applications.[100-104] Some outstanding reviews serve as tutorials to guide readers how to design high-performance TE materials,[9, 105-108] and how to reliably measure TE performance.[109]

Despite the centrality of defect chemistry in the field of thermoelectrics, the recent important developments on defect engineering in thermoelectrics have, to our knowledge, not been collectively discussed. Interested readers can refer to the following reviews or perspectives on defects chemistry in TE materials,[110, 111] and defect engineering in V_2VI_3 TE materials[17, 112] and oxides.[39] Here, we review the scientific approaches and summarize the recent advances and new insights resulting thereof in applying defect engineering to improving the TE

performance and mechanical properties. First, we introduce the various types of defects categorized by dimensionality, i.e. point defects (vacancies, interstitials, antisites, and so-called discordant atoms), dislocations, planar defects (twin boundaries, stacking faults and grain boundaries) and volume defects (precipitates and voids). Second, we summarize the conventional methods to characterize these defects in TE materials. We then discuss the influences of defect engineering on the electrical and thermal transport properties, as well as the mechanical performance of TE materials (as shown schematically in **Figure 1**). In the last section, we propose two major concerns related with defect stability and quantification of defects and provide some outlook.

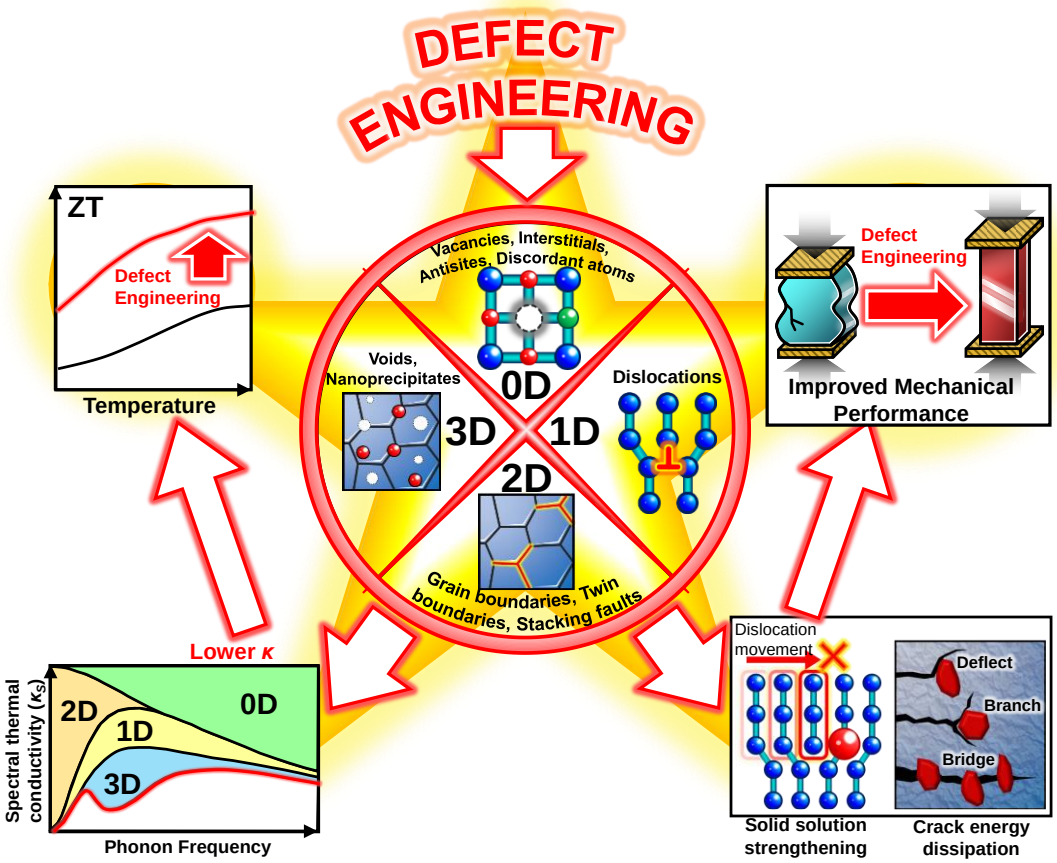

Figure 1. The schematic illustration of improving TE and mechanical properties of TE materials via defect engineering.

2. Defects and characterization methods of defects

2.1 Defects in crystals

Defects in solids can be classified based on their dimensionality. Point defects are atomic scale 0-dimensional (0D) defects including vacancies, interstitials, substitutions, Frenkel defects, Schottky defects, antisite defects, and what we recently refer to as discordant atoms. Point defects in thermoelectric materials are discussed in Section 3.1. Point defects can be introduced by adjusting the initial reaction stoichiometry or through post synthetic treatment, such as hot deformation,[44] electron irradiation,[113] plasma treatment,[114, 115] and ion implantation.[116] Bi_2Te_3-based materials are a good example, as they can exhibit either p- or n-type conduction depending on the impurity atoms, like Sb or Se. The comprehensive review by Zhu and coworkers provides insightful information about intrinsic defects in V_2VI_3 TE materials.[112]

Dislocations are 1-dimensional (1D) defects and can be further classified into edge and screw dislocations. Edge dislocations occur when an extra half plane of atoms is inserted into the crystal. Because they are much easier to observe than screw dislocations, edge dislocations are more commonly discussed in the TE field. Hence, in the remainder of this manuscript we use "dislocations" to refer explicitly to edge dislocations. Dislocations can be introduced through liquid phase sintering, vacancy engineering, and hot deformation. According to Klemens, a high dislocation density over 10^{12} cm^{-2} is needed for the scattering of mid-frequency phonons.[117]

Planar defects (or 2D defects) mainly refer to grain boundaries, phase boundaries, twin boundaries, or stacking faults. Grain boundaries are the interfaces between two adjacent grains within a polycrystalline material, while phase boundaries refer to the interfaces between different phases. Interface engineering is important for optimizing both thermal and electrical transport properties of TE materials, and is generally realized by controlling the synthesis procedure by

mechanical alloying, melt spinning[118] and/or solution-based processes. Stacking faults and twin boundaries often emerge in materials with layered or close packed structures and are proven to be effective in reducing κ_L by suppressing phonon propagation.[119, 120] Twin boundaries have a less detrimental effect on the carrier transport due to the ordered atomic arrangement.[119]

Finally, examples of volume defects (3D defects) are precipitates and voids. These can be introduced in either the synthesis or post-treatment process, and two important ways to incorporate precipitates into state-of-the-art TE materials are in-situ nanoinclusions and exotic second phase. We use the word exotic here in the context of being a phase chemically very unrelated to the matrix, such as graphene or carbon nanotubes incorporated into an inorganic semiconductor. The details of how these strategies are implemented is described in Section 3.4. Voids (or porous structures) are mainly formed during the densification process due to the shrinkage of powder materials or from air trapped inside. Both precipitates and pores can serve as additional phonon scattering centers to effectively reduce κ_L.

2.2 Characterization of point defects

Direct and comprehensive analysis of point defects is difficult to achieve with typical microstructure characterization techniques such as conventional powder X-ray diffraction (PXRD), scanning electron microscopy (SEM), transmission electron microscopy (TEM), Raman scattering, electron paramagnetic resonance (EPR), and Rutherford backscattering.[121-123] In contrast, electron/neutron scattering, synchrotron x-ray diffraction and advanced electron microscopy (such as Cs-corrected high-resolution TEM and atomic resolution electron energy loss spectroscopy) make it possible to study point defects in TE materials because of their high sensitivity and/or high resolution in the detection. For example, neutrons interact with atomic nuclei while x-rays interacts with electron clouds surrounding atoms, thereby neutrons are not affected by the charged electrons, and usually have higher penetration depth. Furthermore, neutrons have higher sensitivity to materials with light elements and can distinguish neighbouring elements in the periodic table, which is problematic for conventional XRD refinements.[124] Powder neutron diffraction (or inelastic neutron scattering) in combination with Rietveld refinement and theoretical calculation serves as a powerful route for providing reliable site occupancies and understanding defect structures in TE materials, such as rattler modes in clathrates,[125, 126] and Ni occupancies in Ni-substituted skutterudites.[124] Recently, the existence of Mg vacancies has been proven using powder neutron diffraction.[127] In the Y-doped $Mg_{3+\delta}Sb_{1.5}Bi_{0.5}$ compound, all intrinsic Mg vacancies were found to be occupied by Y and extra Mg atoms.[128] Y atoms preferentially enter the Mg sites of the covalently bonded $[Mg_2Sb_2]^{2-}$ layer. Interestingly, however, is a noteworthy synchrotron x-ray diffraction study showing that high-density Frenkel defects (i.e. pairs of Mg vacancies and Mg interstitials) .[129] These controversial findings in Mg_3Sb_2-based materials underline the challenges that exist in fully characterizing point defects and the importance of utilizing suitable and complementary tools, such as electron scattering,[49, 130] synchrotron XRD,[131, 132] and electron probe microanalysis (EPMA),[44, 133] for their investigation. In an another interesting example, vacancy-related short range order has been reported and modelled in defective half-Heusler compounds using electron scattering and Monte Carlo simulations.[49, 134] Coupling with EPMA, a typical non-destructive elemental analysis, fully qualitative and quantitative understanding can be realized to interpret the composition dependent point defect evolution. Furthermore, in $(Bi,Sb)_2(Te,Se)_3$ solid solutions their actual composition analysis by EPMA offers the ability to further optimize the TE performance as the point defects (such as antisite defects and vacancies) in $(Bi,Sb)_2(Te,Se)_3$ show a strong dependence on the compositions.[44]

In view of the wide application of the above-mentioned techniques, we defer in describing their technical principles. Instead below we briefly introduce two relatively new in thermoelectrics efficient tools (i.e. positron annihilation spectroscopy and deep-level transient spectroscopy) in characterizing point defects.

2.2.1 Positron annihilation spectroscopy

Positron annihilation spectroscopy (PAS) can provide information on the relative concentration and type of point defects and vacancies with parts per-million level sensitivities,[121, 122, 135-141] and is therefore increasingly used by researchers seeking to obtain a deeper understanding of the defects in TE materials. The advantages of PAS over other characterization techniques are inherent to its fundamental working principles, where the positively charged positrons spontaneously seek valence electrons of the atoms in the sample and annihilate, releasing gamma radiation as shown in **Figure (a)**. A positron lifetime spectrum can then be obtained from the gamma radiation after a series of signal transformations within a PAS spectrometer, as represented in detail in **Figure (b)**. Deconvolution and analysis of the obtained positron lifetime (τ) spectrum can provide characteristic information on the defects.[122, 135, 142, 143] The interested reader can refer to the paper by Tuomisto and Makkonen for a detailed review of positron annihilation characterization techniques and their theory.[142]

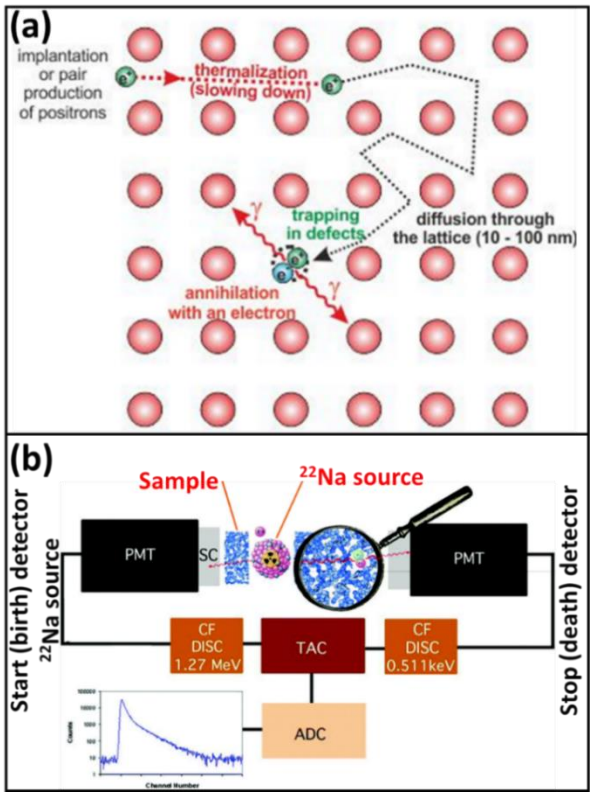

Figure 2. (a) Schematic representation of the scattering, diffusion, and annihilation of an implanted positron within a host material.[144] Copyright 2013, Maik Butterling. (b) Schematic diagram of a PAS spectrometer set up, where the ^{22}Na source (purple sphere) is sandwiched between the sample material (blue) to maximize the quantity of emitted positrons penetrating the sample. After the resulting gamma radiation signals are detected by an assembly of fast scintillators (SC), photomultiplier tubes (PMT) and constant fraction differential discriminators (CF DISC) on each side, a positron lifetime spectrum (blue line) can be obtained through further signal conversions by a time-to-amplitude converter (TAC) and an analogue-to-digital converter (ACD). Readapted with permission from ref[145]. Copyright 2015, The Royal Society of Chemistry.

Li *et al* performed PAS measurements and calculations of the positron lifetime and density distribution in $Bi_{0.975}Cu_{0.975}SeO$ and revealed a higher positron density around the Bi vacancy centers in the insulating $[Bi_{1.95}O_2]^{2+}$ layers compared to the Cu vacancy centers in the conductive $[Cu_{1.95}Se_2]^{2-}$ layers.[136] The observed improvement in σ, with minimal losses to S, was largely attributed to the interlayer charge transfer between the Bi/Cu dual vacancies. While single-vacancy defects are very useful to TE materials for their ability to strongly scatter phonons and reduce κ_L, they may also significantly deteriorate the charge carrier mobility μ and σ, thus dual or multiple vacancies were explored as a potential strategy to overcome the detrimental coupling between electrical and thermal transport properties.[146, 147]

Furthermore, several groups have used PAS to explore the effect of spark plasma sintering (SPS) and the subsequent processing conditions on vacancy defects in sintered pellet samples.[122, 140, 148] He *et al* employed PAS as a sensitive probe for the vacancy defects in the grain boundary regions.[122, 140] While phonon scattering at the grain boundaries is usually suggested as the key reason for the low κ_L of nanocomposites,[149-151] the contribution from the interfacial vacancies cannot be ignored, thus requiring PAS to distinguish between the two possible phonon scattering mechanisms, which would otherwise be difficult to tell apart solely by conventional microstructure characterization techniques. Through a combination of PXRD and PAS measurements on sintered Bi_2Te_3 nanocrystals, He *et al.* discerned the increase in κ_L with greater annealing temperatures is mostly due to the decrease in vacancy concentration at the grain interfaces. The PXRD data demonstrated the estimated average grain size of the sintered Bi_2Te_3 pellets remains almost unaltered with increased annealing temperature from the up to 773 K, implying grain boundary scattering is not the dominant phonon scattering mechanism. On the other hand, the PAS data showed a monotonic decrease in the I_2 intensities, indicating the vacancy concentration in the interfaces drops significantly, thus leading to the conclusion that the phonons in Bi_2Te_3 nanocrystalline samples are primarily scattered by the interfacial vacancies rather than the interface regions themselves.[122]

More recent work reached a similar conclusion when increasing the sintering temperature of In_2O_3 nanopowders. Like in Bi_2Te_3, the In_2O_3 grains also remained relatively constant in size with increased annealing temperature, but a sharp decrease in the measured positron lifetimes τ_1 and τ_2 implied a recovery of monovacancies and vacancy clusters. However, the same conclusion cannot be drawn from the effect of increasing the vacuum annealing temperature of the In_2O_3 sintered pellets. Despite the decrease in κ and average positron lifetimes, the increasing grain size leads to an ambiguity in the determination of the dominant phonon scattering mechanism.[140]

In addition to vacancies, Tan *et al* employed PAS to investigate La_{Bi} substitutional point defects in n-type $Bi_{2-x}La_xO_2Se$. Because La is more electropositive than Bi, the La_{Bi} defects may act as isoelectronic hole traps. As the La fraction (x) is increased from 0 to 0.04, the $\tau_2 I_2$ component increases linearly.[138] Since $\tau_2 I_2$ is characteristic of positron annihilation at the negatively charged Bi vacancies, Tan *et al* deduced the La_{Bi} sites become positively charged after trapping holes and repel the injected positrons which then gather at the Bi vacancies, thus supporting the hypothesis of hole-trapping at La_{Bi} sites.[152, 153] Due to the synergistic combination of the hole traps and the narrowed band gap, moderate La doping causes the electron concentration to rise by four orders of magnitude compared to the pristine Bi_2O_2Se.

While increasingly common, PAS is yet to be widely known or utilized in the TE field. Currently, the most common use of PAS by many researchers is for overall quantification of vacancies. The above specialized examples show that PAS can also be used to distinguish and identify the type and size of defects to better understand the charge and thermal transport properties. Together with other characterization techniques, phonon scattering mechanisms can also be elucidated from the interpretation of PAS results. The selectivity and sensitivity of the characterization technique are paramount to obtain more comprehensive information of the defects and formulate sound strategies to make further improvements in the performance of TE materials.

2.2.2 Deep-level transient spectroscopy

In addition, another sensitive method to probe point defects or traps in semiconductors is deep-level transient spectroscopy (DLTS) which was initially proposed by Lang in 1974.[154] It is based on the measurement of high-frequency capacitance

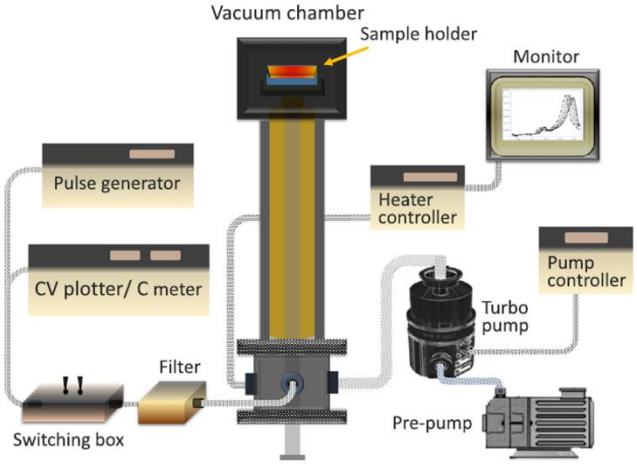

Figure 3. Configuration of the DLTS set-up. Reproduced with permission from ref[155]. Copyright 2019, AIP publishing.

transients as a function of temperature. By applying an altered voltage on the sample, a p-n junction or Schottky barrier can be created which serves as the probe to identify deep-level impurities with respect to their activation energy, defect type and defect concentration. Thereby DLTS is capable of establishing the relationship between charge carrier concentration and point defects. It has a detection limit of 10^8 cm^{-3} for point defects.[123] It is noteworthy that the conventional DLTS operated at below 400 K is suitable for monitoring defects in narrow bandgap semiconductors while a customized high-temperature DLTS can provide insight into more deep-level trapped defects in wide bandgap semiconductors.[155] The main configuration of DLTS is listed in **Figure 3**. In combination with these merits, this technique is promising for experimentally detecting the dopability and understanding the role and nature of defects in TE materials, in particular, thin films. This technique has not been implemented in studying thermoelectric materials. Interested readers can refer to the relevant books and references for more details.[123, 154]

2.3 Quantification of dislocations

Electron microscopy techniques such as TEM can be used to qualitatively observe dislocations in a material. By counting the number of dislocations within the selected area of interest, TEM can be used to estimate the areal dislocation density (N_D) in TE materials.[156, 157] In order to form meaningful correlations between the macroscopically measured TE properties and N_D, analysis of a larger quantity of the sample is often desired to obtain a more representative value of the concentration of these 1D defects. Therefore, the small sample size used for imaging makes macroscopic quantification of dislocations in the bulk sample is impractical using TEM.

Chen *et al.* macroscopically estimated N_D in $Pb_{1-x}Sb_{2x/3}Se$ and $Na_yEu_{0.03}Pb_{0.97-y}Te$ samples using synchrotron powder X-ray diffraction (Syn-PXRD) measurements together with a modified Williamson–Hall (mWH) model.[45, 158] The analysis is presented in **Figure 4**. Starting from the crystallite sizes and peak broadening measured by Syn-PXRD, the derived values of K and ΔK were then used in the mWH plot as indicated by Equation (2).

$$\Delta K = \frac{0.9}{d} + \left(\frac{\pi A^2 B_D^2}{2}\right)\sqrt{N_D}K^2C \pm O(K^4C^2) \quad (2)$$

The N_D values determined by the slope of the mWH plot were in good agreement with those estimated by TEM observations. While the same analysis can be performed using ordinary powder X-ray diffraction (PXRD) measurements, the N_D values derived by PXRD are only useful for qualitative comparisons because of the lower angular resolutions and signal/noise ratios of PXRD as compared to Syn-PXRD.[159] This work revealed that N_D increases with Sb content in $Pb_{1-x}Sb_{2x/3}Se$ (x=0~0.07) and maximizes at Na content of y = 0.025 in $Na_yEu_{0.03}Pb_{0.97-y}Te$ solid solutions. The increased dislocation density with incorporated aliovalent dopants in PbSe- and PbTe-based materials could be ascribed to the accelerated nucleation and multiplication processes for dislocation promoted by point defect diffusion upon annealing.[160, 161] As predicted by models based on the Debye approximation, dislocation scattering of mid-range frequency phonons accounts for 80%–90% and ≥30% κ_L reductions in $Na_{0.025}Eu_{0.03}Pb_{0.945}Te$ and $Pb_{1-x}Sb_{2x/3}Se$ respectively, thus highlighting the significance of accurate quantification of these defects.[45, 158]

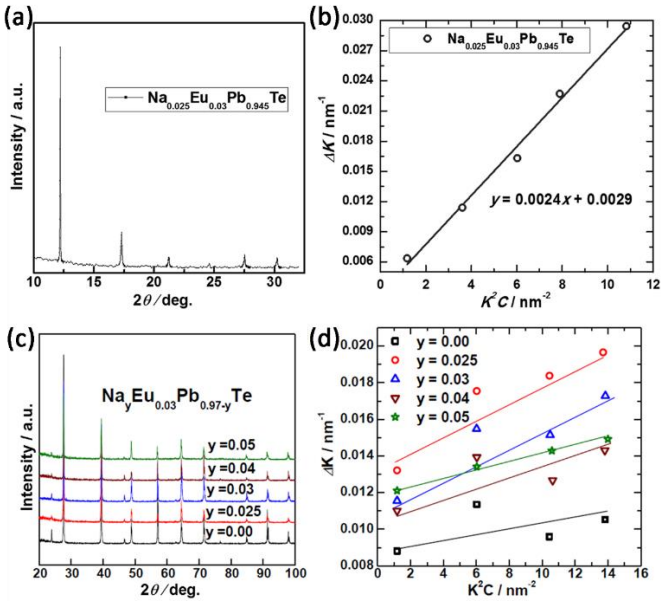

Figure 4. (a) The synchrotron X-ray diffraction pattern and (b) the peak broadening analysis by the modified Williamson–Hall plot. (c) The powder XRD pattern and (d) the peak broadening analysis by the modified Williamson-Hall plots for $Na_yEu_{0.03}Pb_{0.97-y}Te$ ($y \leq 0.05$) samples. Reproduced with permission from ref[162]. Copyright 2017, Wiley-VCH.

3. Improved thermoelectric performance by defect engineering

3.1 Point defects

Point defects are 0-dimensional (0D) defects that are ubiquitous in real crystal lattices. The common types of point defects are illustrated in **Figure 5** for a two-dimensional lattice. From the context of thermoelectric engineering, point defects lead to a τ_{PD} α ω^{-4} phonon relaxation time, and thus are extremely effective at scattering high frequency ω phonons. Historically, point defect engineering, either by extrinsic doping/alloying or manipulating the intrinsic defects is likely the most widely studied means of reducing the lattice thermal conductivity. Point defect phonon scattering originates from both mass fluctuation and strain field contrast in the lattice. Pioneering theoretical studies by Klemens,[163, 164] Callaway[165, 166] and Abeles[167] have modelled the effect of point defects on the lattice thermal conductivity. Early experiment work on PbTe-PbSe solid solutions[168] and SiGe alloys[169] demonstrates the efficacy of solid-solution alloying in reducing the phonon mean free path via enhanced phonon scattering. Following-up studies extend this strategy to many other TE materials, such as $(Bi,Sb)_2(Te,Se)_3$ compounds,[170] and Mg_2X (X=Si, Ge, Sn) solid solutions.[171] In this section, we mainly focus on the intrinsic point defects and their impacts on charge transport and phonon scattering in TE materials.

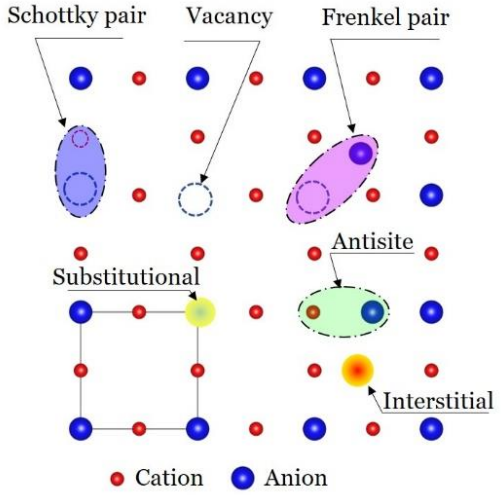

Figure 5. Illustration of common point defects in a two-dimensional lattice where the red and blue spheres denote cations and anions, respectively. A Schottky pair is formed by a pair of cationic and anionic vacancies.

3.1.1 Vacancies. In crystals, vacancies occur when atoms are absent from crystal lattice sites that would be fully occupied in a perfect crystal. Vacancies inherently appear in all crystalline solids due to the increase in entropy from the structural disorder. According to thermodynamic equilibrium theory, the vacancy concentration complies with the relationship,

$$N_V = N\,exp(-Q_V/k_BT), \quad (3)$$

where N_v and N are the vacancy concentration and atomic concentration respectively, Q_V is the vacancy formation energy, k_B is the Boltzmann constant, and T is the absolute temperature. Therefore, lower vacancy formation energy and higher temperature tend to produce more vacancies. Schottky imperfections occur when a pair of oppositely charged ions leave their crystallographic sites, leaving behind vacancies. As shown in **Figure 5**, cationic and anionic vacancies tend to form Schottky clusters in a stoichiometric ratio (i.e. pairs of cationic and anionic vacancies) to conserve the local charge neutrality. Another important point defect is the Frenkel imperfection, which is a vacancy created when an atom is displaced from its initial lattice position and lodged into a neighboring interstitial space, as highlighted by the purple ellipsoid in **Figure 5**. Due to the squeezing of an atom into an interstitial void and the resulting irregular coordination environment, Frenkel defects occur more easily in compounds consisting of smaller atoms (hydrogen, carbon, etc.).

In TE materials, S, σ, and κ_e are highly correlated and are functions of the charge carrier concentration. Conventional chemical modification intentionally introduces atomic vacancies to modulate the position of the Fermi level to optimize the carrier concentration. For example, cubic rare-earth telluride TE materials, RE_3Te_4 (RE = La, Ce, Pr) intrinsically host nearly metallic electron concentrations, and cation

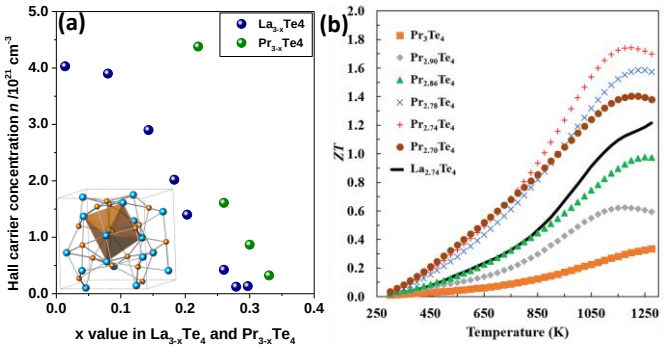

Figure 6. (a) Hall carrier concentration as a function of x value (i.e. vacancy concentration) in $La_{3-x}Te_4$ and $Pr_{3-x}Te_4$. Data were taken from literature.[172, 173] The inset presents the cubic crystal structure of $La_{3-x}Te_4$ at full La occupancy, where La could be replaced by Ce and Pr. Cyan and brown spheres represent lanthanum and tellurium atoms, respectively. Reproduced with permission from ref[172]. Copyright 2008, The American Physical Society. (b) ZT values of $Pr_{3-x}Te_4$, a peak ZT of 1.7 was achieved at 1200 K by tuning Pr vacancy. Reproduced with permission from ref[173]. Copyright 2018, Cell Press.

vacancies can be intentionally introduced, i.e. $RE_{3-x}Te_4$, to offset excess electrons in stoichiometric RE_3Te_4.[172, 174-176] The increase in cationic vacancies (**Figure 6a**) shifts the Fermi level down to a proper position to achieve the optimized carrier concentration. The ZT values were achieved at 1.2 and 1.7 in $La_{2.74}Te_4$ and $Pr_{2.70}Te_4$, respectively[173, 177] (as shown in **Figure 6b**).

Vacancies sometimes can induce ionized impurity scattering which significantly alters the carrier transport properties. The carrier mobility μ is described as,

$$\mu = \frac{e\tau}{m^*} \quad (4)$$

where e, τ and m^* denote the electron charge, τ is the carrier relaxation time, and the effective mass, respectively. The relaxation time τ is related with carrier energy E, temperature T, and m^* via the following formula,[ref to be added]

$$\tau \propto E^r T^s (m^*)^t \quad (5)$$

where r is the carrier scattering factor, s and t are constants independent of temperature. Therefore, regulating the carrier

scattering mechanism becomes another effective route to improve the carrier mobility. For example, the intrinsic Mg vacancies determine the p-type transport behaviour of Mg_3Sb_2.[178, 179] Recent efforts have been devoted to developing n-type counterparts by involving excess Mg content to compensate Mg vacancies that are sensitive to the synthesis conditions.[178] A typical nominal composition of $Mg_{3.2}(Sb,Bi)_2$ (~6.7 at% Mg excess) is usually considered in the ball-milling and high-temperature consolidation process.[178, 180] Moreover, a systematic research has been carried out to study the effects of hot pressing temperature and holding time on controlling the Mg vacancies in $Mg_{3.2}(Sb,Bi)_2$-based compounds.[181]

Furthermore, phonon vacancy scattering can strongly suppress the propagation of heat-carrying phonons, thereby decreasing the lattice thermal conductivity. By alloying In_2Te_3 into a SnTe host matrix, the native concentration of cation vacancies increases, and the vacancies dominate the phonon transport, as shown in **Figure 7a**.[20] Similarly, in the SnTe-$AgSbTe_2$ solid-solution, the concentration of Sn vacancies reaches up to 6 mol %. Here, the vacancies are suggested to soften the lattice and jointly strengthen phonon scattering to considerably reduce the lattice thermal conductivity, therefore giving rise to a high *ZT* of 1.1 at 800 K.[182] As shown in **Figure 7b**, suppression of the lattice thermal conductivity in SnTe-$AgSbTe_2$

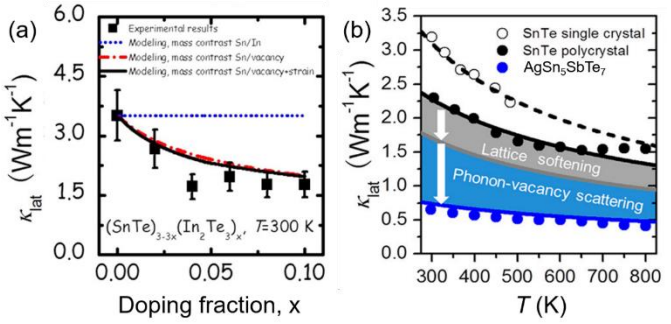

Figure 7. (a) Lattice thermal conductivity, κ_{lat} as a function of doping fraction, x in $(SnTe)_{3-3x}(In_2Te_3)_x$. Reproduced with permission from ref[20]. Copyright 2015, The American Chemical Society. (b) Temperature dependence of κ_{lat} for SnTe single crystal, SnTe polycrystal and $AgSn_5SbTe_7$. The solid lines are Debye-Callaway model calculation considering different phonon scattering mechanisms. Readapted with permission from ref[182]. Copyright 2018, American Chemical Society.

can be quantitatively described by the enhanced vacancy-phonon scattering and lattice softening, as captured by the phonon-vacancy scattering lifetime τ_{vac} in Equation (4),

$$\tau_{vac} = f\frac{3V\omega^2k^2}{\pi v_g}s^2 \quad (4)$$

in which s^2 is the phonon-vacancy scattering strength, *V* is the average atomic volume, ω is the phonon frequency and v_g is the sound velocity.

A following study on the sodium analogues, SnTe–$NaPnTe_2$ (Pn = Sb, Bi), reported similar results. Here, alloying $NaSbTe_2$ into SnTe nearly doubles the concentration of Sn vacancies, enhancing phonon scattering and giving a ~6% decrease in the sound velocity to achieve glasslike lattice thermal conductivity under 0.7 $W{\cdot}m^{-1}{\cdot}K^{-1}$ at room temperature.[183] As a result, the SnTe–$NaSbTe_2$ alloys reach high *ZT*s approaching 1.1–1.2 at 800–900 K. Surprisingly however, $NaBiTe_2$ alloying does not substantially alter the vacancy concentration, and the SnTe–$NaBiTe_2$ alloys only exhibit modest *ZT*s of ~0.85 at 900 K. The SnTe–$ASbTe_2$ (A = Ag, Na) are therefore unique systems in which enhancement of the native Sn vacancy concentration is beneficial to the thermoelectric performance owing to the significant suppression of κ_L by vacancy phonon scattering and lattice softening.

The above examples are all cases where vacancies are manipulated to improve the thermoelectric performance through favorably modulating the carrier density and/or strengthening phonon scattering. Yet, vacancies can often be problematic, either resulting in overdoping or by acting as carrier traps that prevent consistent or sufficient doping. For example, in PbTe, attempts to stabilize the optimal n-type electron concentration are often inconsistent, where samples with nominally identical doping level regularly exhibit different carrier concentrations. By integrating defect energy calculations and experimental compositional mapping, Male *et al* demonstrated the difficulties in achieving high doping efficiency stem from deviations from the ideal stoichiometry during synthesis to give Pb vacancies, which act as acceptor defects and suppress the electron concentration.[184] This works suggests that Pb-rich conditions are crucial to achieve good n-type doping efficiency. Experimentally, this can be achieved by annealing the doped samples in a slightly Pb-rich atmosphere, and this saturation annealing procedure provides a robust means of reliably preparing degenerately doped n-type PbTe.

The process of combining defect energy calculations with experimental investigation of the intrinsic widths of formation is known as phase boundary mapping and is emerging as a powerful means of leveraging the intrinsic defect chemistry of thermoelectric materials to determine to optimum conditions for subsequent extrinsic doping. In addition to PbTe, such techniques lead to new understanding and control over the thermoelectric properties of the Zintl compounds Mg_3Sb_2, $Ca_9Zn_{4+x}Sb_9$,[185] $Cu_2HgGeTe_4$,[186] and the half Heusler ZrNiSn.[187] These studies highlight the increasingly prominent role of theory in guiding experimental establishment of optimal doping conditions in thermoelectric materials. The success of n-type Mg_3Sb_2 provides a particularly compelling example.

In general, Zintl antimonides are one of the classic material family where vacancies largely control and limit the thermoelectric functionality. Here, the intrinsically high density of cation vacancies normally constrains antimonides to p-type doping, despite theoretical predictions of favourable conduction band structures. Nevertheless, shortly after reports of high performance in n-type Mg_3Sb_2, Ohno *et al* used defect energy calculations to predict that preparing Mg_3Sb_2 with excess Mg will suppress the Mg-vacancy electron traps and make the samples amendable to further n-type doping.[188] Experiments confirmed that samples annealed in Mg-rich conditions indeed reduces the vacancy concentration, and Te-doped, Bi-alloyed $Mg_{3+x}Sb_{2-y}Bi_y$ reach n-type carrier concentrations of 10^{20} cm^{-3} and outstanding *ZT*s near 1.6 at 700–800 K,[189-193] significantly outperforming the p-type counterparts that feature *ZT*s under 1.

This success paired, with the relatively lower cost and toxicity of Mg and Sb compared to traditional PbTe and Bi_2Te_3 thermoelectrics, make Mg_3Sb_2 derived materials among the most exciting materials in the field.[194]

As evident from the above discussion, metal chalcogenides and antimonides represent the mainstream in TE research. On the other hand, oxide thermoelectrics, such as $SrTiO_3$,[195, 196] $CaMnO_3$,[197] BiCuSeO,[198, 199] Na_xCoO_2,[200] $Ca_3Co_4O_9$,[201] and $[Bi_{0.87}SrO_2]_2[CoO_2]_{1.82}$ (BSCO)[202] are also widely investigated as promising materials with excellent thermal stability, oxidation resistance and low-toxicity constituents.[71] Defect chemistry likewise provides a good means of enhancing TE properties of these materials. For instance, the electrical conductivity of $SrTiO_{3-\delta}$ can be enhanced by controlling oxygen vacancies (acting as electron-donating defects which are pervasive in $SrTiO_3$) under different oxygen partial pressures or highly-reducing conditions.[203, 204] Moreover, the incorporation of Sr vacancies in $Sr_{1-y}Ti_{0.9}Nb_{0.1}O_{3-\delta}$ results in fast charge transport as manifested by the improved weighted mobility $\mu(m^*/m_0)^{3/2}$ where m_0 is electron mass.[204] This could be ascribed to the following reasons, 1) a slight Sr deficiency suppresses the formation of insulating defects (i.e. Ruddlesden–Popper-type planar faults and highly-defective core-shell structures with Sr enriched shells); 2) alternation of local strains induced by Sr vacancies that facilitates electron transport; and 3) Sr cations may block the electron transport based on the band structure calculation. The Sr vacancies were found to combine with oxygen vacancies to form vacancy clusters that can effectively scatter heat-carrying phonons.[204] Likewise, the beneficial effects of cation and oxygen vacancies on the electrical and thermal transport properties have been reported in BiCuSeO,[136] Na_xCoO_2,[205] and $CaMnO_3$,[206] contributing to the substantial increase of overall *ZT* values.

3.1.2 Interstitials. Interstitial defects refer to crystallographic imperfections where intrinsic or foreign atoms (classified as self-interstitial and interstitial defects, respectively) encroach upon sites that are expected to be unoccupied, i.e. the interstitial positions in lattice structure, shown by red sphere in **Figure 5**. The classic example is intentional introduction of interstitial defects into the void sites in skutterudites and clathrates.The interstitial filler atoms are normally alkaline, alkaline earth, and rare earth atoms that are only weakly bound in the void site and thus behave as rattlers, which introduced new low lying modes into the phonon spectrum, significantly enhancing the available phase space available for scattering and resulting in broad-spectrum resonant phonon scattering.[126, 207-210] Likewise, interstitial filler atoms have also been associated with reduced sound velocity in filled $FeSb_3$ and $CoSb_3$.[126, 207, 211] Xu *et al* adopted a multiple-filler strategy in skutterudites, giving rise to continually promoted *ZT* values from 1.1 to 1.7 at 850 K, depicted in **Figure 8a**.[212]

Moreover, the interstitial defects also suppress the phonon transport by bringing about fluctuations in mass and lattice strain which can be described by the Debye-Callaway model. By alloying 12% Cu_2Te into SnTe crystals, Pei *et al*[213] demonstrated

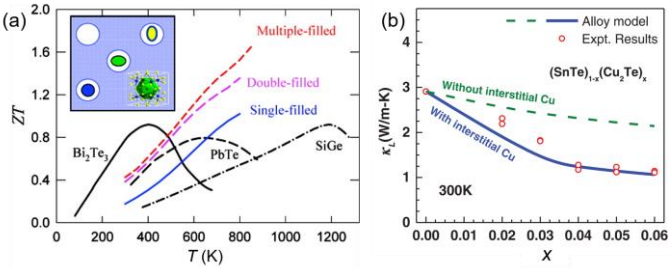

Figure 8. (a) *ZT* values in filled-skutterudites compared with typical TE materials. The inset shows the multiple fillers and skutterudite crystal structure. Reproduced with permission from ref[212]. Copyright 2011, American Chemical Society. (b) Composition dependence of the lattice thermal conductivity at 300 K for $(SnTe)_{1-x}(Cu_2Te)_x$. Reproduced with permission from ref[213]. Copyright 2016, Wiley-VCH.

the coexistence of Cu substitutional and interstitial point defects, in which the later strongly impede phonon propagation and diminish κ_L, as depicted in **Figure 8b**. In the $(SnTe)_{1-x}(Cu_2Te)_x$ solid solution, the κ_L obtained at 12 mol% Cu_2Te-alloyed SnTe can be as low as 0.5 W m^{-1} K^{-1} at 850 K, close to the amorphous limit ($\kappa_{L,min}$ = 0.4 W m^{-1} K^{-1}). Surprisingly, the interstitial point defects do not deteriorate the charge transport, and this pure thermal suppression strategy promotes the ZT from 0.4 up to 1.0. By incorporating Cu interstitial defects to scatter phonons, a record high *ZT* of 1.6 was achieved in the optimal composition of $Sn_{1.03-y}Mn_yTe(Cu_2Te)_{0.05}$ (y=0.14).[214]

Cationic interstitial defects are much more common than their anionic counterparts due to smaller sizes of cations and the subsequently smaller lattice distortion and strain energy required to create a cation interstitial. Furthermore, the coexistence of diverse point defects is pervasive in TE materials. By intentionally tailoring the initial stoichiometry and crystal growth conditions, the point defects anticipated to be favorable to the TE performance can be built up. However, as point defects are generally dilute and randomly distributed throughout the host matrix, it is a grand challenge to attain direct observations of the defects. Based on density functional theory (DFT), Liu *et al* calculated the formation energy of point defects in Mg_2X (X= Si, Ge, Sn) under both cation-rich and anion-rich conditions.[215] Their calculated results demonstrate that Mg vacancies and interstitial Mg are the dominant defects, playing acceptor- and donor-like roles in charge transport. Formation of interstitial Mg is more favorable in Mg_2Si compared to Mg_2Ge and Mg_2Sn, because of the strong electrostatic interaction of interstitial Mg with Si and smallest strain energies in Mg_2Si, as depicted in Figure

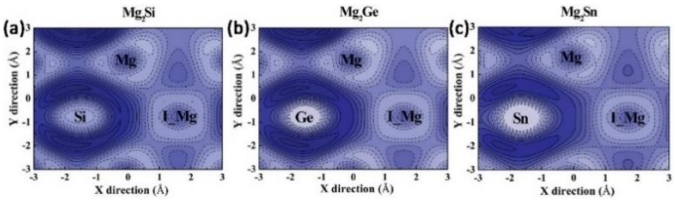

Figure 9. Contour plot of the charge density difference of $Mg_{65}X_{32}$, (a) X=Si, (b)X=Ge, (c) X=Sn with a Mg interstitial. The dashed lines and the solid lines demonstrate charge depletion and accumulation respectively. Reproduced with permission from ref[215]. Copyright 2016, Wiley-VCH.

8. The interaction strength is directly depicted by the change in charge density along Mg-X chemical bonding. As illustrated in **Figure 9**, the degree of charge density accumulation between interstitial Mg and X ascends from Mg_2Sn to Mg_2Ge and to Mg_2Si, which suggests the interaction between the interstitial Mg with Si is stronger than with Ge or Sn.

3.1.3 Antisite defects. Antisite defects occur when two elements exchange atomic positions, i.e. when an atom (A) relocates to a site (B) in AB compound, or vice versa, as shown by the green ellipsoid in Figure 3. Antisite defects commonly occur in weakly ionic or covalent crystals due to the energetic favorability of exchanging atomic sites. Especially in TE materials, antisite defects are pervasive in degenerate semiconductors that lack strongly prohibitive electrostatic repulsions. Consequently, it is crucial to understand the impact of antisite defects on the charge carrier type and concentration of TE materials.

Based on extensive and systematic research on V_2VI_3 binary compounds, Zhu *et al* proposed a simple yet effective (χ, r) model[112] where the formation energy of antisite defects E_{AS} is strongly correlated with ionic electronegativity χ and covalent radius r. According to this model, antisite defects are more energetically favorable when cations and anions have minor discrepancies in electronegativity and covalent radius. This model provides a useful means of predicting the evolution of the dominant charge carrier type and concentration in TE materials after alloying with elements of the same group. For example, substituting Te for Se in Bi_2Te_3 enlarges the (χ, r) difference and, tends to increase E_{AS}, suppress the formation of positively charged antisite defects, and diminish the hole concentration, n_h.[44] Conversely, reduction of the (χ, r) discrepancy, which occurs when partially substituting Bi with Sb in $Bi_{2-x}Sb_xTe_3$, facilitates the formation of antisite defects. Here, the smaller distinction of (χ, r) between Sb and Te compared to that between Bi and Te ultimately promotes n_h in p-type $Bi_{2-x}Sb_xTe_3$.[216-218]

Similar to their prevalence and usage in V_2VI_3 compounds, antisite defects are also common in half-Heusler (HH) alloys, where they play significant roles in altering the band structure and phonon scattering.[219] In ZrNiSn, Zr/Sn antisite defects are common due to the similar covalent radii (1.45 Å for Zr and 1.41 Å for Sn) and shrink the band gap, increase the density of states (DOS), and scatter phonons strongly, which consequently contributes to a higher power factor, lower κ and finally yields a higher ZT value, as compared to counterparts with lower concentration of antisite imperfections.[220]

3.1.4 Discordant Atoms. An atom substituted in a crystal lattice is said to be discordant if its local chemistry disagrees with the implied or imposed chemistry of that particular crystal site. The atom then must choose between adopting the coordination geometry characteristic of its own intrinsic local chemistry or that imposed by the host crystal site. For example, if an atom is always found to be tetrahedral in its compounds but it is forced to occupy an octahedral site it will always attempt to adopt the tetrahedral geometry. These atoms may be the correct size for the host site but they resist adopting the required coordination geometry and thus deviate from it by moving away from the ideal position. Historically, such local bonding arrangements were overlooked because X-ray diffraction only gives information on the average atomic positions. Recently however, probes of local structure including pair distribution function (PDF) and solid-state NMR coupled with theoretical simulations have provided strong evidence that many promising thermoelectric systems indeed feature local off-centering of specific atoms. Examples of discordant atoms in thermoelectric materials, and how they influence phonon scattering and electronic structure, will be discussed below.

Good examples are the alloys of PbSe with HgSe or CdSe, which both feature excellent p-type ZTs ~ 1.6–1.7 near 950 K.[221, 222] While pure HgSe crystallizes in the zincblende structure with tetrahedrally coordinated Hg, X-ray diffraction suggests HgSe and PbSe form a solid solution in which the Hg atoms rest on the octahedrally coordinated Pb sites of the rocksalt PbSe structure. Interestingly however, DFT calculations indicate the most energetically favorable position for the Hg atoms is slightly off-centered away from the anticipated octahedral geometry and toward the tetrahedral holes. This prediction is in line with chemical intuition, which anticipates Hg to prefer tetrahedral coordination. The Hg off-centering is experimentally supported by solid state NMR performed on the alloyed samples and is suggested to strengthen the phonon scattering (**Figure 10a-c**), contributing to the high figures of merit reported for PbSe-HgSe. Similar DFT and NMR results strongly point towards Cd off-centering in the PbSe-CdSe alloys.[222]

Discordant bonding arrangements are furthermore reported in the n-type alloys PbSe-GeSe and PbS-GeS. Like in the above alloys, DFT calculations show the Ge^{2+} atoms energetically prefer to lie away from the expected center of the octahedral sites because of the strong tendency of the $4s^2$ lone pair of electrons to stereochemically express itself (**Figure 10d**). The off-centering introduces new low-lying optical phonon modes into the vibrational spectrum, both softening the lattice and

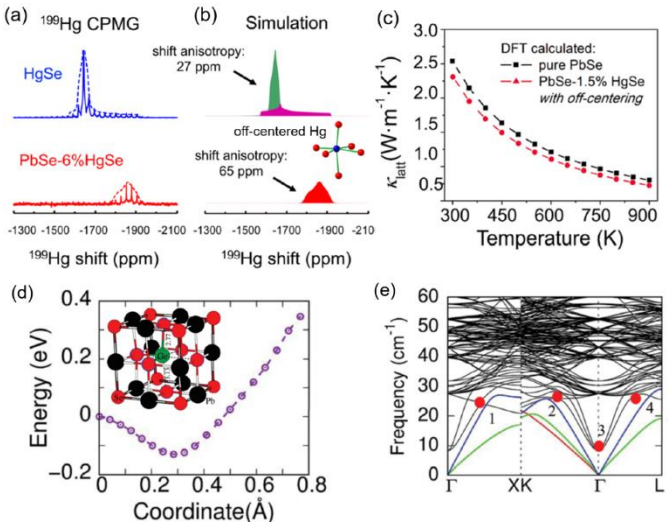

Figure 10. (a) Experimental ^{199}Hg CPMG static NMR spectra and (b) corresponding simulations for HgSe and PbSe−6%HgSe. The major peak (green) in the HgSe spectrum is attributed to Hg at the tetrahedral site within HgSe, and the small shift anisotropy (27

ppm) indicates high symmetry. Conversely, the PbSe−6%HgSe spectrum (red) shows a large shift anisotropy of 65 ppm, indicating an asymmetric bonding environment. The inset illustrates a locally distorted $HgSe_6$ octahedron. (c) DFT calculated κ_{lat} for pure PbSe and PbSe-HgSe showing suppressed κ_{lat} when considering the Hg off-centering. Reproduced with permission.[157] Copyright 2018, American Chemical Society. (d) Energy profile of PbSe-GeSe as a function of atomic coordinates from the octahedral Ge substituted Pb site along the (111) direction towards the tetrahedral site. The inset shows Ge shifted away from the octahedral position. (e) DFT calculated phonon dispersion for PbSe-GeSe considering the Ge off-centering. Low-lying optical modes (marked with red dots) and suppressed phonon group velocities are found, features that are not present in calculations without the discordant Ge. Reproduced with permission from ref[222]. Copyright 2020, The Royal Society of Chemistry.

enhancing the phonon scattering (**Figure 10e)**.[223] In PbSe-GeSe, the discordant bonding results in exceptionally low lattice thermal conductivities ~0.36 W m^{-1} K^{-1} and a peak ZT ~ 1.5 with an outstanding ZT_{avg} of 1.06 over 400–800 K, the highest yet reported among n- or p-type PbSe alloys.

Discordant bonding also occurs in more complex materials. $CsAg_5TeS_2$ is a newly discovered mixed anion semiconductor with unique structural chemistry. In $CsAg_5TeS_2$, the Te and S atoms occupy unique crystallographic positions, and the crystal structure moreover features heteroleptic Ag atoms in tetrahedral coordination, i.e. Ag coordinated to both Te and S ($AgTe_2S_2$).[224] While single crystal X-ray diffraction studies suggest the tetragonal space group *P4/mmm*, pair distribution function directly shows the heteroleptic Ag atoms are locally off centered from the center of the tetrahedron to give a lower symmetry *I4/mcm* structure. DFT calculations suggest the discordant Ag atoms induce low frequency optical phonons which strengthen the phonon scattering and yield glasslike lattice thermal conductivities under 0.4 W m^{-1} K^{-1} at 300 K. Indeed, the experimental lattice thermal conductivities are considerably suppressed compared to those estimated from Debye-Callaway type models that do not consider the discordant nature of the heteroleptic Ag atoms

3.2 Dislocations

The incorporation and role of dislocations in thermoelectric materials is currently evoking great interest. Dislocation cores and strain fields give respective phonon relaxation times τ_{DC} α ω^{-3} and τ_{DS} α ω^{-1} and therefore can effectively scatter mid-frequency heat-carrying phonons and result in a significant reduction of κ_L.[163, 225] Currently many researches claim dislocation-induced reduction in κ_L without providing an estimation of dislocation density. Based on Klemens' theory, the effective scattering of mid-frequency phonons requires the dislocation density to be larger than 10^{12} cm^{-2}.[117]

Pei's group designed dense dislocation networks in a $Pb_{1-x}Sb_{2x/3}Se$ solid solution by vacancy engineering,[45] in stark contrast to the dislocation-free stoichiometric alloy $Pb_{1-x}Sb_xSe$. The dislocations are formed by collapse of the intentionally induced Pb vacancies, and the dislocation concentration can be controlled by tuning the x value in $Pb_{1-x}Sb_{2x/3}Se$. Direct observations by scanning TEM (**Figure 11a**) and indirect calculations from synchrotron XRD provide a consistent estimate of the dislocation density of ~4-5×10^{12} cm^{-2} for the x=0.05 sample (i.e. $Pb_{0.95}Sb_{0.033}Se$). This value is nearly an order of magnitude higher than that generated in liquid phase sintered-samples.[226] As a consequence, an ultralow κ_L of 0.4 W m^{-1} K^{-1} was obtained (**Figure 11b**), comparable to the minimum value theoretically predicted by Cahill's model. The remarkable κ_L reduction is mainly ascribed to the additional phonon scattering by dislocation networks, as intrinsic phonon-phonon interactions and point defect scattering cannot produce such a low κ_L. It is noteworthy that the presence of complex dislocations in $Pb_{1-x}Sb_{2x/3}Se$ makes the temperature-dependent mobility (T<500 K) deviate from the function of $\mu_H \sim T^{-2.25}$ normally observed in pristine n-type PbSe. Instead, the interplay of dislocation- Instead, the interplay of dislocation-dominated carrier scattering gives $\mu \sim T^{1.5}$, similar to ionized impurity scattering. However, $Pb_{1-x}Sb_{2x/3}Se$ samples still exhibit a relatively high carrier mobility due to dielectric screening effects. The dense dislocation cores together with concomitant dislocation strains enhance the scattering of mid-range frequency phonons, hence contributing to outstanding ZT values of ~1.5 at 850 K. Similar results were achieved by Lee *et al*, who reported low thermal conductivity for $Pb_{1-x}Sb_xSe$ and also achieved excellent ZT near 1.5 at 800 K.[227]

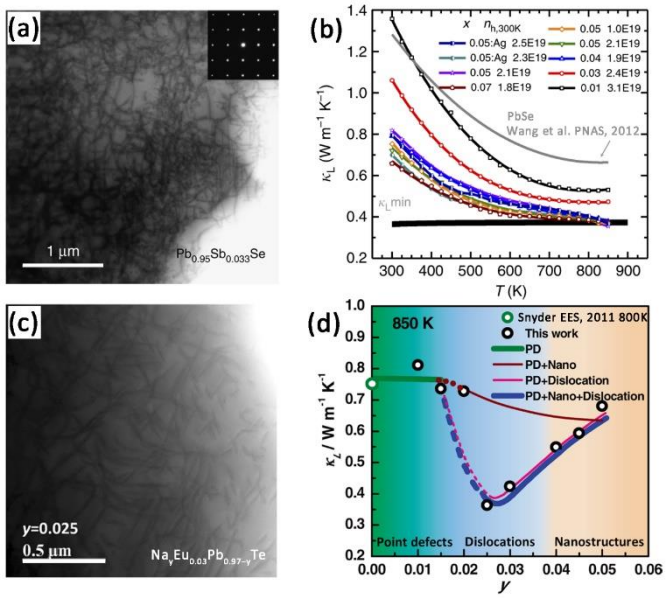

Figure 11. (a) TEM image showing dense dislocations in $Pb_{0.95}Sb_{0.033}Se$ solid solution. The inset is the selected-area electron diffraction (SAED) image of the corresponding area. (b) Temperature-dependent lattice thermal conductivity (κ_L) of $Pb_{1-x}Sb_{2x/3}Se$ (x=0.01, 0.03, 0.04, 0.05 and 0.07) with or without Ag doping. The grey line is taken from literature.[228] Reproduced with permission from ref[45]. Copyright 2017, Nature Publishing Group. (c) TEM image of $Na_yEu_{0.03}Pb_{0.97-y}Te$ (y=0.025) with dense dislocation networks. (d) Composition-dependent lattice thermal conductivity for $Na_yEu_{0.03}Pb_{0.97-y}Te$ at 850 K. The symbols show the experimental results in the cited work[162] (black) and from literature[229] (green), while the curves show the model predictions (with both N- and U-process included) based on a Debye approximation with different types of phonon scattering. Phonon scattering by dislocations has the largest contribution to the reduction in κ_L in this material. Dashed lines are used as visual guides only. Reproduced with permission from ref[162]. Copyright 2017, Wiley-VCH.

Aliovalent impurities can also be intentionally added to introduce dislocations in Na-doped $Pb_{1-x}Eu_xTe$ and $Mg_2Si_{1-x}Sb_x$ compounds.[162, 230] Pei *et al.* reported a high density of dislocations in Na-doped $Pb_{1-x}Eu_xTe$ by varying the Na content, as shown in **Figure 11c**.[162] When the Na concentration is above 2 at% in $Na_yEu_{0.03}Pb_{0.97-y}Te$, both the dislocation density and

number of nanoprecipitates increase. The concentration of dislocation networks reaches a maximum of (~4×10^{12} cm^{-2}) for y=0.025. As a result, an extremely low κ_L of ~0.4 W m^{-1} K^{-1} (**Figure 11d**) and a high *ZT* of ~2.2 were obtained.

Recently, Zhao and co-workers reported dense dislocations in $Mg_2Si_{1-x}Sb_x$ compounds (when x > 10%) and investigated their influences on the thermal transport properties.[230] Mg vacancies are formed when Sb substitution is over 10%, which introduces strong strain fluctuation into the lattice. Hence, dense dislocations and Mg vacancies together contribute to the scattering of both high- and mid-frequency phonons and give a significant decrease of κ_L. Hot deformation is also a promising technique to introduce dislocations in TE materials, such as Bi_2Te_3-based alloys[29] and $FeSb_2$ compounds.[231] The combination of dislocations and other induced defects enhances the scattering of a broader part of the spectrum of phonons giving rise to the κ_L reduction and enhanced *ZT* values.

Liquid phase compaction was applied to prepare Yb-filled $CoSb_3$ with dense dislocation arrays.[118] The excess Sb partially combines with Yb to form $YbSb_2$ impurity phase in the melting and spinning process. The $YbSb_2$ + Sb eutectic phase can be expelled out in the hot press process at 1023 K, producing dense dislocations at the grain boundaries (density ~ 4-8×10^{10} cm^{-2}). Kim *et al* intentionally added excess tellurium in $Bi_{0.5}Sb_{1.5}Te_3$ and utilized liquid phase sintering to squeeze out the additional tellurium.[226] This sintering process yielded dense dislocation arrays (density ~ 2×10^{11} cm^{-2}) at the grain boundaries of the $Bi_{0.5}Sb_{1.5}Te_3$ compounds which exhibited a low κ_L of 0.33 W m^{-1} K^{-1} at 320 K. The authors ascribed the purported high *ZT* values of 1.86 to the effective phonon scattering by dislocation arrays. Recently, Tang and co-workers reported the same dislocation networks in anisotropic TE transport properties of $Bi_{0.5}Sb_{1.5}Te_3$ alloys prepared in the same way (utilized liquid phase sintering to squeeze out the additional tellurium). However, while they measured low κ_L,they also found the dislocation networks in $Bi_{0.5}Sb_{1.5}Te_3$ alloys do not necessarily contribute to the enhanced *ZT* values through κ_L reduction. Instead, the high performance could only be replicated using in plane electrical and out of plan thermal measurements.[232] Consequently, a maximum *ZT* value of 1.24 was obtained at 350 K, far below the value reported by Kim and coworkers and consistent with previous works on $Bi_{2-x}Sb_xTe_3$.[226] This study highlights the importance of consistent measurements for both electrical and thermal transport properties in anisotropic materials. Moreover, the effect of dislocations on the thermal conductivity of Bi_2Te_3-based materials should be carefully evaluated.

3.3 Planar defects

The most common planar defects in TE materials include grain boundaries (GBs), phase boundaries, twin boundaries and stacking faults, all which have significant impact on phonon and carrier transport. Here, grain boundaries refer to the interfaces between grains in polycrystalline samples, while phase boundaries are the interfaces between different phases, such as between a host matrix and secondary precipitates. Given the pronounced difference between the mean free paths of charge carriers and phonons, grain boundary engineering is an effective way to introduce interfaces and enhance the scattering of low-frequency phonons at grain boundaries, resulting in a remarkable reduction of κ_L.[118]

In the past decades, extensive approaches have been developed to introduce nanostructures or hierarchical structures in state-of-the-art TE materials. The most popular methods include ball milling,[25] melt-spinning,[233] and solution-based processes.[234]

Ball milling processing involves mechanical alloying and mechanical grinding, which can be used to either form alloys or pulverize samples. It has been employed in preparing nanostructured SiGe alloys,[235, 236] half-Heuslers,[237] BiCuSeO,[238] Zintl compounds,[178, 239] metal chalcogenides[25, 240-243] and skutterudites.[244]

Melt spinning is another efficient approach to manipulate the microstructure of TE materials using kinetic control. Melt spinning is particularly suitable for preparation of metastable forms of compounds using high cooling rates of 10^4-10^7 K min^{-1}. This technique has been advanced by Tang's group to refine microstructures and introduce nanocrystallites in state-of-the-art TE materials, such as Bi_2Te_3-based alloys,[232, 233] skutterudites[245] and silicides.[246, 247] Melt-spun BiSbTe alloys exhibit unique microstructures that consist of 5–15 nm nanocrystals with coherent grain boundaries and nanocrystalline domains embedded in an amorphous matrix[233] (as shown in **Figure 12a-b**). Remarkable reductions in κ_L (**Figure 12c**) and over 50% enhancement of *ZT* compared to the commercial ingot materials have been achieved.

In addition to powder metallurgy methods, solution-based synthesis has shown great potential in grain boundary engineering for TE materials.[97, 248, 249] Solution-based routes have several advantages over solid-state synthesis, in particular low reaction temperature and facile control of microstructures. Numerous metal chalcogenide nanocrystals have been synthesized in solution, including PbTe, Cu_2Se, SnSe, and Bi_2Te_3-based compounds. In combination with high temperature consolidation process, solution grown nanocrystals are subject to grain growth and compressed into bulk materials, thus generating a high-density of grain boundaries inside the final pellets. For instance, solvothermal-synthesized Cu_2Se nanoplates have a wide distribution of lateral size from several hundred nanometers to 1 μm.[250] The post-synthetic sintering process preserved the plate-like morphology and nanoscale size of the grains which enhanced the scattering of intermediate and low frequency phonons, resulting in an ultralow κ_L of 0.2 $Wm^{-1}K^{-1}$. In addition, because grain boundaries also can serve as barriers to scatter charge carriers, they can feasibly be used to selectively filter those with energy lower than the barrier height,.[251]but because the barriers will also sharply decrease the electrical conductivity, strong evidence for an overall beneficial energy filtering effects remains lacking.

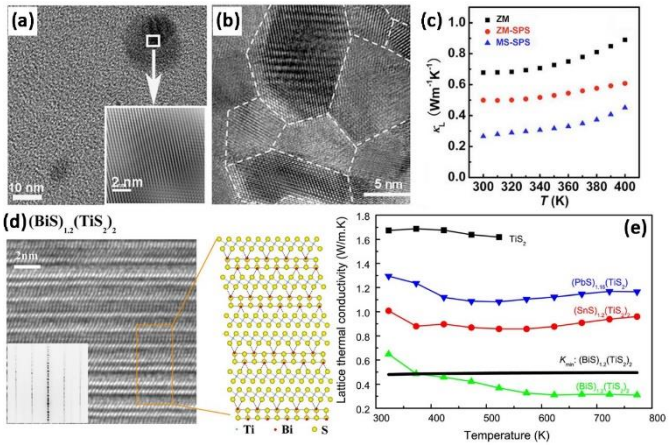

Figure 12. (a) and (b) TEM images of melt-spun-SPS (MS-SPS) bulk materials, which display both the nanocrystalline domains and amorphous phase. (c) The lattice thermal conductivity (κ_L) of zone-melted (ZM) ingot, ZM-SPS, and MS-SPS bulk samples as a function of temperature. Reproduced with permission from[233]. Copyright 2009, The American Institute of Physics. (d) TEM image (left) and simulated crystal structure (right) of $(BiS)_{1.2}(TiS_2)_2$ along the [100] zone axis. The inset shows the electron diffraction pattern of the sample. (e) Temperature dependent in-plane lattice thermal conductivity of TiS_2, $(PbS)_{1.18}(TiS_2)_2$, $(SnS)_{1.2}(TiS_2)_2$, and $(BiS)_{1.2}(TiS_2)_2$. The black solid line indicates the minimum thermal conductivity of $(BiS)_{1.2}(TiS_2)_2$ calculated by Cahill's model. Reproduced with permission from ref[120]. Copyright 2012, The American Institute of Physics.

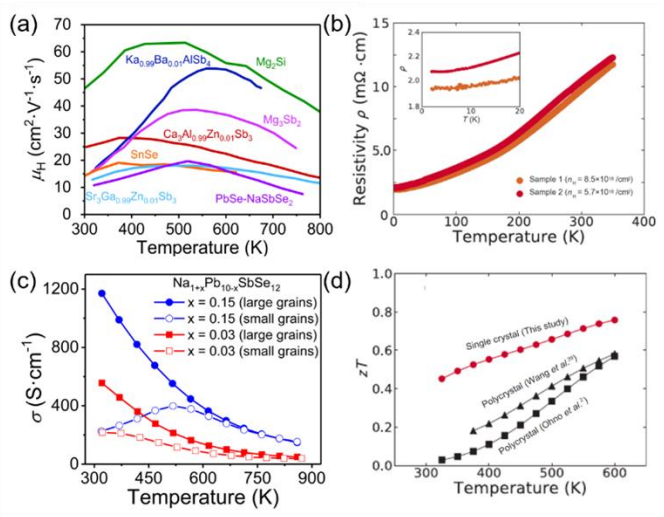

Figure 13. (a) Traces of the temperature–dependent Hall carrier mobility in several high performance and promising thermoelectric materials with strong grain boundary scattering, $KAlSb_4$,[52] Mg_3Sb_2,[190] Ca_3AlSb_3,[255] Sr_3GaSb_3,[266] SnSe,[267] PbSe-NaSbSe$_2$,[258] and Mg_2Si.[268] (b) Electrical resistivity of two degenerate n-type single crystals of Mg_3Sb_2 showing metallic behavior down to 2 K with no evidence for ionized impurity scattering. Reproduced with permission from[263]. Copyright 2020, John Wiley & Sons, Inc. (c) Comparison of the electrical conductivities for large– and small–grained PbSe–NaSbSe$_2$ showing elimination of the low-temperature scattering in the large–grained samples. Reproduced and adapted with permission from[258]. Copyright 2019, John Wiley & Sons, Inc.. (d) Demonstration of improved *ZT*s in single crystalline Mg_3Sb_2 compared to polycrystalline materials. Reproduced with permission from[258]. Copyright 2020, John Wiley & Sons, Inc.

As demonstrated by the above examples, grain boundaries can effectively suppress κ_L; however, GBs will also generally degrade the electronic transport and decrease the carrier mobility μ. In traditional thermoelectric materials such as PbTe and Bi_2Te_3, the tradeoff is often favorable, and small grains (high GB density) are desired to obtain the lowest κ_L; however, many emerging TE materials feature unusually strong charge carrier scattering from the GBs that is ultimately detrimental to the thermoelectric performance. Examples include, but are not limited to, Mg_3Sb_2[190, 252] and other Zintl antimonides,[52, 253-255], half-Heuslers,[256, 257], and PbSe–ASbSe$_2$ (A = Na Ag) alloys.[258-260].

Here, the GBs are sufficiently resistive to produce anomalous thermally activated electrical conductivity and mobility at lower temperatures (generally below ~600 K), as shown in **Figure 13a**, while the Seebeck coefficient is mostly unaffected. In Mg_3Sb_2, the unusual temperature dependence of the conductivity was initially ascribed to ionized impurity scattering,[190] which can in principle produce similar behaviour; however, later work suggested a grain boundary based scattering model can also reproduce the irregular electrical conductivity while providing a better theoretical description of the Seebeck coefficients.[261] The most convincing evidence for GB scattering came from measurements on single crystals and large grain samples that demonstrated elimination of the deleterious scattering as the grain size increased, and in the case of the single crystals, lacked evidence for ionized impurity scattering down to 2 K (**Figure 13b**).[262, 263] Similarly, large grained samples of PbSe–NaSbSe$_2$ alloys do not show the low temperature scattering found in small grained materials (**Figure 13c**).[264] At a microscopic level, detailed atom probe tomography investigations of the GBs in Mg_3Sb_2 reveals significant (up to 5%) Mg deficiency along the interfaces.[265]

Recent work suggests more ionic semiconductors will in general be more prone to detrimental GB scattering owing to the weakened dielectric screening of the charge carriers.[269] This is consistent with the above picture, where Zintl antimonides often show GB dominated transport, while more polarizable traditional materials like Bi_2Te_3 do not. In such cases, any gains owing from reduced κ_L in small–grained samples are overtaken from the severe increase in resistance at the grain boundaries and the overall thermoelectric performance often suffers. Even in cases where the maximum *ZT* is somewhat higher in small-grained materials, the suppression of the electrical conductivity, particularly at lower temperatures, generally leads to lower device ZT_{dev}. The above example materials therefore represent exceptions to the widely accepted notion that small grains are preferable in thermoelectric materials. Here, large-grained microstructures may be favorable to suppress GB scattering and maintain high charge carrier mobility. Indeed large grained and/or single crystalline forms of Mg_3Sb_2 and SnSe are reported to show considerably better thermoelectric performance than small grained or polycrystalline counterparts, as shown in **Figure 13d** for Mg_3Sb_2.[262, 270, 271] Further in support of this claim, suitable processing of polycrystalline SnSe to suppress the GB scattering yielded samples with comparable figures of merit to the single crystals.[272]

Electrically resistive GBs can also lead to dramatic over estimations of the lattice thermal conductivity. In a recent publication, Kuo *et al.* demonstrated how typical use the of Wiedemann Franz law to estimate κ_{elec} and may result in significant errors when GB scattering is strong.[273] When the GBs

are sufficiently resistive to dominate the electrical conductivity, the usual implementation of the Wiedemann Franz law neglects heat transported by charge carriers moving through the bulk grains, leading to underestimation of the true κ_{elec} and thus overestimation of κ_L. In some extreme cases, such as SnSe, this leads to an obvious contradiction where the polycrystalline forms have apparently larger κ_L than single crystals. While SnSe is a particularly dramatic example, Kuo *et al* show significant GB effects are pervasive in the TE literature, indicating care must be taken to properly estimate the electronic and lattice thermal conductivity in small grained thermoelectric materials.

While GB engineering is often a powerful means of improving the TE performance, the above works demonstrate the influence of GBs can also be malignant. A simple rule of thumb available to researchers is that more ionic materials are more likely to exhibit negative effects from the GBs, whereas the GBs in polarizable materials like PbTe will largely be benign. In either case, we emphasize the importance of both properly characterizing and considering the overall contribution of the grain boundaries and engineering the proper microstructure to optimize the trade-off between κ_L and μ.

Lastly, stacking faults are observed in a number of TE materials and their composites, such as $Cr_2Ge_2Te_6$,[274, 275] $InSiTe_3$,[275] $Sb_2Si_2Te_6$,[276] TiS_2-based misfit-layered compounds[120, 277, 278] PbTe-$PbSnS_2$ composites,[279] $SrTiO_3$-based oxides,[204] MgAgSb alloys,[280, 281] etc. Wan *et al* reported the natural superlattice structures in $(MS)_{1+x}(TiS_2)_2$ (M=Pb, Sn, Bi) bulk materials[120] in which the MS layers are intercalated naturally into the van der Waals gap of TiS_2 and stack periodically. The resulting misfit layers can suppress phonon transport and lead to a low κ_L in the direction perpendicular to the layers. By controlling the stacking faults of the MS and TiS_2 layers, the κ_L can be progressively reduced (**Figure 12d-e**). Due to the high density of stacking faults, $(BiS)_{1.2}(TiS_2)_2$ shows even lower κ_L than the minimum value calculated by Cahill's model at high temperature (**Figure 12e**). In addition, prolonged ball milling process and subsequent heat treatment were found to introduce high-density stacking faults in α-MgAgSb alloys that could result in enhanced scattering of medium-wavelength phonons.[280]

3.4 Volume defects

3.4.1 In-situ nanoinclusions. In-situ inclusion of nanostructures is of great importance in the TE community, as the precipitates act as efficient phonon scattering centers, thus enabling efficient modulation of the thermal transport properties in various TE systems. It is particularly desirable during a nucleation and growth or spinodal decomposition process that the interface created between the two phases is as coherent as possible, a phenomenon referred to as *endotaxy*. This is because such an interface can effectively scatter phonons and at the same time (if there is good electronic band alignment between the two phases) easily transmit charge carriers. Traditionally, in-situ nanoinclusions are naturally formed (i.e. without milling or secondary processing) using solid state phase transformations, as detailed by following techniques:

(1) Phase separation of instable solid solutions through spinodal decomposition.

Precipitates effectively lower the κ_L of a host material if their sizes are on nanoscale.[282] Phase separation can be controlled on

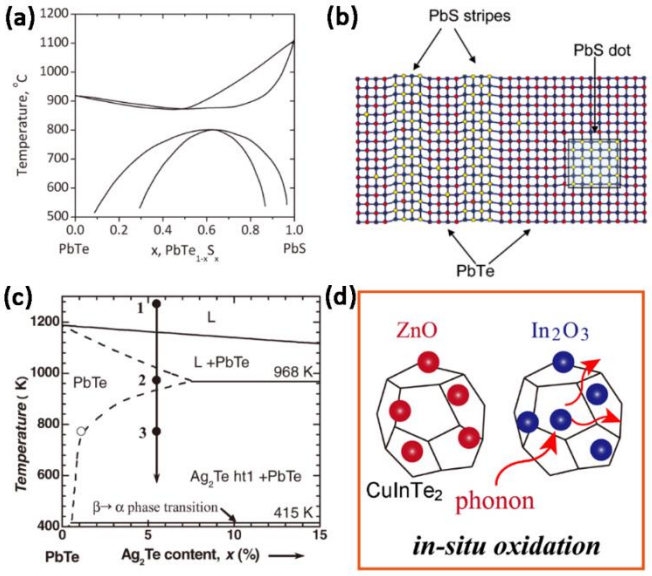

Figure 14. (a) Phase diagram of PbTe-PbS. Reproduced with permission.[283] Copyright 2012, WILEY-VCH. (b) Schematic illustration of PbS precipitates in PbTe. Reproduced with permission from ref[284]. Copyright 2007, The American Chemical Society. (c) Phase diagram of PbTe-Ag_2Te. Reproduced with permission from ref[285]. Copyright 2011, WILEY-VCH. (d) Schematic diagram of in-situ oxidation in $CuInTe_2$-ZnO and $CuInTe_2$-In_2O_3 systems. Adapted with permission from ref. [286] Copyright 2018, Chinese Physical Society and IOP Publishing Ltd.

nanometer scale in materials that undergo spinodal decomposition. As a representative example, the PbTe-PbS system exhibits a miscibility gap (**Figure 14a**).[287] Sufficient thermodynamic driving force for spinodal decomposition is reached when pushing the alloy far from equilibrium and into the unstable miscibility gap region. For a given isotherm over the composition range, phase segregation reduces the overall free energy of the system because of the curvature in the Gibbs free energy.[283] Moreover, the precipitate morphology (e.g size and shape) can be controlled to some extent by the nucleation and growth mechanism. **Figure 14b** schematically highlights nanoscale PbS-rich stripes created by spinodal decomposition and nanocrystals of PbS precipitated in a PbTe matrix.[284] Microstructural investigation indicates the in-situ formed PbS leads to dense dislocations and lattice strains at the PbS/PbTe grain boundaries due to the large lattice mismatch of ~ 6% between PbTe and PbS.[288] Comparison of single phase and nanostructured PbTe-PbS composites found significantly lower κ_L in the nanostructured forms,[289] providing strong evidence that the unique nanostructure facilitates a large reduction in κ_L and high TE performance owing to the enhanced phonon scattering.

Androulakis *et al* found a very low $\kappa_L \sim 0.4$ $Wm^{-1}K^{-1}$ at room temperature for the composition of 8% PbS in PbTe owing to the strong phonon scattering from acoustic impedance mismatch at interfaces, comparable to that of artificial thin film

superlattice structures (~0.33 W m^{-1} K^{-1}). Such a low κ_L enables a high *ZT* value of 1.50 at 642 K.[284] Girard *et al* reported successful shape control of the PbS nanostructures in Na-doped PbTe-PbSe by modulating the concentrations of Na and PbS, yielding cuboctahedral PbS nanocrystals coherently embedded throughout the PbTe matrix. Here, low κ_L values (~0.5 W m^{-1} K^{-1} at ~800 K) combined with high power factor (~2×10^{-3} W m^{-1} K^{-2} at ~800 K) result in a maximum *ZT* of ~1.8 at 800 K for 2% Na-doped PbTe- 12 %PbS sample.[287] Wu *et al* reported an even greater *ZT* of ~2.3 at 923 K for a spark plasma sintered 3 at% Na-doped $(PbTe)_{0.8}(PbS)_{0.2}$ sample.[290] The superior performance was attributed to the further decrease of κ_L (~0.38 W m^{-1} K^{-1} at 923 K) derived from the mesostructured microstructure and the very high power factors (up to 2.65×10^{-3} W m^{-1} K^{-2} at 623 K).

In addition to the PbTe-PbS system, the quasi-binary PbTe-GeTe [291, 292] is also a classic system Formed by spinodal decomposition. By Sn alloying, Gelbstein[293] *et al* formed a periodic distribution of GeTe- and PbTe-rich phases at the micro- and nano- (down to 10 nm) scales, yielding a ~50% reduction of the room temperature κ_L (~0.8 W m^{-1} K^{-1}) and a high *ZT* of ~1.2 at 723 K in $Ge_{0.5}Sn_{0.25}Pb_{0.25}Te$ alloy. Further metallurgical control[294] over the phase separation by spark plasma sintering and subsequently heat treatment induced sub-micron phase separated domains along with twinning and dislocation networks in PbTe-GeTe, which results in an ultralow κ_L of ~0.4 W m^{-1} K^{-1} and a very high *ZT* of up to ~2 at 723 K for p -type $Ge_{0.87}Pb_{0.13}Te$ alloys.

Outside of the lead and/or tin chalcogenide-based alloys, spinodal decomposition has been widely utilized in other TE materials to introduce in-situ nanoinclusions. Meng *et al*[295] observed spinodal decomposition in the skutterudite $La_{0.8}Ti_{0.1}Ga_{0.1}Fe_3CoSb_{12}$ synthesized by a rapid solidification method (i.e. melting–spinning). In this compound, coherent La-poor and La-rich skutterudite grains with sizes of ~200 nm were achieved, rendering a ~30% reduction in κ_L (~0.75 W m^{-1} K^{-1}) and ~50 % increment in *ZT* (~1.2) at 700 K compared to quenched samples. Gürth *et al*[296] studied the $Ti_{1-x}Hf_xNiSn$ and $Ti_{1-x}Zr_xNiSn$ half-Heusler system, which undergoes spinodal decomposition when prepared with an optimized arc melting technique consisting of an intermediate high frequency melting step, a long ball milling time, and a multi-step hot pressing. The resulting nano precipitates strongly scatter heat-carrying phonons and lead to lower κ. The *ZT* values reach up to ~1 for ternary TiNiSn and ZrNiSn, and ~1.2 for $Ti_{0.5}Zr_{0.5}NiSn_{0.98}Sb_{0.02}$.

Preparation of half-Heusler (HH) materials containing nanoscale precipitates of full-Heuslers (FH) coherently embedded in the bulk matrix has furthermore been demonstrated to favorably modulate both phonon scattering and charge transport properties.[297] Polycrystalline samples of the HH $Zr_{0.25}Hf_{0.75}NiSn$ containing 2–6 percent fractions of FH $Zr_{0.25}Hf_{0.75}Ni_2Sn$ nano inclusions (under 10 nm) exhibit enhanced charge carrier mobility and simultaneous reduction of κ to give significantly improved performance.[298] Similar results were also achieved in composites of HH $Ti_{0.5}Hf_{0.5}CoSb_{0.9}Sn_{0.1}$ with the FH $Ti_{0.5}Hf_{0.5}Co_2Sb_{0.9}Sn_{0.1}$, where the inclusion of FH nanoprecipitates in the HH matrix raises both the charge carrier mobility and thermopower as well as reducing the thermal conductivity of highly degenerate samples.[299] These surprising results are ascribed to the trapping of low energy charge carriers at the HH/FH interface, lowering the net hole density and increasing the carrier relaxation time and thus mobility. Likewise, the lowered carrier concentration leads to improvement in the Seebeck coefficients. Lastly, recent work indicates growth of magnetic $Ti(Ni_{4/3}Fe_{2/3})Sn$ FH nanoparticles in a $Ti_{0.25}Zr_{0.25}Hf_{0.5}NiSn_{0.975}Sb_{0.025}$ HH matrix can significantly improve the thermopower, which is suggested to be the result of interactions between the magnetic moments of the FH precipitates with the spins of itinerate electrons. This leads to charge localization and the formation of bound magnetic polarons, which may enhance the carrier effective mass and improve the thermopower.[300]

(2) Precipitation from a metastable supersaturated solid solution. Nucleation and growth.

In general, stable precipitates with good thermal stability can be achieved based on their low solubilities in the host matrix. As shown in the phase diagram of the pseudobinary PbTe-Ag_2Te[285] (**Figure 14c**), the solubility of Ag_2Te in PbTe is strongly temperature-dependent. By rationally adjusting the composition, phase separation of PbTe and Ag_2Te occurs when the Ag_2Te fraction is over its solubility limit. Therefore, precipitates can be grown in the host matrix without system restrictions. Using this concept, Biswas et al[301] incorporated endotaxially arranged SrTe nanocrystals (~1–15 nm) in Na_2Te doped PbTe matrix and found the SrTe has little effect on hole mobility but significant suppresses heat propagation, therefore decoupling phonon and electron transport in the system. The resulting high power factor (2×10^{-3} W m^{-1} K^{-2} at ~800 K) and low κ_L (~0.45 W m^{-1} K^{-1} at ~800 K) led to the then highest *ZT* of 1.7 at 815 K for the 2% SrTe sample. Tan *et al* extended this work, using a rapid quenching procedure to trap SrTe beyond its thermodynamic solubility limit of <1 mol% in PbTe. The increased alloy fraction of SrTe promotes greater convergence of *L* and *Σ* valence bands and also widens the bandgap. As a result, the non-equilibrium processing rendered much higher power factors with maximal values over 3×10^{-3} W m^{-1} K^{-2}. In addition, the endotaxial SrTe nanostructures yield low κ_L of ~0.5 W m^{-1} K^{-1} at 923 K in the heavily doped PbTe-SrTe system. Consequently, $Pb_{0.98}Na_{0.02}Te$–8%SrTe achieves a record high *ZT* value of 2.5 at 923 K.

Zhou *et al*[302] reported that bismuth is multifunctional in SnTe compounds. Bismuth can modulate the carrier concentration and increase the density of states effective mass of SnTe for high power factor (2×10^{-3} W m^{-1} K^{-2} at 873 K). Bismuth will also precipitate from the SnTe matrix when the doping level exceeds 4 at%. The nanoscale bismuth precipitates act as phonon scattering centers and largely reduce κ_L of (~0.7 W m^{-1} K^{-1} at 873 K). Compared to pure SnTe, $Sn_{0.94}Bi_{0.06}Te$ has considerably improved performance with a *ZT* of 1.1 at 873 K. To reduce the κ_L of bismuth doped SnTe without deteriorating the hole carrier mobility, Zhao *et al*[303] incorporated endotaxial SrTe nanostructures as phonon scattering centers. The nanostructures lower the κ_L from ~1.1 W m^{-1} K^{-1} for $Sn_{0.97}Bi_{0.03}Te$ to ~0.70 W m^{-1} K^{-1} for $Sn_{0.97}Bi_{0.03}Te$-

5.0% SrTe at 823 K, leading to a *ZT* of 1.2 at 823 K and a high average *ZT* of 0.7 in the temperature range of 300–823 K.

Luo *et al*[304] found nanoscale Ag_8SnSe_6 precipitates can further reduce the already ultralow κ_L of polycrystalline SnSe to 0.32 W m^{-1} K^{-1} at 773 K. Such a low κ along with the high power factor caused by Ag/Na dual doping achieves a peak *ZT* of 1.33 at 773 K with a high average *ZT* (ZT_{ave}) value of 0.91 in the temperature range of 423–823 K for the SnSe system. By directly incorporating excess ZnS, Luo *et al*[305] created nanoscale ZnS secondary precipitates with dense stacking faults in a $CuInTe_2$ matrix. The unique precipitates result in a ~40% reduction in κ_L for $CuInTe_2$-6 mol% ZnS (~0.42 W m^{-1} K^{-1}) compared to $CuInTe_2$ (0.72 W m^{-1} K^{-1}) at 823 K. The resulting *ZT* value reaches ~1.52 at 823 K for an increase of ~90%.

Eutectic-precipitation[306] is a special strategy for incorporating nanoscale or submicron phases into the host TE materials. Owing to the interlaced nature of eutectic phase separation, most of the resulting products are lamellar with controllable sizes.[307] In this way, Bhardwaj *et al*[308] prepared metallic submicron lamellar eutectic phase of $Ti_{70.5}Fe_{29.5}$ in the half-Heusler TiNiSn matrix. The incorporation of the lamellar $Ti_{70.5}Fe_{29.5}$ results in a ~57% increase in the power factor (compared to TiNiSn) and a ~25% reduction in κ. The *ZT* of the $Ti_{70.5}Fe_{29.5}$ containing samples is twice that of pristine TiNiSn. Cheng[309] and Xin[310] *et al* studied the effect of in-situ grown InSb–Sb eutectic structures on the TE properties of InSb. They found the InSb–Sb eutectic melts into a liquid phase beyond 765 K, and the obstruction of the transverse acoustic phonons drastically reduces κ_L. Zhang *et al*[311] found lamellar MnTe and particle-like $MnTe_2$ precipitates form in $Pb_{1-x}Mn_xTe$ when the Mn content exceeds its solubility limit in PbTe. The discontinued nanometer or micrometer-sized $MnTe_2$ precipitates act as strong phonon scattering centers, which reduce κ_L from ~1.69 W m^{-1} K^{-1} for PbTe to ~1.16 W m^{-1} K^{-1} for $Pb_{0.94}Mn_{0.06}Te$ at room temperature.

It is furthermore important to consider the stability of the nanoprecipitates. For practical thermoelectric applications, it is imperative for the nano inclusions to be stable over long periods at the desired operating temperatures. An interesting example of in-situ changes to the micro-nanoscale structure that occurs at relevant temperature is found in the $NaPb_mSbTe_{m+2}$ (PbTe–$NaSbTe_2$) alloy system. $NaPb_mSbTe_{m+2}$ is a classic nanostructured thermoelectric material in which Na- and Sb-rich nano structures give rise to low lattice thermal conductivity and high *ZT* ~ 1.6 near 700 K.[312] Surprisingly, recent work demonstrated the secondary phases present in the as-cast ingots dissolve during sintering or hot pressing to give a single phase solid solution.[313] The dissolution of the secondary phases causes a shift from degenerate p-type conduction to nearly intrinsic n-type charge transport, and the resulting solid-solutions have considerably poorer *ZT*s then the phase separated ingots. High performance can be recovered by tuning the cation stoichiometry; however, this work clearly demonstrates the need to fully characterize the thermal stability of precipitates and secondary phases in thermoelectric materials.

(3) In-situ nanoinclusions formed by chemical reaction.

In-situ chemical reactions (e.g. replacement, oxidation) are a new strategy to induce desired dispersed nanoinclusions within the host matrix.[314] Luo *et al*[315] incorporated TiO_2 nanoparticles, nanotubes, and nanofibers in $CuInTe_2$. The TiO_2 additives reacted with $CuInTe_2$ during the hot pressing at the onset temperature of ~623 K, forming well dispersed In_2O_3 inclusions with sizes of ~30 nm. The presence of In_2O_3 nanoinclusions results in ~33% reduction of κ_L (~0.48 W m^{-1} K^{-1}) compared to pure $CuInTe_2$ (~0.72 W m^{-1} K^{-1}) at 823 K. By further alloying with ZnTe to enhance the power factor, the TiO_2 nanofiber containing $(CuInTe_2)_{0.99}(2ZnTe)_{0.01}$ reaches a high *ZT* ~1.47 at 823 K. Furthermore, ZnO nanoparticles were incorporated into $CuInTe_2$ to simultaneously modify its electrical and thermal transport properties.[316] The reaction between ZnO and $CuInTe_2$ leads to hole doping of Zn at the In sites and formation of In_2O_3 nanoinclusions (**Figure 14d**). Consequently, the power factor increases by ~ 76% (~1.45×10^{-3} W m^{-1} K^{-2}) and the κ_L reduced by 34% (0.47 W m^{-1} K^{-1}), enabling the $CuInTe_{1.99}Sb_{0.01}$+1.0 wt% ZnO sample to achieve a record high *ZT* of ~1.61 at 823 K. Ahmad [317] demonstrated Y_2O_3 nanoparticles (average size of 60 nm) can react with SiGe to form an in-situ metallic YSi_2 phase which exhibits coherent grain boundaries with SiGe. The coherent grain boundaries scatter phonons but allow charge carriers to pass through, resulting in very low κ (~0.56 W m^{-1} K^{-1} at 1100 K) without altering the power factor. As a result, a record *ZT* of 1.81 at 1100 K is observed, which is an increase of ~34% compared to SiGe. Favier *et al* [318] observed nanosized (~30 nm) $MoSi_2$ inclusions in an n-type SiGe matrix. Here, the nanoinclusions were formed during sintering via an in-situ reaction between the native SiGe and added molybdenum. The presence of the nanosized inclusions significantly reduces κ_L from 4.8 W m^{-1} K^{-1} for SiGe to 3.6 W m^{-1} K^{-1} for 1.3 vol% incorporated SiGe at 973 K,and the resulting material exhibits a *ZT* of ~1.0 at 973 K.

Elsheikh *et al* [319]found Al atoms tend to react with Sb and form AlSb nano-inclusions in the grain boundaries instead of entering the Sb-icosahedral voids in composites of $Yb_{0.25}Co_4Sb_{12}$ and Al. The AlSb inclusions are suggested to act as barriers for both low energy charge carriers and phonons, leading to a high power factor of 4.89×10^{-3} W m^{-1} K^{-2} at 650 K for $Al_{0.1}Yb_{0.25}Co_4Sb_{12}$ and a low κ_L of 0.6 W m^{-1} K^{-1} at 500K for $Al_{0.3}Yb_{0.25}Co_4Sb_{12}$. The *ZT* was enhanced up to 1.36 at 850 K for $Al_{0.3}Yb_{0.25}Co_4Sb_{12}$. Kim *et al*[320] incorporated TeO_2 nanoparticles into $Bi_{0.5}Sb_{1.5}Te_3$. The *in-situ* reaction between Sb and TeO_2 during ball milling and spark plasma sintering resulted in the formation of Sb_2O_3 nanoinclusions in the samples. The Sb_2O_3 significantly reduces the κ_L by ~23% at 300 K (~0.44 W m^{-1} K^{-1}). As a result, the $Bi_{0.5}Sb_{1.5}Te_3$-3 wt%TeO_2 sample achieves a *ZT* of 1.07 at 350 K.

Furthermore, redox engineering has been successfully applied to introduce *in-situ* nanoinclusions in oxide TE materials.[203, 321] This strategy requires cations have multiple valence states that can be easily tuned via the redox reactions with atmosphere. For example, the incorporation of redox-sensitive Mo cations in A-site deficient $Sr_{1-x}(Ti,Mo)O_3$-based materials results in the Mo exsolution and the formation of Mo

nanoinclusions. This is due to the chemical reactions between the secondary phases of $SrMoO_4$ and TiO_2, [203]

$$SrMoO_4 + TiO_2 \rightarrow SrTiO_3 + Mo + 1.5O_2,$$

The intrinsically high refractoriness of Mo could account for the dispersion of Mo in the nanoscale and submicron-scale located at grain boundaries. The in-situ Mo nanoinclusions and atomic inhomogeneities can serve as effective phonon scattering centers, resulting in reduced κ_L for the obtained nanocomposities. Similarly, other metallic nanoinclusions with high melting point have also been introduced in $SrTiO_3$-based compounds via the reduction of corresponding oxide or salt precursors.[322, 323]

3.4.2 Exotic secondary phases. We refer to compounds that are chemically unrelated or inert to the primary thermoelectric matrix as exotic secondary phases. The large chemical differences between host matrix and secondary phases mean composites cannot be created via the nucleation and growth, spinodal decomposition, or the other reaction techniques described above. Exotic secondary phases are thus a distinct sub-class of volume defects that can be incorporated by physical means into TE materials to optimize their performance. Since the phonon and electron transport behaviors largely depend on the type, size distribution, and concentration of secondary phases, exotic secondary phases are expected to generate interfaces in host materials which could introduce, either fortuitously or by design, energy filtering effects and enhance the scattering of both phonons and electrons. Therefore, it is critical to understand the nature of the matrix and find suitable additives.

In general, additives are chosen according to the following criteria: 1) high chemical and thermal stability, i.e. they do not react with the matrix material within the operating temperature; 2) formation of a homogeneous distribution in the matrix, i.e. no obvious aggregation. To date, various exotic secondary phases have been used as fillers in state-of-the-art TE materials, such as carbon-based materials (graphene, carbon nanotubes, etc.),[324-330] SiC,[329, 331-334] TiN,[335, 336] oxides,[337] and single elements.[232, 338] These secondary phases are mainly introduced and dispersed *via* powder processing, specifically by mechanical alloying, which facilitates the formation of homogeneous composites. Meanwhile, the secondary phases can serve as barriers to prevent grain growth during heat treatment, such as annealing, hot pressing, and rapid sintering. This in turn increases the density of grain boundaries.

Carbon-based materials, such as carbon, graphene, carbon nanotubes, and fullerene, are emerging as attractive additives in TE materials due to their unique physical properties such as excellent electrical conductivity and good thermal stability.[339-341] The type and dimensionality of carbon sources has significantly different effects on the electrical and thermal transport properties. It is noteworthy that graphene and carbon nanotubes have anisotropic structures, and phonons and charge carriers thus exhibit distinct transport behavior parallel to or perpendicular to the tube/layer. Therefore, the anisotropy of the TE properties for these composites must be taken into consideration.

A very interesting example is the work on Mg_3Sb_2 incorporated with multilayer graphene recently published by Lin et al., where the authors demonstrate an interfacial Seebeck coefficient, similar to the energy filtering effect, that originates in the graphene sheets segregated at the grain boundaries.[342] While energy filtering is commonly invoked in the thermoelectrics literature to explain enhanced performance, rigorous evidence for a beneficial effect is scarce at best. In fact, detailed calculations indicate the typical picture of energy filtering from barriers at grain boundaries or precipitate interfaces can raise *S*, but also will always significantly impede the carrier mobility and thus give negligible true enhancement of the power factor or figure of merit.[343]

In their recent work, Lin et al. use ball milling followed by hot pressing to prepare graphene–Mg_3Sb_2 composites. They find the graphene largely segregates to the grain boundaries, lowering the thermal conductivity across the interfaces. The increased thermal resistance at the boundaries produces an interfacial Seebeck effect, which adds to and enhances the net Seebeck coefficient. Crucially, unlike resistive Schotky barriers normally considered in the context of energy filtering, graphene has outstanding charge carrier mobility allows relatively facile charge transport across the graphene containing boundaries. The overall result is enhanced Seebeck without major losses to the electrical conductivity, resulting in an outstanding *ZT* of 1.7 at 750 K in the graphene- Mg_3Sb_2 samples.

While we believe claims of energy filtering should generally be treated with caution, the above work provides a new perspective in which real enhancement to *ZT* is possible. The key requirement is to increase the thermal resistance of the interfacial region without compromising the electrical conductivity. Because graphene and other carbon–based materials are often outstanding conductors, these may represent useful materials for achieving this effect. As we discuss below, many of the examples of carbon based exotic secondary phases recently studied in thermoelectric semiconductors appear to produce energy filtering effects that are beneficial to the material performance.

Recently, Zhao *et al.* dispersed a wide range of carbon precursors in Cu_2Se, including graphite, carbon black, carbon fibers, and hard carbon.[344] With addition of 0.3 wt% carbon fibers, the composite demonstrated an impressive *ZT* of 2.4 at 850 K. Moreover, in other notable works, the addition of carbon-based nanomaterials such as multi-walled carbon nanotubes[345, 346] and carbon-coated boron nanoparticles[347] also play beneficial roles in Cu_2Se-based composites, which exhibited $ZT > 1$ over a broad temperature range of 600-900 K. The authors ascribed the TE enhancement to more effective scattering of phonons at interfaces than electrons. To elaborate the role of carbon-related precursors in Cu_2Se composites, more advanced experiments and calculation tools are required. The same group carried out further studies on graphene-incorporated Cu_2Se composites and reported the ultra-high *ZT* value of 2.44 at 873 K for Cu_2Se/0.15 wt% graphene composites.[348] A high temperature (~1200 °C) melting process accelerated the diffusion of Cu, Se and C atoms, while graphene nanoplates tend to aggregate to form graphite or remained

unchanged. Both carbon inclusions and multi-layered graphene were found in the composites. Based on the synchrotron XRD results and DFT calculations, they concluded that no solid-state reaction occurred between carbon and Cu_2Se up to high temperature. The large mismatch of phonon density of states between graphene (or graphite) and Cu_2Se largely accounts for the significant reduction of κ.

In addition, Baik *et al* mixed a small portion of graphene (0.1 vol%) in $Bi_{0.5}Sb_{1.5}Te_3$ by ball milling,[349] which simultaneously increased both the carrier concentration and mobility due to the intrinsically high carrier concentration and mobility of graphene.[350] The composites likewise have suppressed κ_L from the enhanced phonon scattering at interfaces and demonstrate maximum *ZT* of 1.13 at 360 K. The $Bi_{0.5}Sb_{1.5}Te_3$/0.1 vol% graphene composites also showed good thermal stability verified by repeated cycling of the TE performance.

Besides mechanical mixing, a wet chemical method has been developed to synthesize PbTe/graphene nanocomposites (**Figure 15a**).[351] Graphene oxide nanosheets served as both the dispersant and growth template for PbTe nanoparticles. The PbTe nanoparticles were formed *in-situ*, while the graphene oxides nanosheets were simultaneously reduced to graphene. The presence of graphene in the composites provides extra transport channels for electrons, resulting in significant enhancement of σ, from 2.29×10^3 S m^{-1} (pristine PbTe) to 3.11×10^4 S m^{-1} (PbTe-5 wt% graphene). Meanwhile the composites exhibited low κ_L and suppressed bipolar thermal conductivity at high temperature, ascribed to enhanced phonon scattering at interfaces and the increased carrier concentration. The PbTe/5 wt% graphene samples reached maximum *ZT* values of 0.7 at 670 K, which is approximately a six-fold increase compared to that of pristine PbTe prepared in the same manner.

Carbon nanotubes (CNT) also have been extensively employed in TE materials for reducing κ and enhancing *ZT*. Recently, Kim *et al* implanted CNT in Bi_2Te_3 powders by a novel chemical route, which led to a homogeneous dispersion of CNT in the Bi_2Te_3 matrix. The CNT reduced κ by promoting phonon-scattering at the Bi_2Te_3 interface, significantly increasing the *ZT* to 0.85 at 473 K.[352] In addition, Yeo *et al* obtained a high *ZT* value of 1.47 at 348 K for a $(Bi_{0.2}Sb_{0.8})_2Te_3$ nanocomposite with 0.12 wt% multiwall carbon nanotubes (MWCNTs) via enhanced

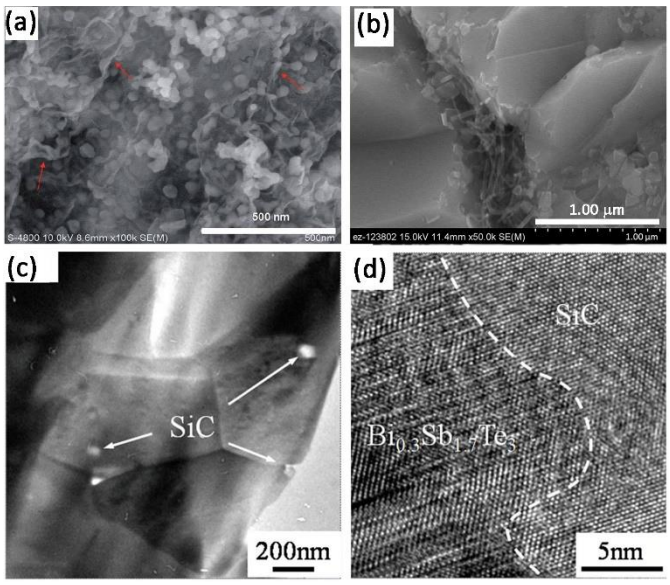

Figure 15. (a) The SEM image of PbTe-5 wt% graphene powders. The red arrows indicate the wrinkles of graphene. Reproduced with permission from ref[351]. Copyright 2013, The Royal Society of Chemistry. (b) The fracture surface shows the CNT distributed at $Bi_{0.4}Sb_{1.6}Te_3$ grain boundaries. Reproduced with permission from ref[324]. Copyright 2013, The American Institute of Physics. TEM images show (c) the SiC nanodispersion in $Bi_{0.3}Sb_{1.7}Te_3$ matrix, and (d) the interface between $Bi_{0.3}Sb_{1.7}Te_3$ matrix and SiC nanoparticles. Reproduced with permission from ref[332]. Copyright 2013, Wiley-VCH.

phonon scattering at the MWCNT/matrix interfaces and grain boundaries.[353] Similarly, Ren *et al.* incorporated MWCNTs into polycrystalline $Bi_{0.4}Sb_{1.6}Te_3$ through powder processing (**Figure 15b**). Interestingly, the results indicate the MWCNTs not only reduced κ but also increased the flexural strength of the materials.[324] For the intermediate-temperature thermoelectric PbTe, work by Khasimsaheb *et al.* indicate a 0.05% CNT distribution in a PbTe matrix significantly enhances σ and *S* above 450 K. They suggest CNTs introduce potential barriers and act as low energy filters, leading to enhanced Seebeck coefficient and maintain good mobility for high energy electrons, resulting in increased σ, we emphasize that this is however speculation at this point that needs additional experimental support. At the same time, the additional interfaces and enhanced phonon scattering facilitate ultralow κ of 0.32 W m^{-1} K^{-1} at 525 K for 0.05% CNT.[354]

Single crystalline SnSe shows a record high *ZT* of 2.6 at 923K, attracting considerable attention and intense study in recent years.[355] However, the layered structure results in poor mechanical properties and limits its wider applicability. As such, increasing attention is being directed at polycrystalline forms. Chu *et al* found Na-doped polycrystalline SnSe/CNTs composites not only maintain high carrier concentrations of approximately 4×10^{19} cm^{-3} and high σ at room temperature, but also reduced κ. As a result, a high *ZT* of ~0.96 at 773 K was obtained for polycrystalline SnSe sample with the addition of 0.25 vol% CNTs. More importantly, the composites demonstrated superior mechanical properties and thus may be more suitable for device fabrication and practical applications. Moreover, the Vickers hardness and flexural strength of the Na-doped polycrystalline SnSe/CNTs (1.0 vol% CNTs) composites

were enhanced by 59.8% and 47.9% respectively when compared to the CNTs-free sample. This study confirms that CNTs can improve TE and mechanical properties of the Na-doped SnSe polycrystalline materials.[327]

Fullerene (C_{60}) is a stable nonpolar molecule with high elastic modulus. In Cu_2SnSe_3, C_{60} and C_{60}-decorated grain boundaries were found to be effective phonon scattering sites that decreased κ_L. On the other hand, because the charge carrier wavelengths are larger than the size of a fullerene molecule, scattering of electrons or holes is comparatively negligible.[356] The effect of C_{60} in $Bi_{2-x}Sb_xTe_3$ alloys has also been extensively studied,[357-362] with results showing that fullerene molecules act as phonon blocking sites, reducing κ_L, and enhancing the TE performance. In addition, C_{60} also can efficiently reduce the κ_L of other TE systems including skutterudites[363, 364] and Cu-/Ag-based chalcogenides.[356, 365]

Because of its high thermal stability and elastic modulus, silicon carbide (SiC) is a favorable additive in composite materials. Dispersion of ultra-fine SiC nanoparticles into a host matrix has been found to be an effective strategy for reducing κ.[366]. For example, a high *ZT* of 1.54 at 723 K was obtained for $AgPb_{20}SbTe_{20}$ with 1% SiC via reduction of κ due to the mismatched interfaces between the dispersed SiC nanoparticles and $AgPb_{20}SbTe_{20}$ matrix.[367] Bathula *et al.* reported a high *ZT* of ~1.7 at 1173 K for SiGe/SiC nanocomposites via a significant reduction in κ_L. This *ZT* value is about twice than that of pristine bulk SiGe. The dispersion with SiC nanoparticles led to a high density of nanoscale interfaces, mass fluctuations and lattice scale modulations, resulting in extensive scattering of phonons.[366]
In addition to enhancing the TE performance, SiC doping can also improve the mechanical properties.[368-371] Yin *et al.* found the flexural strength, compressive strength, fracture toughness, and Vickers hardness of $Mg_2Si_{1-x}Sn_x$/SiC nano-composites were all significantly improved due to pinning effects, fiber pull-out mechanisms, and fiber bridging stemming from the nano-SiC additives. Moreover, the fracture toughness of $Mg_2Si_{1-x}Sn_x$ was enhanced by ~50% after addition of 0.8 at% of SiC nano-powders or nano-wires into the matrix. At the same time, the $Mg_2Si_{1-x}Sn_x$/SiC composite maintained excellent TE performance with maximum *ZT* of 1.20 at 750 K.[372] Interestingly, Li *et al.* reported mixing a small volume (0.4 vol%, **Figure 15c**) of SiC nanoparticles into the BiSbTe matrix can effectively enhance the TE performance with a high *ZT* of 1.33 at 373 K. It was indicated that SiC nanoparticles, which possess coherent interfaces with the matrix (**Figure 15d**), can increase both *S* and σ. Furthermore, the dispersion of SiC nanoparticles can significantly reduce κ_L of BiSbTe matrix by enhancing phonon scattering (**Figure 15e**) and endowing the BiSbTe alloys with improved mechanical properties.[373]

3.4.3 Porous structures. In general, most researchers prefer to synthesize fully dense (or as close as possible) bulk TE materials to achieve good electrical transport performance and mechanical properties as well as ensure reliable and consistent measurement of the material properties. Since the densities of bulk materials usually exceeds 95% of the theoretical values, the influence of porosity on TE performance is seldom considered. Porous structures nevertheless effectively scatter low-frequency phonons and reduce the κ_L of TE bulk materials. However, pores may also reduce μ_H, resulting in degradation of σ. Therefore, it is important to control the size and distribution of pores in order to favorably control the ratio μ_H/κ_L and enhance the *ZT* values of the corresponding porous TE materials.[374]

Pores can be introduced by tuning the synthesis and processing parameters, including the composition, morphology, and size of starting materials,[375-377] as well as adoption of various processing techniques.[36, 378-381] For instance, high-temperature consolidation processes inevitably lead to sublimation of the constituent Sb and Zn in $YbZn_2Sb_2$ compounds, thus generating *in-situ* nanopores with a random size distribution of 50-200 nm.[382] The samples with nanopore incorporation were found to have increased carrier mobility up to 191.3 $cm^2V^{-1}s^{-1}$, about 40% increase over that of dense bulk materials. The significant increase in the carrier mobility was suggested to arise from the nanopore-induced carrier drag effect however further experimental support will be needed to better understand this issue. Moreover, in comparison to fully densified counterparts, nanoporous samples present 16% decreases in κ_L at room temperature, which is due to the additional phonon scattering by randomly arranged nanopores. Ascribed to decreased κ_L, the nanoporous samples sintered at 998 K demonstrate 46% enhancement in the maximum *ZT* value

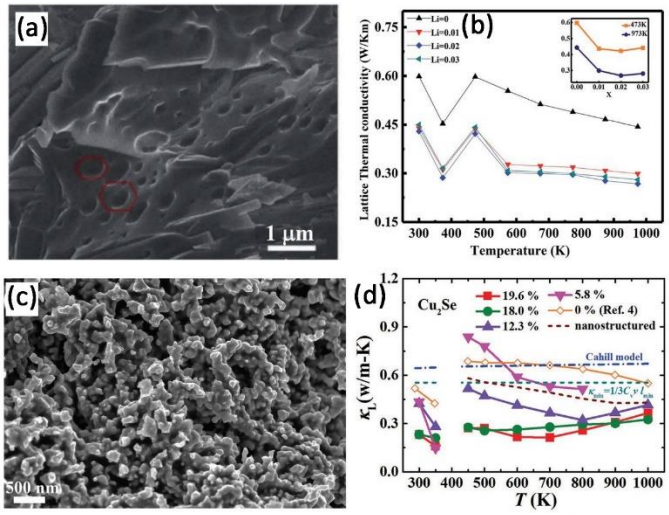

Figure 16. (a) The fracture surface of the $Cu_{1.98}Li_{0.02}Se$ bulk sample. Many nanopores can be found at grain boundaries. (b) The temperature-dependent lattice thermal conductivity of $Cu_{2-x}Li_xSe$ (x=0-0.03) samples. The inset shows the lattice thermal conductivity as a function of Li content at 473 K and 973 K, respectively. Reproduced with permission from ref[380]. Copyright 2018, The Royal Society of Chemistry. (c) Cu_2Se porous bulk materials prepared at 323 K (corresponding to 19.6% porosity). (d) Temperature dependence of lattice thermal conductivity (κ_L) for Cu_2Se porous bulk materials. The calculated minimum thermal conductivity (κ_{min}) was plotted as comparison. Reproduced with permission from ref[383]. Copyright 2017, Wiley-VCH.

compared to their highly densified counterparts. The improvement mainly stems from the enhanced scattering of low-frequency phonons in nanoporous $YbZn_2Sb_2$.

Hu *et al.* reported a maximum *ZT* of 2.14 at 973 K for $Cu_{1.98}Li_{0.02}Se$ prepared with *in-situ* nanopores.[380] The formation

of nanopores (**Figure 16a**) in Li-doped Cu_2Se was proposed to be related to Li substitution, which could reduce the melting point of $Cu_{2-x}Li_xSe$. This leads to the dissimilar shrinkage rates of liquid phase and solid phase, producing nanopores. Li-doped Cu_2Se exhibits a 25% decrease in κ_L (**Figure 16b**) as compared to pristine samples. In addition to incorporating nanoporous architectures into single-phase materials, this strategy has also been successfully applied in TE composites.[377, 381]

Recently, Wu *et al.* prepared nanoporous PbSe/SiO_2 composites by using mechanical alloying and subsequent wet-milling followed by rapid sintering.[381] The authors speculated that the porous structures are closely related to the hydrophilic behavior and abundant surfaces of the exotic SiO_2 nanoparticles. In the wet-milling process, the hydroxyl compounds are adsorbed onto SiO_2 nanoparticles and evaporate during the sintering process, leaving behind nanopores at the grain boundaries. Due to the additional phonon scattering at the interfaces, PbSe-0.7 vol% SiO_2 composites show a maximum *ZT* of 1.15 at 823 K.

Despite the promise of nanopores to reduce κ_L while maintaining μ_H, it remains a challenge to effectively control the pore size and porosity in bulk TE materials. Recently, Zhao *et al.* utilized a simple solid-state explosive reaction to prepare Cu_2Se pellets with well controlled pore sizes and distributions.[383] The homogeneously mixed raw elements were loaded into a graphite mold and subjected to spark plasma sintering. By interrupting the sintering process at different temperatures, the obtained pellet samples showed various porosities (5.8-19.6%) and pore sizes ranging from 20-50 nm to hundreds of nanometers. This led to the lowest κ_L of 0.22 W m^{-1} K^{-1} reported among low-density Cu_2Se samples (with 19.6% porosity, **Figure 16c**), which is lower than the theoretical value for fully dense Cu_2Se based on the Cahill model, **Figure 16d**. A peak *ZT* value of 1.9 at 973 K was reached for the Cu_2Se sample with a moderate porosity of 12.3%. This study provided a time- and cost-efficient way to synthesize a high-performance bulk TE material with controllable porosity.

Moreover, upon combination with various phonon scattering centers including point defects, dislocations, and grain boundaries, high porosity (~23%) samples of n-type $Bi_2Te_{2.5}Se_{0.5}$ reached ultralow κ_L of 0.14 W m^{-1} K^{-1} at 513 K.[376] This resulted in a peak *ZT* of 1.18 at 463 K, which is comparable to that of state-of-the-art $Bi_2Te_{3-x}Se_x$ materials. The hollow $Bi_2Te_{2.5}Se_{0.5}$ nanostructures were first synthesized by a self-templating method before being employed as starting materials for the sintering process. The nanoshells were crushed and merged into large grains while sintering at 623-673 K, leaving a high-density of pores at grain boundaries (**Figure 17a**). The theoretical modeling of temperature dependent κ_L is presented in **Figure 17b**, demonstrating an additional drop in κ_L with pore incorporation.

Likewise, based on the collective effects of porosity, grain boundaries, pore surfaces/junctions, and dislocations, Pan *et al.* realized a nearly 60% decrease in κ_L of melt-centrifuged $(Bi,Sb)_2Te_3$ compared to a zone-melted ingot.[374] During the centrifugation process, excess Te was forced out from the melt, leaving porous structures in the bulk $(Bi,Sb)_2Te_3$. This enhanced the scattering of low-frequency phonons at pore interfaces. Effective medium theory (EMT) can be used to estimate the

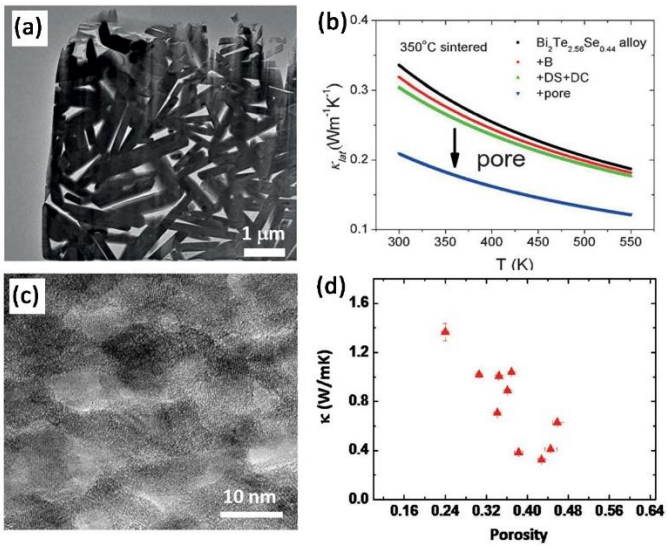

Figure 17. (a) TEM image of a porous $Bi_{2.02}Te_{2.56}Se_{0.44}$ nanocomposite sintered at 400 °C; (b) Theoretical modelling of the temperature dependent κ_L for the 350 °C-sintered BiTeSe nanocomposite. Here, B, DS, and DC denote grain boundaries, dislocation strain, and dislocation core, respectively. Reproduced with permission from ref[376]. Copyright 2017, Wiley-VCH. (c) TEM image of porous silicon nanowire; (d) Thermal conductivity as a function of porosity for ten different porous silicon nanowires. Reproduced with permission from ref [379]. Copyright 2017, Wiley-VCH.

effect of porosity on TE performance.[148, 384, 385] Furthermore, the simultaneous management of nanopores, nanoprecipitates and point defects in Cd-doped $SnTe_{1-x}Se_x$ led to a peak *ZT* of over 1.5 at 900 K.[386]

Introduction of porosity has also been implemented in low dimensional materials to either reduce κ_L or increase the area of active sites for catalytic applications.[36, 379, 387] For example, single-crystalline, porous Si nanowires (43% porosity) exhibit an ultralow κ of 0.33 W m^{-1} K^{-1} at room temperature, approaching the amorphous limit (**Figure 17c-d**).[379] Ju *et al.* employed Li-intercalation and liquid exfoliation to prepare $SnSe_{1-x}S_x$ nanosheets, which were then subjected to hydrothermal reaction in tartaric acid, to achieve porous structures.[387] Ascribed to the sulfur substitution and high porosity, $SnSe_{0.8}S_{0.2}$ nanosheets demonstrated a low κ of 0.4 W m^{-1}K^{-1} at 503 K, close to the theoretical limit κ_{min}.

The above findings mainly discuss facile strategies to design porous TE bulk materials with significantly reduced κ_L and ideally almost unaffected μ_H. They are challenging the widely-accepted viewpoint that fully dense bulk materials are desired and that porosity generally leads to negligible gain in *ZT* values. Therefore, these studies pave the way for developing bulk TE materials with well-controlled pore sizes and distributions to achieve improved *ZT* values. Despite the lower mechanical strengths of these porous materials compared to their highly densified counterparts,[383] they may exhibit higher crack-resistances and longer service lifetimes.[388]

3.4.4 Cellular structures. Cellular nanostructures are thin layers of a secondary phase that encapsulate or form "shells" around the grains of the primary thermoelectric phase. These

microstructures can significantly impede phonon transport, even in materials with already intrinsically low thermal conductivity and will intuitively also impact charge transport. Despite a number of experimental and theoretical works suggesting cellular structures as a dramatic means of limiting

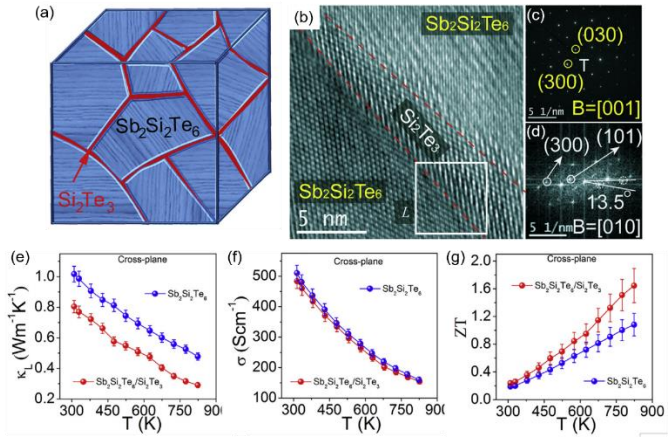

Figure 18. (a) Illustration of the cellular microstructure of $Sb_2Si_2Te_6$-Si_2Te_3 featuring a thin Sb_2Te_3 layer surrounding the bulk $Sb_2Si_2Te_6$ grains. (b) A high-resolution TEM image of the grain boundary region. (c) and (d) are respectively selected area electron diffraction images and fast-Fourier transformed images obtained from the TEM data and confirming the bulk $Sb_2Si_2Te_6$ and GB Si_2Te_3 phases. (e) Temperature-dependent lattice thermal conductivities, (f) electrical conductivities, and (g) *ZT*s of both pure Sb_2Si_2Te and $Sb_2Si_2Te_6$-Si_2Te_3. Reproduced with permission from ref[276]. Copyright 2020, Cell Press.

heat transport, there are relatively few good examples successfully employed in thermoelectric materials. This is because the cellular microstructures are normally grown around nanoparticles with wet chemical techniques, and these approaches are challenging to scale up and reliably utilize in bulk thermoelectric materials.

Recently, Luo *et al.* demonstrated the successful preparation of bulk $Sb_2Si_2Te_6$ with thin layers of Si_2Te_3 surrounding the grains (**Figure 18a**).[276] This was accomplished by first synthesizing polycrystalline $Sb_2Si_2Te_6$ by ball milling followed by SPS sintering with 10 weight percent excess Te. During the sintering process, a small amount of $Sb_2Si_2Te_6$ decomposes into Sb_2Te_3 and Si_2Te_3, and most of the Sb_2Te_3 is squeezed out with the excess liquid Te. As confirmed by TEM microscopy (**Figure 18b-d**), the post-synthetic reaction during compaction leaves a thin cellular structure of Si_2Te_3 along the grain boundaries. As shown in **Figure 18e**, the resulting $Sb_2Si_2Te_6$-Si_2Te_3 composites exhibit significantly suppressed lattice thermal conductivity compared to the single-phase $Sb_2Si_2Te_6$, which is attributed to strengthened phonon scattering by the Si_2Te_3 interfaces at the boundaries as well as the dense intragranular dislocations induced by high Sb vacancies. Surprisingly, the electrical conductivities of the $Sb_2Si_2Te_6$-Si_2Te_3 samples are nearly unchanged (**Figure 18f**). The authors address this result by using photoemission spectroscopy to demonstrate good valence-band alignment between the bulk $Sb_2Si_2Te_6$ and Si_2Te_3 layer, which allows charge to flow across the interfaces with minimal scattering. The close band alignment is confirmed by photoemission spectroscopy. Ultimately, while $Sb_2Si_2Te_6$ already has intrinsically promising *ZT* ~ 1, the cellular structured $Sb_2Si_2Te_6$-Si_2Te_3 achieves outstanding figures of merit approaching 1.65 at 823 K (**Figure 18g**). This study therefore introduces a new in-situ synthetic route to achieve cellular microstructures in bulk thermoelectric materials. Provided the technique is generalizable, integrating these nanoscale futures may represent a novel route to significantly improving material performance.

3.5 Multiscale defects

To sum up, defects with different dimensions have different impacts on the scattering of charge carriers and heat-carrying phonons. Considering that defects with multiscale dimensions can scatter phonons with various mean free paths, it is therefore important to introduce various defects in TE materials to scatter a wide spectrum of phonons for achieving *ZT* enhancement.[389] Based on the Debye-Callaway model, theoretical κ_L of TE materials can be expressed as,[166]

$$\kappa_L = \frac{k_B}{2\pi^2 v}\left(\frac{k_B T}{\hbar}\right)^3 \int_0^{\theta_D/T} \frac{x^4 e^x}{\tau_C^{-1}(e^x-1)^2} dx$$

where $x = \hbar\omega/k_B T$ is dimensionless, ω is the phonon frequency, $\hbar$ is the reduced Planck constant, v is the average sound velocity, θ_D is the Debye temperature, τ_C is the integration of relaxation times for various phonon scattering induced by phonon-phonon interaction (Umklapp process and normal process scattering denoted as τ_U and τ_N, respectively) and phonon-defects interaction, including point defect scattering (τ_{PD}), grain/phase boundary scattering (τ_B), dislocation core scattering (τ_{DC}), dislocation strain scattering (τ_{DS}) and stacking faults scattering ($\tau_{SF}{}^{-1}$) that are calculated by,[163]

$$\tau_C{}^{-1} = \sum_i \tau_i{}^{-1} = \tau_U{}^{-1} + \tau_N{}^{-1} + \tau_{PD}{}^{-1} + \tau_{DC}{}^{-1} + \tau_{DS}{}^{-1} + \tau_B{}^{-1} + \tau_{SF}{}^{-1} \ldots$$

where τ_i refers to the relaxation time for each phonon scattering mechanism *i*. The relaxation time for Umklapp phonon-phonon scattering (τ_U) can be calculated by,[390 391]

$$\tau_U{}^{-1} = A_N \frac{2}{(6\pi^2)^{1/3}} \frac{k_B \bar{V}^{1/3} \gamma^2 \omega^2 T}{\bar{M} v^3}$$

where A_N is the dimensionless factor estimated to include the contribution of normal phonon-phonon scattering (τ_N), γ is the Grüneisen parameter, $\bar{V}$ and $\bar{M}$ are the average atomic volume and average atomici mass of the TE material, respectively. In terms of point defect scattering, Klemens first calculated the phonon relaxation time by taking the mass fluctuation into account.[163] Abeles then incorporated strain field modification and described the relaxation time τ_{PD} for point-defect scattering of phonons as,[167]

$$\tau_{PD}{}^{-1} = \frac{V\omega^4}{4\pi v^3}\Gamma$$

and

$$\Gamma = \sum_i f_i\left(1 - \frac{m_i}{\bar{m}}\right)^2 + \sum_i f_i\left(1 - \frac{r_i}{\bar{r}}\right)^2$$

where *V* is the volume per atom, Γ is the scattering parameter, m_i is the mass of an atom, $\bar{m}$ is the average mass of all atoms, r_i is the radius of an atom, $\bar{r}$ is the average radius of all atoms, f_i corresponds to the fraction of atoms with mass $m_i$and radius r_i . For grain boundaries, the scattering rate of phonons is determined by,[392, 393]

$$\tau_B{}^{-1} = v/L$$

where L denotes the grain size for grain boundary. Grain boundary scattering exhibits frequency independence of phonon scattering. The relaxation time of phonon scattering by stacking faults can be estimated by,[394]

$$\tau_{SF}{}^{-1} = \frac{4}{3}\frac{1}{G_3 v}\frac{a}{18}\gamma^2\omega^2$$

where a is the lattice constant, and G_3 is the number of layers in a crystal containing one stacking fault. In the case of phonon-dislocation scattering, the influences of dislocation cores (τ_{DC}) and surrounding dislocation strains (τ_{Ds}) can be estimated via,

$$\tau_{DC}{}^{-1} \propto N_D \frac{r^4}{v^2}\omega^3$$

and

$$\tau_{DS}{}^{-1} \propto N_D \frac{\gamma^2 B_D^2 \omega}{2\pi}$$

where N_D is the dislocation density, r is the radius of dislocation core, B_D is the Burgers vector of the dislocation.

Clearly, these various types of defect-phonon scattering exhibit different temperature and frequency dependent relaxation times. In general, point defects target the scattering of high-frequency phonons ($\tau_{PD}{}^{-1} \propto \omega^4$) at intermediate temperatures (50-100 K) while grain boundaries aim to scatter low-frequency phonons at low temperatures (20-40 K), and Umklapp phonon-phonon scattering dominates at high temperatures (close to θ_D =300 K). Further incorporation of dislocations and stacking faults can scatter mid-frequency phonons, achieving full-spectrum phonon scattering and thus significant reduction of κL in TE materials.[162, 279]

4. Defect engineering to enhance mechanical performance of TE materials

The various defects discussed above are primarily beneficial to the electrical or/and thermal transport properties of TE materials, which in turn boosts the maximum ZT values.[395] However, most state-of-the-art TE pellets are brittle with poor mechanical properties and machinability, which restricts from the development of TE module assembly and long-term operation under harsh conditions, such as thermal cycling and high temperature exposure.[396] To this end, improving the mechanical properties is important and must be addressed for TEs to achieve widespread use. As such, researchers are increasingly focused on improving the mechanical properties of TE materials by microstructure manipulation and defect engineering to dissipate the crack propagation energy. The former strategy is mainly realized by reducing the distribution of grain sizes, which depends on the development of non-equilibrium process such as mechanical alloying, hot deformation, and melt spinning. The incorporation of defects, such as dislocation, micropores, nanoprecipitates, and twinning can further improve the mechanical responses. In this section, we discuss the recent progress in the strengthening of mechanical properties by defect engineering.

In addition to enhancing phonon scattering, typical 3D defects such as nanoinclusions and micropores can introduce crack toughening mechanisms, including crack deflection, crack blunting, crack pinning and crack branching, and thus increase the mechanical toughness. In particular, the introduction of micropores in thermoelectric materials can promote intrinsic crack toughening via crack blunting, i.e. a growing crack tip impinges on a pore and stops propagating.[46, 47, 397] As discussed in prior sections, melt-spinning or mechanical alloying combined with rapid sintering is frequently employed as a non-equilibrium technique to prepare high-performance TE materials, such as Bi_2Te_3-based alloys, skutterudites, and Zn_4Sb_3. Some of these nanostructured TE materials demonstrate concomitant increases in the mechanical properties as manifested by significant enhancement of hardness, compressive strength, fracture toughness, and compressive fatigue resistance.[27, 398] Recently, simultaneous improvement of the TE and mechanical properties were achieved in p-type $Bi_{0.5}Sb_{1.5}Te_3$ fabricated by melt-spinning and plasma activated sintering (MS-PAS).[27] The MS-PAS-induced hierarchical structures, including in-situ formed nanoprecipitates and matrix crystals with sizes spanning from sub-microns to tens of microns, serve as crack blocking/deflecting centers (**Figure 19c-d**) and lead to significant enhancement of mechanical toughness. In comparison to zone-melted ingots, MS-PAS samples exhibit ~30% improvement of fracture toughness, as well as a six- to eight-fold enhancement in their flexural and compressive strengths, respectively, as presented in **Figure 19a-b**.

Moreover, mechanical alloying has been employed to disperse SiC,[329, 332, 399] TiN,[335] carbon nanotubes,[324] carbon fibers,[400] B_4C,[401] or conductive glass inclusions[402] in state-of-the-art TE materials to improve their mechanical properties. The addition of a small portion of SiC nanoparticles (1-2 vol%) can enhance the fracture toughness of Mg_2Si through the crack deflection mechanism.[399] A significant increase of flexural strength was observed in $Bi_{0.4}Sb_{1.6}Te_3$ with 0.5 wt% carbon nanotubes,[324] which is ascribed to the pull-out of carbon

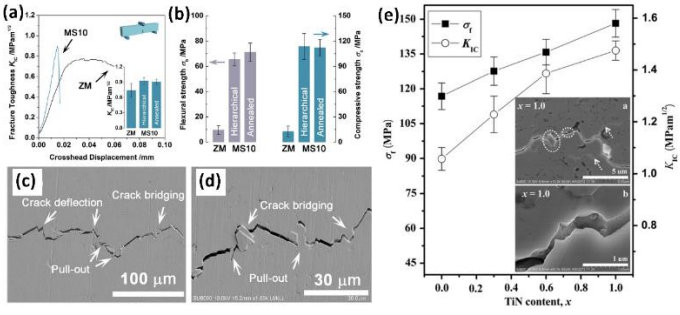

Figure 19. (a) Fracture toughness K_{IC} *vs.* displacement curves for ZM and MS10 samples. Here, MS10 refers to the sample prepared with the optimum linear speed of 10 m/s. The inset shows the K_{IC} values for ZM, MS10, and annealed MS10 samples; (b) Flexural and compressive strengths of ZM, MS10 and annealed MS10 specimens; (c) and (d) Crack propagation images of MS10 samples after the K_{IC} test, showing crack deflecting, pull-out, and crack bridging. Reproduced with permission from ref[27]. Copyright 2015, Wiley-VCH. (e) Flexural strength and fracture toughness of $CoSb_{2.875}Te_{0.125}$/TiN composites with various TiN content. The inset shows crack deflection, crack bridging and crack branching in $CoSb_{2.875}Te_{0.125}$/1.0 vol% TiN composites. Reproduced with permission from ref[335]. Copyright 2012, Elsevier.

nanotubes from the matrix. In addition, dispersing nano-TiN in $CoSb_{2.875}Te_{0.125}$ simultaneously enhanced the flexural strength and fracture toughness.[335] The increased crack resistance is mainly ascribed to crack branching, crack deflection, and crack bridging mechanisms (**Figure 19e**).

PbTe jointly alloyed with Ca and Ba was also recently shown to have improved mechanical properties. P-type PbTe–SrTe are among the very finest TE materials, with outstanding *ZT*s up to 2.5 at 923 K.[389, 395] Unfortunately however, the optimal doping and alloying compositions yield samples extremely prone to cracking and breakage rendering device fabrication nearly impossible. Sarkar *et al*. demonstrated alloying PbTe with Ca and Ba in the place of Sr gives samples with dramatically improved mechanical toughness while retaining the high *ZT*s of 2.2 at 923 K.[403] This could be ascribed to the lattice and precipitation hardening effects caused by low concentration metal telluride precipitates (1 mol % $Ba_{0.5}Ca_{0.5}Te$ in $Pb_{0.97}Na_{0.03}Te$) and improved grain refinement (based on the Hall-Petch relation). Moreover, these semicoherent nanoprecipitates could serve as barriers to impede dislocation motion across the GBs. That said, the ultimate mechanism for the hardening remains and open question still in need of resolution. It is furthermore an interesting question whether the dual alloying approach can achieve similar hardening in other thermoelectric semiconductors. In any case, this work directly shows the choice of dopant/alloying element can have a significant impact on the mechanical properties, in addition to the charge and thermal transport behavior. Considering the importance of sample toughness for practical TE applications, the complete impact of dopants, on both transport and mechanical behavior, should be taken into account. In our opinion far more work is needed to be done in this area you know the to answer some of these questions and further understand the weak mechanical properties of lead chalcogenides and how they can be improved to a level that is suitable for widespread thermoelectric module generators.

5. Concluding discussion and future

Defect engineering underpins all means of optimizing the performance of TE materials. Substantial attention has been paid to introducing defects of varied dimensionality and length scale into TE materials to synergistically improve the electrical, thermal and mechanical properties. Each type of defect imparts unique affects on the thermoelectric and mechanical properties in ways that can be both beneficial or costly. the Because defects have competing effects, the limitations and drawbacks of each class must be taken into consideration to ensure the best performance.

In general, point defects are useful for optimizing the charge carrier concentration and scattering of high-frequency phonons. But point defects are sensitive to the synthesis and service conditions, making it difficult to precisely manipulate different point defects and control their concentrations in TE materials. For instance, the high density of native vacancies normally results in overdoping in SnTe, while cation vacancies can act as acceptor states and prevent proper doping in n-type PbTe and Mg_3Sb_2. Similarly, the concentration of antisite defects (Sb_{Te}' or Bi_{Te}') in $(Bi,Sb)_2Te_3$ compounds can be adjusted by changing the initial Bi/Sb ratio. While the subsequent thermal annealing process can result in the annihilation of these antisite defects. In the case that various point defects are present in a certain TE material, the calculation of defect formation energies is useful for analysing which point defect dominates the intrinsic properties. This provides important guidelines for designing the best synthesis approach and for the further optimization of the thermoelectric properties.

By further incorporating 1D, 2D and/or 3D defects such as dislocations, grain boundaries and nanoprecipitates, one can induce broad-spectrum phonon scattering and dramatically reduce the lattice thermal conductivity. Careful attention should be paid to the manipulation of the dislocation density, which must be higher than 10^{12} cm^{-2} to realize the effective phonon scattering.[117] Moreover, while the success of grain boundary engineering lead to a widely accepted consensus that TE materials with small grains usually exhibit lower κ_L compared to those with large grains or single crystals, recent work reveals notable exceptions in Mg_3Sb_2 and SnSe,where electrically-resistive grain boundaries degrade the performance and also result in overestimation of κ_L. [272, 404] A useful rule of thumb for GB engineering is that more ionic materials (like Zintl antimonides) are more likely to have resistive GBs, while polarizable compounds (like PbTe or Bi_2Te_3) will benefit from small grains.

The incorporation of porous structures in TE materials can result in reduced machinability and weakened mechanical strength that causes problems for device manufacturing. In addition, the composition and size distribution of nanoinclusions should be carefully chosen and determined to minimize the mismatch of thermal expansion coefficients in between the nanoinclusions and matrix materials. Failure to do so can bring about the formation of voids and microcracks at grain boundaries which deteriorate TE and mechanical strength. To ensure good carrier mobility, close band alignment between matrix and precipitate phases is furthermore desirable. Considering these defects can suppress the carrier mobility and sometimes may only have a small impact on the thermal conductivity, it is critical to properly configure and control the types and concentrations of defects in TE materials so that a net increase of *ZT* and enhanced mechanical properties is realized. With the rapid development of defect engineering in TE materials, several concerns are particularly pertinent, as listed below.

(1) Defect stability: In practical applications, TE materials and devices often encounter complex service conditions, including exposure to high operating temperatures for extended periods of time, thermal cycling, and vibrational forces, all of which may cause defects to evolve and/or interact. Such operating conditions may change the matrix composition or the dominant scattering mechanism of phonons and charge carriers, resulting in unstable TE performance. For example, when Bi_2Te_3-based polycrystallites are subject to prolonged heat treatment at 573 K, the matrix becomes porous and bloated due to the inevitable sublimation of tellurium.[405] Upon extended thermal exposure,

$Bi_{0.5}Sb_{1.5}Te_3$ alloys present degraded TE performance which is ascribed to the substantial decrease of the carrier concentration and porous structures. Cyclic stresses generated from thermal cycling or vibrational stress in service also have a great impact on the defect stability. However, this topic has seldom been investigated in TE materials. Specifically, the stress field affects the motion of dislocations. Dislocations can evolve under cyclic stress and get pinned by grain boundaries or precipitates, leading to the increase of dislocation density and corresponding mechanical toughness. Therefore, the continued study of defect stability in TE materials is critical to developing practical modules suitable for widespread and long-term applications.

(2) Characterization of defects. Defects play important roles in determining the TE transport properties and mechanical performance. Therefore, establishing the relationship between composition, microstructure, and performance of defects in each materials is a central problem in the field. Unfortunately, it is generally difficult to carry-out direct real-time observation and in-situ characterization of defects as they are in the non-equilibrium states and prone to movement or transformation under different conditions. For example, when subject to thermal annealing treatment, the intentionally incorporated vacancies in lead chalcogenides can diffuse to form vacancy clusters which then collapse into dislocations. In recent years, advanced instruments and techniques have been developed and applied to characterize the defects in TE (and other) materials.[406] Large amounts of Sn vacancies and Se interstitials have been directly observed in SnSe single crystals using aberration corrected scanning transmission electron microscopy.[407] The presence of these off-stoichiometric point defects further accounts for the intrinsically ultralow lattice thermal conductivity of SnSe single crystals. Moreover, in-situ TEM or SEM have realized the in-situ observation of defects evolution under high temperature or mechanical forces.

(3) Defect-interface interaction: as promising TE performance has been found in nanostructured materials with a large density of interfaces, it is important to understand the interactions between defects and interfaces, which influence concentrations of different defects and therefore TE and mechanical properties.[408] In general, interfaces can serve as sinks for point defects via absorption and annihilation, barriers for dislocations, as well as the storage sites for defects.

Conflicts of interest

There are no conflicts to declare.

Acknowledgements

TE materials research at NTU is supported by Agency for Science, Technology and Research (A*STAR), Industry Alignment Fund, Pharos ''Hybrid thermoelectric materials for ambient applications'' Program (Grant no.: 1527200019). TE materials research at Northwestern (TJS, YL, ZZL, and MGK) is supported by the U.S Department of Energy, Office of Science and Office of Basic Energy Sciences for funding under award number DE-SC0014520.

Notes and references

1. S. M. O'Shaughnessy, M. J. Deasy, J. V. Doyle and A. J. Robinson, *Energy for Sustainable Development*, 2014, **20**, 1-10.
2. J. Yang and F. R. Stabler, *J Electron Mater*, 2009, **38**, 1245-1251.
3. Y. D. Deng, Y. Zhang and C. Q. Su, *Journal of Electronic Materials*, 2015, **44**, 1491-1497.
4. L. Wang and A. Romagnoli, *2016 IEEE 2nd Annual Southern Power Electronics Conference (SPEC)*, 2016, 1-6.
5. W. He, G. Zhang, X. Zhang, J. Ji, G. Li and X. Zhao, *Applied Energy*, 2015, **143**, 1-25.
6. F. K. Shaikh and S. Zeadally, *Renewable and Sustainable Energy Reviews*, 2016, **55**, 1041-1054.
7. A. R. M. Siddique, S. Mahmud and B. Van Heyst, *Renewable and Sustainable Energy Reviews*, 2017, **73**, 730-744.
8. R. C. O'Brien, R. M. Ambrosi, N. P. Bannister, S. D. Howe and H. V. Atkinson, *J Nucl Mater*, 2008, **377**, 506-521.
9. J. He and T. M. Tritt, *Science*, 2017, **357**, 1369.
10. W. Liu, Q. Jie, H. S. Kim and Z. Ren, *Acta Mater.*, 2015, **87**, 357-376.
11. S. W. Angrist, *Direct energy conversion*, Allyn and Bacon, Inc.,Boston, 1976.
12. G. J. Snyder and E. S. Toberer, *Nat. Mater.*, 2008, **7**, 105-114.
13. M. Hong, Y. Wang, W. Liu, S. Matsumura, H. Wang, J. Zou and Z.-G. Chen, *Advanced Energy Materials*, 2018, **8**, 1801837.
14. Y. Pei, H. Wang and G. J. Snyder, *Adv Mater*, 2012, **24**, 6125-6135.
15. X. Su, P. Wei, H. Li, W. Liu, Y. Yan, P. Li, C. Su, C. Xie, W. Zhao, P. Zhai, Q. Zhang, X. Tang and C. Uher, *Adv. Mater.*, 2017, **29**, 1602013.
16. M. K. Jana and K. Biswas, *ACS Energy Letters*, 2018, **3**, 1315-1324.
17. Y. Liu, M. Zhou and J. He, *Scripta Mater*, 2016, **111**, 39-43.
18. Y. Pei, X. Shi, A. LaLonde, H. Wang, L. Chen and G. J. Snyder, *Nature*, 2011, **473**, 66-69.
19. W. Liu, X. Tan, K. Yin, H. Liu, X. Tang, J. Shi, Q. Zhang and C. Uher, *Phys. Rev. Lett.*, 2012, **108**, 166601.
20. G. Tan, W. G. Zeier, F. Shi, P. Wang, G. J. Snyder, V. P. Dravid and M. G. Kanatzidis, *Chemistry of Materials*, 2015, **27**, 7801-7811.
21. C. M. Jaworski, V. Kulbachinskii and J. P. Heremans, *Physical Review B*, 2009, **80**, 233201.
22. J. P. Heremans, V. Jovovic, E. S. Toberer, A. Saramat, K. Kurosaki, A. Charoenphakdee, S. Yamanaka and G. J. Snyder, *Science*, 2008, **321**, 554-557.
23. Q. Zhang, H. Wang, W. Liu, H. Wang, B. Yu, Q. Zhang, Z. Tian, G. Ni, S. Lee, K. Esfarjani, G. Chen and Z. Ren, *Energy & Environmental Science*, 2012, **5**, 5246-5251.
24. J. P. Heremans, B. Wiendlocha and A. M. Chamoire, *Energy & Environmental Science*, 2012, **5**, 5510-5530.
25. B. Poudel, Q. Hao, Y. Ma, Y. Lan, A. Minnich, B. Yu, X. Yan, D. Wang, A. Muto, D. Vashaee, X. Chen, J. Liu, M. S. Dresselhaus, G. Chen and Z. Ren, *Science*, 2008, **320**, 634.
26. H. J. Wu, L. D. Zhao, F. S. Zheng, D. Wu, Y. L. Pei, X. Tong, M.

G. Kanatzidis and J. Q. He, *Nat. Commun.*, 2014, **5**, 4515.

27. Y. Zheng, Q. Zhang, X. Su, H. Xie, S. Shu, T. Chen, G. Tan, Y. Yan, X. Tang, C. Uher and G. J. Snyder, *Adv. Energy Mater.*, 2015, **5**, 1401391.
28. X. Su, F. Fu, Y. Yan, G. Zheng, T. Liang, Q. Zhang, X. Cheng, D. Yang, H. Chi, X. Tang, Q. Zhang and C. Uher, *Nat. Commun.*, 2014, **5**, 4908.
29. L. Hu, Y. Zhang, H. Wu, Y. Liu, J. Li, J. He, W. Ao, F. Liu, J. Pennycook Stephen and X. Zeng, *Advanced Functional Materials*, 2018, **28**, 1803617.
30. D. Morelli, V. Jovovic and J. Heremans, *Phys. Rev. Lett.*, 2008, **101**, 035901.
31. H. Liu, X. Shi, F. Xu, L. Zhang, W. Zhang, L. Chen, Q. Li, C. Uher, T. Day and G. J. Snyder, *Nat. Mater.*, 2012, **11**, 422-425.
32. B. Li, H. Wang, Y. Kawakita, Q. Zhang, M. Feygenson, H. Yu, D. Wu, K. Ohara, T. Kikuchi and K. Shibata, *Nat Mater*, 2018, **17**, 226.
33. R. J. Tilley, *Defects in solids*, John Wiley & Sons, 2008.
34. P. Niu, M. Qiao, Y. Li, L. Huang and T. Zhai, *Nano Energy*, 2018, **44**, 73-81.
35. J. Hong, C. Jin, J. Yuan and Z. Zhang, *Advanced Materials*, 2017, **29**, 1606434.
36. K. N. Dinh, P. Zheng, Z. Dai, Y. Zhang, R. Dangol, Y. Zheng, B. Li, Y. Zong and Q. Yan, *Small*, 2018, **14**, 1703257.
37. H. Zhang and R. Lv, *Journal of Materiomics*, 2018, **4**, 95-107.
38. G. Parande, V. Manakari, S. D. S. Kopparthy and M. Gupta, *Adv Eng Mater*, 2017, **20**, 1700919.
39. H. L. Tuller and S. R. Bishop, *Annual Review of Materials Research*, 2011, **41**, 369-398.
40. I. T. Lu and M. Bernardi, *Scientific Reports*, 2017, **7**, 3403-3403.
41. W. Xu, C. Sun, K. Zhao, X. Cheng, S. Rawal, Y. Xu and Y. Wang, *Energy Storage Materials*, 2019, **16**, 527-534.
42. D.-Y. Son, S.-G. Kim, J.-Y. Seo, S.-H. Lee, H. Shin, D. Lee and N.-G. Park, *Journal of the American Chemical Society*, 2018, **140**, 1358-1364.
43. M. Kumar, A. Dubey, N. Adhikari, S. Venkatesan and Q. Qiao, *Energy & Environmental Science*, 2015, **8**, 3134-3159.
44. L. Hu, T. Zhu, X. Liu and X. Zhao, *Advanced Functional Materials*, 2014, **24**, 5211-5218.
45. Z. Chen, B. Ge, W. Li, S. Lin, J. Shen, Y. Chang, R. Hanus, G. J. Snyder and Y. Pei, *Nature Communications*, 2017, **8**, 13828.
46. J. B. Wachtman, W. R. Cannon and M. J. Matthewson, *Mechanical properties of ceramics*, John Wiley & Sons Inc, New York, 2009.
47. E. D. Case, in *Modules, Systems, and Applications in Thermoelectrics*, CRC Press, Boca Raton, FL, 2012, pp. 1-29.
48. A. Goyal, P. Gorai, S. Anand, E. S. Toberer, G. J. Snyder and V. Stevanović, *Chemistry of Materials*, 2020, **32**, 4467-4480.
49. K. Xia, P. Nan, S. Tan, Y. Wang, B. Ge, W. Zhang, S. Anand, X. Zhao, G. J. Snyder and T. Zhu, *Energy & Environmental Science*, 2019, **12**, 1568-1574.
50. L. Xi, S. Pan, X. Li, Y. Xu, J. Ni, X. Sun, J. Yang, J. Luo, J. Xi, W. Zhu, X. Li, D. Jiang, R. Dronskowski, X. Shi, G. J. Snyder and W. Zhang, *Journal of the American Chemical Society*, 2018, **140**, 10785-10793.
51. X. Li, Y. Sheng, L. Wu, S. Hu, J. Yang, D. J. Singh, J. Yang and W. Zhang, *npj Computational Materials*, 2020, **6**, 107.
52. B. R. Ortiz, P. Gorai, L. Krishna, R. Mow, A. Lopez, R. McKinney, V. Stevanović and E. S. Toberer, *Journal of Materials Chemistry A*, 2017, **5**, 4036-4046.
53. R. Gautier, X. Zhang, L. Hu, L. Yu, Y. Lin, T. O. L. Sunde, D. Chon, K. R. Poeppelmeier and A. Zunger, *Nature Chemistry*, 2015, **7**, 308-316.
54. P. Gorai, A. Ganose, A. Faghaninia, A. Jain and V. Stevanović, *Materials Horizons*, 2020, **7**, 1809-1818.
55. P. Gorai, A. Goyal, E. S. Toberer and V. Stevanović, *Journal of Materials Chemistry A*, 2019, **7**, 19385-19395.
56. A. Banik, S. Roychowdhury and K. Biswas, *Chemical Communications*, 2018, **54**, 6573-6590.
57. M. Hong, Z.-G. Chen and J. Zou, *Chin. Phys. B*, 2018, **27**, 048403.
58. M. Karunanithy, G. Prabhavathi, A. H. Beevi, B. Ibraheem, K. Kaviyarasu, S. Nivetha, N. Punithavelan, A. Ayeshamariam and M. Jayachandran, *Journal of Nanoscience and Nanotechnology*, 2018, **18**, 6680-6707.
59. S. Li, X. Li, Z. Ren and Q. Zhang, *Journal of Materials Chemistry A*, 2018, **6**, 2432-2448.
60. J. Zhai, T. Wang, H. Wang, W. Su, X. Wang, T. Chen and C. Wang, *Chinese Physics B*, 2018, **27**, 047306.
61. R. Moshwan, L. Yang, J. Zou and Z.-G. Chen, *Advanced Functional Materials*, 2017, **27**, 1703278.
62. W.-D. Liu, D.-Z. Wang, Q. Liu, W. Zhou, Z. Shao and Z.-G. Chen, *Advanced Energy Materials*, 2020, **10**, 2000367.
63. G. Dennler, R. Chmielowski, S. Jacob, F. Capet, P. Roussel, S. Zastrow, K. Nielsch, I. Opahle and G. K. H. Madsen, *Advanced Energy Materials*, 2014, **4**, 1301581.
64. C. Gayner, K. K. Kar and W. Kim, *Materials Today Energy*, 2018, **9**, 359-376.
65. V. Q. Nguyen, J. Kim and S. Cho, *Journal of the Korean Physical Society*, 2018, **72**, 841-857.
66. T.-R. Wei, Y. Qin, T. Deng, Q. Song, B. Jiang, R. Liu, P. Qiu, X. Shi and L. Chen, *Science China Materials*, 2018, **62**, 8-24.
67. T.-R. Wei, C.-F. Wu, F. Li and J.-F. Li, *Journal of Materiomics*, 2018, **4**, 304-320.
68. G. Han, Z. G. Chen, J. Drennan and J. Zou, *Small*, 2014, **10**, 2747-2765.
69. W.-D. Liu, L. Yang and Z.-G. Chen, *Nano Today*, 2020, **35**, 100938.
70. Z.-H. Ge, L.-D. Zhao, D. Wu, X. Liu, B.-P. Zhang, J.-F. Li and J. He, *Materials Today*, 2016, **19**, 227-239.
71. K. Koumoto, Y. Wang, R. Zhang, A. Kosuga and R. Funahashi, *Annual Review of Materials Research*, 2010, **40**, 363-394.
72. M. Mohammed, I. Sudin, A. M. Noor, S. Rajoo, M. Uday, N. H. Obayes and M. F. Omar, *International Journal of Engineering & Technology*, 2018, **7**, 27-30.
73. A. T. Burkov, *Physica Status Solidi A*, 2018, **215**, 1800105.
74. R. Santos, S. Aminorroaya Yamini and S. X. Dou, *Journal of Materials Chemistry A*, 2018, **6**, 3328-3341.
75. W. Liu, K. Yin, Q. Zhang, C. Uher and X. Tang, *Natl. Sci. Rev.*, 2017, **4**, 611-626.
76. X. Shi, X. Wang, W. Li and Y. Pei, *Small Methods*, 2018, **2**, 1800022.
77. J. Yu, K. Xia, X. Zhao and T. Zhu, *Journal of Physics D: Applied Physics*, 2018, **51**, 113001.
78. Z. Liu, J. Mao, J. Sui and Z. Ren, *Energy & Environmental Science*, 2018, **11**, 23-44.
79. W. Peng, S. Chanakian and A. Zevalkink, *Inorganic Chemistry Frontiers*, 2018, **5**, 1744-1759.
80. K. Suekuni and T. Takabatake, in *Materials Aspect of Thermoelectricity*, CRC Press, 2016, pp. 233-250.
81. Y. Chen, Y. Zhao and Z. Liang, *Energy & Environmental Science*, 2015, **8**, 401-422.

82. M. Bharti, A. Singh, S. Samanta and D. K. Aswal, *Progress in Materials Science*, 2018, **93**, 270-310.
83. Y. Du, J. Xu, B. Paul and P. Eklund, *Applied Materials Today*, 2018, **12**, 366-388.
84. H. Yao, Z. Fan, H. Cheng, X. Guan, C. Wang, K. Sun and J. Ouyang, *Macromolecular Rapid Communications*, 2018, **39**, 1700727.
85. Q. Zhang, Y. Sun, W. Xu and D. Zhu, *Advanced Materials*, 2014, **26**, 6829-6851.
86. Y. Zheng, H. Zeng, Q. Zhu and J. Xu, *Journal of Materials Chemistry C*, 2018, **6**, 8858-8873.
87. J. L. Blackburn, A. J. Ferguson, C. Cho and J. C. Grunlan, *Adv Mater*, 2018, **30**.
88. X. Wang, H. Wang and B. Liu, *Polymers*, 2018, **10**, 1196.
89. Y. Zhou and L. D. Zhao, *Adv Mater*, 2017, **29**.
90. M. Markov and M. Zebarjadi, *Nanosc Microsc Therm*, 2019, **23**, 117-127.
91. Y. Zhang, Y. Zheng, K. Rui, H. H. Hng, K. Hippalgaonkar, J. Xu, W. Sun, J. Zhu, Q. Yan and W. Huang, *Small*, 2017, **13**, 1700661.
92. J. Wu, Y. Chen, J. Wu and K. Hippalgaonkar, *Advanced Electronic Materials*, 2018, **4**, 1800248.
93. A. Azhar, C. Yixi, V. Venkata and V. Sreeram, *Nanotechnology*, 2017, **28**, 282001.
94. C. Chang and L.-D. Zhao, *Materials Today Physics*, 2018, **4**, 50-57.
95. J. Xin, Y. Tang, Y. Liu, X. Zhao, H. Pan and T. Zhu, *npj Quantum Materials*, 2018, **3**, 9.
96. Z. Chen, X. Zhang and Y. Pei, *Adv Mater*, 2018, **30**, 1705617.
97. S. Ortega, M. Ibáñez, Y. Liu, Y. Zhang, M. V. Kovalenko, D. Cadavid and A. Cabot, *Chemical Society Reviews*, 2017, **46**, 3510-3528.
98. K.-X. Chen, M.-S. Li, D.-C. Mo and S.-S. Lyu, *Frontiers in Energy*, 2018, **12**, 97-108.
99. L.-D. Zhao, V. P. Dravid and M. G. Kanatzidis, *Energy Environ. Sci.*, 2014, **7**, 251-268.
100. D. S. Patil, R. R. Arakerimath and P. V. Walke, *Renewable and Sustainable Energy Reviews*, 2018, **95**, 1-22.
101. M. Haras and T. Skotnicki, *Nano Energy*, 2018, **54**, 461-476.
102. W. Liu, J. Hu, S. Zhang, M. Deng, C.-G. Han and Y. Liu, *Materials Today Physics*, 2017, **1**, 50-60.
103. H. S. Kim, W. Liu and Z. Ren, *Energy & Environmental Science*, 2017, **10**, 69-85.
104. W. Liu, H. S. Kim, Q. Jie and Z. Ren, *Scripta Mater.*, 2016, **111**, 3-9.
105. X. Shi, L. Chen and C. Uher, *Int. Mater.Rev.*, 2016, **61**, 379-415.
106. X. Zhou, Y. Yan, X. Lu, H. Zhu, X. Han, G. Chen and Z. Ren, *Mater Today*, 2018, **21**, 974-988.
107. T. Zhu, Y. Liu, C. Fu, J. P. Heremans, J. G. Snyder and X. Zhao, *Adv Mater*, 2017, **29**, 1605884.
108. X.-L. Shi, J. Zou and Z.-G. Chen, *Chemical Reviews*, 2020, **120**, 7399-7515.
109. T.-R. Wei, M. Guan, J. Yu, T. Zhu, L. Chen and X. Shi, *Joule*, 2018, **2**, 2183-2188.
110. Z. Li, C. Xiao, H. Zhu and Y. Xie, *J Am Chem Soc*, 2016, **138**, 14810-14819.
111. C. Zhao, Z. Li, T. Fan, C. Xiao and Y. Xie, *Research*, 2020, **2020**, 9652749.
112. T. Zhu, L. Hu, X. Zhao and J. He, *Adv. Sci.* , 2016, **3**, 1600004.
113. T. Masayuki, A. Yuki and Y. Kazuki, *Nanotechnology*, 2016, **27**, 335703.
114. N. Xiao, X. Dong, L. Song, D. Liu, Y. Tay, S. Wu, L.-J. Li, Y. Zhao, T. Yu, H. Zhang, W. Huang, H. H. Hng, P. M. Ajayan and Q. Yan, *Acs Nano*, 2011, **5**, 2749-2755.
115. W. Zhao, S. Fan, N. Xiao, D. Liu, Y. Y. Tay, C. Yu, D. Sim, H. H. Hng, Q. Zhang, F. Boey, J. Ma, X. Zhao, H. Zhang and Q. Yan, *Energy & Environmental Science*, 2012, **5**, 5364-5369.
116. S. Augustine, S. Ampili, Y. Seong-Ho, K. Kang Jeung and E. Mathai, *Journal of Physics: Condensed Matter*, 2005, **17**, 2873.
117. P. G. Klemens, *Proceedings of the Physical Society. Section A*, 1955, **68**, 1113.
118. X. Meng, Z. Liu, B. Cui, D. Qin, H. Geng, W. Cai, L. Fu, J. He, Z. Ren and J. Sui, *Advanced Energy Materials*, 2017, **7**, 1602582.
119. A. Zhang, B. Zhang, W. Lu, D. Xie, H. Ou, X. Han, J. Dai, X. Lu, G. Han, G. Wang and X. Zhou, *Advanced Functional Materials*, 2018, **28**, 1705117.
120. C. Wan, Y. Wang, W. Norimatsu, M. Kusunoki and K. Koumoto, *Applied Physics Letters*, 2012, **100**, 101913.
121. W. Zheng, D. Yang, P. Bi, C. He, F. Liu, J. Shi, Y. Ding, Z. Wang and R. Xiong, *Journal of Electronic Materials*, 2017, **46**, 2936-2943.
122. H. F. He, X. F. Li, Z. Q. Chen, Y. Zheng, D. W. Yang and X. F. Tang, *The Journal of Physical Chemistry C*, 2014, **118**, 22389-22394.
123. Filip Tuomisto, *Characterisation and Control of Defects in Semiconductors*, Institution of Engineering and Technology, London, United Kingdom, 2019.
124. M. Christensen, B. B. Iversen, L. Bertini, C. Gatti, M. Toprak, M. Muhammed and E. Nishibori, *Journal of Applied Physics*, 2004, **96**, 3148-3157.
125. M. Christensen, F. Juranyi and B. B. Iversen, *Physica B: Condensed Matter*, 2006, **385-386**, 505-507.
126. M. Christensen, A. B. Abrahamsen, N. B. Christensen, F. Juranyi, N. H. Andersen, K. Lefmann, J. Andreasson, C. R. H. Bahl and B. B. Iversen, *Nature Materials*, 2008, **7**, 811-815.
127. J. Mao, J. Shuai, S. Song, Y. Wu, R. Dally, J. Zhou, Z. Liu, J. Sun, Q. Zhang, C. dela Cruz, S. Wilson, Y. Pei, D. J. Singh, G. Chen, C.-W. Chu and Z. Ren, *Proceedings of the National Academy of Sciences*, 2017, **114**, 10548-10553.
128. S. W. Song, J. Mao, M. Bordelon, R. He, Y. M. Wang, J. Shuai, J. Y. Sun, X. B. Lei, Z. S. Ren, S. Chen, S. Wilson, K. Nielsch, Q. Y. Zhang and Z. F. Ren, *Materials Today Physics*, 2019, **8**, 25-33.
129. T. Kanno, H. Tamaki, M. Yoshiya, H. Uchiyama, S. Maki, M. Takata and Y. Miyazaki, *Advanced Functional Materials*, 2021, DOI: https://doi.org/10.1002/adfm.202008469, 2008469.
130. T. Fang, K. Xia, P. Nan, B. Ge, X. Zhao and T. Zhu, *Materials Today Physics*, 2020, **13**, 100200.
131. F. Qin, S. A. Nikolaev, A. Suwardi, M. Wood, Y. Zhu, X. Tan, U. Aydemir, Y. Ren, Q. Yan, L. Hu and G. J. Snyder, *Chemistry of Materials*, 2020, **32**, 10130-10139.
132. F. Böcher, S. P. Culver, J. Peilstöcker, K. S. Weldert and W. G. Zeier, *Dalton T*, 2017, **46**, 3906-3914.
133. G. Jiang, J. He, T. Zhu, C. Fu, X. Liu, L. Hu and X. Zhao, *Advanced Functional Materials*, 2014, **24**, 3776-3781.
134. N. Roth, T. Zhu and B. B. Iversen, *IUCrJ*, 2020, **7**, 673-680.
135. C. Xiao, X. Qin, J. Zhang, R. An, J. Xu, K. Li, B. Cao, J. Yang, B. Ye and Y. Xie, *Journal of the American Chemical Society*, 2012, **134**, 18460-18466.
136. Z. Li, C. Xiao, S. Fan, Y. Deng, W. Zhang, B. Ye and Y. Xie,

Journal of the American Chemical Society, 2015, **137**, 6587-6593.
137. S. Roychowdhury, M. K. Jana, J. Pan, S. N. Guin, D. Sanyal, U. V. Waghmare and K. Biswas, *Angewandte Chemie International Edition*, 2018, **57**, 4043-4047.
138. X. Tan, J.-L. Lan, K. Hu, B. Xu, Y. Liu, P. Zhang, X.-Z. Cao, Y. Zhu, W. Xu, Y.-H. Lin and C.-W. Nan, *Journal of the American Ceramic Society*, 2018, **101**, 4634-4644.
139. R. Deng, X. Su, S. Hao, Z. Zheng, M. Zhang, H. Xie, W. Liu, Y. Yan, C. Wolverton, C. Uher, M. G. Kanatzidis and X. Tang, *Energy & Environmental Science*, 2018, **11**, 1520-1535.
140. H. F. He, B. Zhao, N. Qi, B. Wang, Z. Q. Chen, X. L. Su and X. F. Tang, *Journal of Materials Science*, 2018, **53**, 12961-12973.
141. M. Dutta, D. Sanyal and K. Biswas, *Inorganic Chemistry*, 2018, **57**, 7481-7489.
142. F. Tuomisto and I. Makkonen, *Reviews of Modern Physics*, 2013, **85**, 1583-1631.
143. M. Guan, C. Xiao, J. Zhang, S. Fan, R. An, Q. Cheng, J. Xie, M. Zhou, B. Ye and Y. Xie, *Journal of the American Chemical Society*, 2013, **135**, 10411-10417.
144. M. Butterling, Positron Annihilation Spectroscopy at the HZDR, https://www.hzdr.de/db/Cms?pOid=35245&pNid=3581, (accessed 22 July 2020).
145. C. Fong, A. W. Dong, A. J. Hill, B. J. Boyd and C. J. Drummond, *Phys Chem Chem Phys*, 2015, **17**, 17527-17540.
146. T. Plirdpring, K. Kurosaki, A. Kosuga, M. Ishimaru, A. Harnwunggmoung, T. Sugahara, Y. Ohishi, H. Muta and S. Yamanaka, *MATERIALS TRANSACTIONS*, 2012, **53**, 1212-1215.
147. C.-e. Kim, K. Kurosaki, M. Ishimaru, H. Muta and S. Yamanaka, *Journal of Electronic Materials*, 2011, **40**, 999-1004.
148. Y. Gu, X. Liu, S. Huang, J. Guo, P. Bi, J. Shi, W. Zheng, Z. Wang and R. Xiong, *Ceram Int*, 2018, **44**, 21421-21427.
149. J. Fu, S. Song, X. Zhang, F. Cao, L. Zhou, X. Li and H. Zhang, *Crystengcomm*, 2012, **14**, 2159.
150. J. S. Son, M. K. Choi, M.-K. Han, K. Park, J.-Y. Kim, S. J. Lim, M. Oh, Y. Kuk, C. Park, S.-J. Kim and T. Hyeon, *Nano Letters*, 2012, **12**, 640-647.
151. X. Wang, Y. Yang and L. Zhu, *Journal of Applied Physics*, 2011, **110**, 024312.
152. S. G. Bishop, B. V. Shanabrook, P. B. Klein and R. L. Henry, *Physical Review B*, 1988, **38**, 8469-8472.
153. D. G. Thomas, J. J. Hopfield and C. J. Frosch, *Physical Review Letters*, 1965, **15**, 857-860.
154. D. V. Lang, *Journal of Applied Physics*, 1974, **45**, 3023-3032.
155. S. Majdi, M. Gabrysch, N. Suntornwipat, F. Burmeister, R. Jonsson, K. K. Kovi and A. Hallén, *Rev Sci Instrum*, 2019, **90**, 063903.
156. N. Peranio and O. Eibl, *physica status solidi (a)*, 2009, **206**, 42-49.
157. J.-J. Shen, T.-J. Zhu, X.-B. Zhao, S.-N. Zhang, S.-H. Yang and Z.-Z. Yin, *Energy & Environmental Science*, 2010, **3**, 1519-1523.
158. Z. Chen, Z. Jian, W. Li, Y. Chang, B. Ge, R. Hanus, J. Yang, Y. Chen, M. Huang, G. J. Snyder and Y. Pei, *Adv. Mater.*, 2017, **29**, 1606768.
159. H. Cheng, C. Lu, J. Liu, Y. Yan, X. Han, H. Jin, Y. Wang, Y. Liu and C. Wu, *Progress in Natural Science: Materials International*, 2017, **27**, 66-73.
160. F. C. Frank, *Discussions of the Faraday Society*, 1957, **23**, 122-127.
161. W. G. Johnston and J. J. Gilman, *Journal of Applied Physics*, 1960, **31**, 632-643.
162. Z. Chen, Z. Jian, W. Li, Y. Chang, B. Ge, R. Hanus, J. Yang, Y. Chen, M. Huang, G. J. Snyder and Y. Pei, *Adv Mater*, 2017, **29**, 1606768.
163. P. G. Klemens, *Proceedings of the Physical Society. Section A*, 1955, **68**, 1113-1128.
164. P. G. Klemens, in *Solid State Physics*, eds. F. Seitz and D. Turnbull, Academic Press, 1958, vol. 7, pp. 1-98.
165. J. Callaway, *Physical Review*, 1959, **113**, 1046-1051.
166. J. Callaway and H. C. von Baeyer, *Physical Review*, 1960, **120**, 1149-1154.
167. B. Abeles, *Physical Review*, 1963, **131**, 1906-1911.
168. A. Ioffe, S. Airapetyants, A. Ioffe, N. Kolomoets and L. Stil'bans, *Dokl. Akad. Nauk. SSSR*, 1956, **106**, 981.
169. M. C. Steele and F. D. Rosi, *Journal of Applied Physics*, 1958, **29**, 1517-1520.
170. H. J. Goldsmid, *Journal of Applied Physics*, 1961, **32**, 2198-2202.
171. V. Zaitsev, E. Tkalenko and E. Nikitin, *Sov Phys Solid State*, 1969, **11**, 221-224.
172. A. May, J.-P. Fleurial and G. Snyder, *Physical Review B*, 2008, **78**, 125205.
173. D. Cheikh, B. E. Hogan, T. Vo, P. Von Allmen, K. Lee, D. M. Smiadak, A. Zevalkink, B. S. Dunn, J.-P. Fleurial and S. K. Bux, *Joule*, 2018, **2**, 698-709.
174. A. F. May, J.-P. Fleurial and G. J. Snyder, *Chemistry of Materials*, 2010, **22**, 2995-2999.
175. J. M. Ma, S. M. Clarke, W. G. Zeier, T. Vo, P. Von Allmen, G. Jeffrey Snyder, R. B. Kaner, J.-P. Fleurial and S. K. Bux, *Journal of Materials Chemistry C*, 2015, **3**, 10459-10466.
176. A. F. May, M. A. McGuire, C. Cantoni and B. C. Sales, *Physical Review B*, 2012, **86**, 035135.
177. A. May, D. Singh and G. Snyder, *Physical Review B*, 2009, **79**, 153101.
178. H. Tamaki, H. K. Sato and T. Kanno, *Adv. Mater.*, 2016, **28**, 10182-10187.
179. C. L. Condron, S. M. Kauzlarich, F. Gascoin and G. J. Snyder, *Journal of Solid State Chemistry*, 2006, **179**, 2252-2257.
180. J. Mao, Y. Wu, S. Song, J. Shuai, Z. Liu, Y. Pei and Z. Ren, *Materials Today Physics*, 2017, **3**, 1-6.
181. J. Mao, Y. Wu, S. Song, Q. Zhu, J. Shuai, Z. Liu, Y. Pei and Z. Ren, *ACS Energy Letters*, 2017, **2**, 2245-2250.
182. G. Tan, S. Hao, R. C. Hanus, X. Zhang, S. Anand, T. P. Bailey, A. J. E. Rettie, X. Su, C. Uher, V. P. Dravid, G. J. Snyder, C. Wolverton and M. G. Kanatzidis, *ACS Energy Letters*, 2018, **3**, 705-712.
183. T. J. Slade, K. Pal, J. A. Grovogui, T. P. Bailey, J. Male, J. F. Khoury, X. Zhou, D. Y. Chung, G. J. Snyder, C. Uher, V. P. Dravid, C. Wolverton and M. G. Kanatzidis, *J. Am. Chem. Soc.*, 2020, DOI: 10.1021/jacs.0c05650.
184. J. Male, M. T. Agne, A. Goyal, S. Anand, I. T. Witting, V. Stevanović and G. J. Snyder, *Materials Horizons*, 2019, **6**, 1444-1453.
185. S. Ohno, U. Aydemir, M. Amsler, J.-H. Pöhls, S. Chanakian, A. Zevalkink, M. A. White, S. K. Bux, C. Wolverton and G. J. Snyder, *Adv. Funct. Mater.*, 2017, **27**, 1606361.
186. B. R. Ortiz, K. Gordiz, L. C. Gomes, T. Braden, J. M. Adamczyk, J. Qu, E. Ertekin and E. S. Toberer, *Journal of Materials Chemistry A*, 2019, **7**, 621-631.

187. X. Li, P. Yang, Y. Wang, Z. Zhang, D. Qin, W. Xue, C. Chen, Y. Huang, X. Xie, X. Wang, M. Yang, C. Wang, F. Cao, J. Sui, X. Liu and Q. Zhang, *Research*, 2020, **2020**, 4630948.
188. S. Ohno, K. Imasato, S. Anand, H. Tamaki, S. D. Kang, P. Gorai, H. K. Sato, E. S. Toberer, T. Kanno and G. J. Snyder, *Joule*, 2018, **2**, 141-154.
189. J. Zhang, L. Song, S. H. Pedersen, H. Yin, L. T. Hung and B. B. Iversen, *Nature Communications*, 2017, **8**, 13901.
190. J. Mao, J. Shuai, S. Song, Y. Wu, R. Dally, J. Zhou, Z. Liu, J. Sun, Q. Zhang, C. dela Cruz, S. Wilson, Y. Pei, D. J. Singh, G. Chen, C.-W. Chu and Z. Ren, *Proceedings of the National Academy of Sciences*, 2017, **114**, 10548-10553.
191. H. Tamaki, H. K. Sato and T. Kanno, *Adv. Mater.*, 2016, **28**, 10182-10187.
192. P. Gorai, B. R. Ortiz, E. S. Toberer and V. Stevanović, *Journal of Materials Chemistry A*, 2018, **6**, 13806-13815.
193. P. Gorai, E. S. Toberer and V. Stevanović, *Journal of Applied Physics*, 2019, **125**, 025105.
194. J. Mao, H. Zhu, Z. Ding, Z. Liu, G. A. Gamage, G. Chen and Z. Ren, *Science*, 2019, **365**, 495.
195. H. Muta, K. Kurosaki and S. Yamanaka, *Journal of Alloys and Compounds*, 2003, **350**, 292-295.
196. S. R. Popuri, A. J. M. Scott, R. A. Downie, M. A. Hall, E. Suard, R. Decourt, M. Pollet and J. W. G. Bos, *RSC Advances*, 2014, **4**, 33720-33723.
197. D. Flahaut, T. Mihara, R. Funahashi, N. Nabeshima, K. Lee, H. Ohta and K. Koumoto, *Journal of Applied Physics*, 2006, **100**, 084911.
198. L. D. Zhao, D. Berardan, Y. L. Pei, C. Byl, L. Pinsard-Gaudart and N. Dragoe, *Applied Physics Letters*, 2010, **97**, 092118.
199. G.-K. Ren, J.-L. Lan, K. J. Ventura, X. Tan, Y.-H. Lin and C.-W. Nan, *npj Computational Materials*, 2016, **2**, 16023.
200. I. Terasaki, Y. Sasago and K. Uchinokura, *Physical Review B*, 1997, **56**, R12685.
201. H. Ohta, K. Sugiura and K. Koumoto, *Inorg Chem*, 2008, **47**, 8429-8436.
202. J. D. Baran, D. Kepaptsoglou, M. Molinari, N. Kulwongwit, F. Azough, R. Freer, Q. M. Ramasse and S. C. Parker, *Chemistry of Materials*, 2016, **28**, 7470-7478.
203. A. V. Kovalevsky, K. V. Zakharchuk, M. H. Aguirre, W. Xie, S. G. Patrício, N. M. Ferreira, D. Lopes, S. A. Sergiienko, G. Constantinescu, S. M. Mikhalev, A. Weidenkaff and J. R. Frade, *Journal of Materials Chemistry A*, 2020, **8**, 7317-7330.
204. A. V. Kovalevsky, M. H. Aguirre, S. Populoh, S. G. Patrício, N. M. Ferreira, S. M. Mikhalev, D. P. Fagg, A. Weidenkaff and J. R. Frade, *Journal of Materials Chemistry A*, 2017, **5**, 3909-3922.
205. P. H. Tsai, T. Norby, T. T. Tan, R. Donelson, Z. D. Chen and S. Li, *Applied Physics Letters*, 2010, **96**, 141905.
206. M. Molinari, D. A. Tompsett, S. C. Parker, F. Azough and R. Freer, *Journal of Materials Chemistry A*, 2014, **2**, 14109-14117.
207. W. Li and N. Mingo, *Physical Review B*, 2015, **91**, 144304.
208. J. Yang, W. Zhang, S. Q. Bai, Z. Mei and L. D. Chen, *Applied Physics Letters*, 2007, **90**, 192111.
209. V. Keppens, D. Mandrus, B. C. Sales, B. C. Chakoumakos, P. Dai, R. Coldea, M. B. Maple, D. A. Gajewski, E. J. Freeman and S. Bennington, *Nature*, 1998, **395**, 876-878.
210. B. C. Sales, B. C. Chakoumakos, D. Mandrus and J. W. Sharp, *Journal of Solid State Chemistry France*, 1999, **146**, 528-532.
211. M. Zebarjadi, K. Esfarjani, J. Yang, Z. F. Ren and G. Chen, *Physical Review B*, 2010, **82**, 195207.
212. X. Shi, J. Yang, J. R. Salvador, M. Chi, J. Y. Cho, H. Wang, S. Bai, J. Yang, W. Zhang and L. Chen, *Journal of the American Chemical Society*, 2011, **133**, 7837-7846.
213. Y. Pei, L. Zheng, W. Li, S. Lin, Z. Chen, Y. Wang, X. Xu, H. Yu, Y. Chen and B. Ge, *Advanced Electronic Materials*, 2016, **2**, 1600019.
214. W. Li, L. Zheng, B. Ge, S. Lin, X. Zhang, Z. Chen, Y. Chang and Y. Pei, *Advanced Materials*, 2017, **29**, 1605887.
215. X. Liu, L. Xi, W. Qiu, J. Yang, T. Zhu, X. Zhao and W. Zhang, *Advanced Electronic Materials*, 2016, **2**, 1500284.
216. L. Hu, T. Zhu, Y. Wang, H. Xie, Z. Xu and X. Zhao, *NPG Asia Mater.*, 2014, **6**, e88.
217. Z. Starý, J. Horák, M. Stordeur and M. Stölzer, *J Phys Chem Solids*, 1988, **49**, 29-34.
218. L. Ivanova and Y. V. Granatkina, *Inorg Mater+*, 1995, **31**, 678-681.
219. Y. W. Chai, K. Yoshioka and Y. Kimura, *Scripta Mater*, 2014, **83**, 13-16.
220. P. Qiu, J. Yang, X. Huang, X. Chen and L. Chen, *Applied Physics Letters*, 2010, **96**, 152105.
221. J. M. Hodges, S. Hao, J. A. Grovogui, X. Zhang, T. P. Bailey, X. Li, Z. Gan, Y.-Y. Hu, C. Uher, V. P. Dravid, C. Wolverton and M. G. Kanatzidis, *J. Am. Chem. Soc.*, 2018, **140**, 18115-18123.
222. S. Cai, S. Hao, Z.-Z. Luo, X. Li, I. Hadar, T. P. Bailey, X. Hu, C. Uher, Y.-Y. Hu, C. Wolverton, V. P. Dravid and M. G. Kanatzidis, *Energy & Environmental Science*, 2020, **13**, 200-211.
223. Z.-Z. Luo, S. Hao, X. Zhang, X. Hua, S. Cai, G. Tan, T. P. Bailey, R. Ma, C. Uher, C. Wolverton, V. P. Dravid, Q. Yan and M. G. Kanatzidis, *Energy & Environmental Science*, 2018, **11**, 3220-3230.
224. J. M. Hodges, Y. Xia, C. D. Malliakas, G. C. B. Alexander, M. K. Y. Chan and M. G. Kanatzidis, *Chem. Mater.*, 2018, **30**, 7245-7254.
225. H.-S. Kim, S. D. Kang, Y. Tang, R. Hanus and G. Jeffrey Snyder, *Mater. Horiz.*, 2016, **3**, 234-240.
226. S. I. Kim, K. H. Lee, H. A. Mun, H. S. Kim, S. W. Hwang, J. W. Roh, D. J. Yang, W. H. Shin, X. S. Li, Y. H. Lee, G. J. Snyder and S. W. Kim, *Science*, 2015, **348**, 109-114.
227. Y. Lee, S.-H. Lo, C. Chen, H. Sun, D.-Y. Chung, T. C. Chasapis, C. Uher, V. P. Dravid and M. G. Kanatzidis, *Nature Communications*, 2014, **5**, 3640.
228. H. Wang, Y. Pei, A. D. LaLonde and G. J. Snyder, *Proceedings of the National Academy of Sciences*, 2012, **109**, 9705-9709.
229. A. D. LaLonde, Y. Pei and G. J. Snyder, *Energy & Environmental Science*, 2011, **4**, 2090.
230. J. Xin, H. Wu, X. Liu, T. Zhu, G. Yu and X. Zhao, *Nano Energy*, 2017, **34**, 428-436.
231. Y. Wang, C. Fu, T. Zhu, L. Hu, G. Jiang, G. Zhao, D. Huo and X. Zhao, *Journal of Applied Physics*, 2013, **114**, 184904.
232. R. Deng, X. Su, Z. Zheng, W. Liu, Y. Yan, Q. Zhang, V. P. Dravid, C. Uher, M. G. Kanatzidis and X. Tang, *Sci. Adv.*, 2018, **4**, eaar5606.
233. W. Xie, X. Tang, Y. Yan, Q. Zhang and T. M. Tritt, *Applied Physics Letters*, 2009, **94**, 102111.
234. R. J. Mehta, Y. Zhang, C. Karthik, B. Singh, R. W. Siegel, T. Borca-Tasciuc and G. Ramanath, *Nat. Mater.*, 2012, **11**, 233-240.
235. G. Joshi, H. Lee, Y. Lan, X. Wang, G. Zhu, D. Wang, R. W. Gould, D. C. Cuff, M. Y. Tang and M. S. Dresselhaus, *Nano Lett.*, 2008, **8**, 4670-4674.

236. S. Bathula, M. Jayasimhadri, N. Singh, A. K. Srivastava, J. Pulikkotil, A. Dhar and R. C. Budhani, *Applied Physics Letters*, 2012, **101**, 213902-213905.
237. X. Yan, G. Joshi, W. Liu, Y. Lan, H. Wang, S. Lee, J. W. Simonson, S. J. Poon, T. M. Tritt, G. Chen and Z. F. Ren, *Nano Letters*, 2011, **11**, 556-560.
238. F. Li, J.-F. Li, L.-D. Zhao, K. Xiang, Y. Liu, B.-P. Zhang, Y.-H. Lin, C.-W. Nan and H.-M. Zhu, *Energy Environ. Sci.*, 2012, **5**, 7188-7195.
239. E. S. Toberer, A. Zevalkink, N. Crisosto and G. J. Snyder, *Adv. Funct. Mater.*, 2010, **20**, 4375-4380.
240. B. Yu, W. Liu, S. Chen, H. Wang, H. Wang, G. Chen and Z. Ren, *Nano Energy*, 2012, **1**, 472-478.
241. H. Liu, X. Zhang, S. Li, Z. Zhou, Y. Liu and J. Zhang, *J Electron Mater*, 2017, **46**, 2629-2633.
242. X. Zhang, Y. Zhou, Y. Pei, Y. Chen, B. Yuan, S. Zhang, Y. Deng, S. Gong, J. He and L.-D. Zhao, *Journal of Alloys and Compounds*, 2017, **709**, 575-580.
243. C.-F. Wu, T.-R. Wei and J.-F. Li, *Phys Chem Chem Phys*, 2015, **17**, 13006-13012.
244. W.-S. Liu, B.-P. Zhang, L.-D. Zhao and J.-F. Li, *Chemistry of Materials*, 2008, **20**, 7526-7531.
245. G. Tan, Y. Zheng and X. Tang, *Applied Physics Letters*, 2013, **103**, 183904.
246. Q. Zhang, Y. Zheng, X. Su, K. Yin, X. Tang and C. Uher, *Scripta Mater*, 2015, **96:**, 1-4.
247. W. Luo, H. Li, F. Fu, W. Hao and X. Tang, *J Electron Mater*, 2011, **40**, 1233-1237.
248. W. Zheng, B. Xu, L. Zhou, Y. Zhou, H. Zheng, C. Sun, E. Shi, T. D. Fink and Y. Wu, *Nano Res.*, 2017, **10**, 1498-1509.
249. K. W. Shah, S.-X. Wang, Y. Zheng and J. Xu, *Applied Sciences*, 2019, **9**, 1511.
250. L. Yang, Z.-G. Chen, G. Han, M. Hong, Y. Zou and J. Zou, *Nano Energy*, 2015, **16**, 367-374.
251. J. Martin, L. Wang, L. Chen and G. S. Nolas, *Phys. Rev. B*, 2009, **79**, 115311.
252. J. J. Kuo, S. D. Kang, K. Imasato, H. Tamaki, S. Ohno, T. Kanno and G. J. Snyder, *Energy & Environmental Science*, 2018, DOI: 10.1039/C7EE03326E.
253. A. Zevalkink, W. G. Zeier, G. Pomrehn, E. Schechtel, W. Tremel and G. J. Snyder, *Energy & Environmental Science*, 2012, **5**, 9121-9128.
254. E. S. Toberer, A. Zevalkink, N. Crisosto and G. J. Snyder, *Adv. Funct. Mater.*, 2010, **20**, 4375-4380.
255. W. G. Zeier, A. Zevalkink, E. Schechtel, W. Tremel and G. J. Snyder, *J. Mater. Chem.*, 2012, **22**, 9826-9830.
256. Q. Qiu, Y. Liu, K. Xia, T. Fang, J. Yu, X. Zhao and T. Zhu, *Advanced Energy Materials*, 2019, **9**, 1803447.
257. R. He, D. Kraemer, J. Mao, L. Zeng, Q. Jie, Y. Lan, C. Li, J. Shuai, H. S. Kim, Y. Liu, D. Broido, C.-W. Chu, G. Chen and Z. Ren, *Proceedings of the National Academy of Sciences*, 2016, **113**, 13576-13581.
258. T. J. Slade, T. P. Bailey, J. A. Grovogui, X. Hua, X. Zhang, J. J. Kuo, I. Hadar, G. J. Snyder, C. Wolverton, V. P. Dravid, C. Uher and M. G. Kanatzidis, *Advanced Energy Materials*, 2019, **9**, 1901377.
259. K. F. Cai, X. R. He, M. Avdeev, D. H. Yu, J. L. Cui and H. Li, *J. Solid State Chem.*, 2008, **181**, 1434-1438.
260. L. Pan, S. Mitra, L.-D. Zhao, Y. Shen, Y. Wang, C. Felser and D. Berardan, *Adv. Funct. Mater.*, 2016, **26**, 5149-5157.
261. J. J. Kuo, S. D. Kang, K. Imasato, H. Tamaki, S. Ohno, T. Kanno and G. J. Snyder, *Energy & Environmental Science*, 2018, **11**, 429-434.
262. T. Kanno, H. Tamaki, H. K. Sato, S. D. Kang, S. Ohno, K. Imasato, J. J. Kuo, G. J. Snyder and Y. Miyazaki, *Appl. Phys. Lett.*, 2018, **112**, 033903.
263. K. Imasato, C. Fu, Y. Pan, M. Wood, J. J. Kuo, C. Felser and G. J. Snyder, *Advanced Materials*, 2020, **32**, 1908218.
264. T. Slade, J. Grovogui, J. J. Kuo, S. Anand, T. Bailey, M. Wood, C. Uher, G. J. Snyder, V. Dravid and M. G. Kanatzidis, *Energy & Environmental Science*, 2020, DOI: 10.1039/D0EE00491J.
265. J. J. Kuo, Y. Yu, S. D. Kang, O. Cojocaru-Mirédin, M. Wuttig and G. J. Snyder, *Advanced Materials Interfaces*, 2019, **6**, 1900429.
266. A. Zevalkink, W. G. Zeier, G. Pomrehn, E. Schechtel, W. Tremel and G. J. Snyder, *Energy & Environmental Science*, 2012, **5**, 9121-9128.
267. T.-R. Wei, G. Tan, X. Zhang, C.-F. Wu, J.-F. Li, V. P. Dravid, G. J. Snyder and M. G. Kanatzidis, *J. Am. Chem. Soc.*, 2016, **138**, 8875-8882.
268. J. de Boor, T. Dasgupta, H. Kolb, C. Compere, K. Kelm and E. Mueller, *Acta Mater.*, 2014, **77**, 68-75.
269. T. J. Slade, J. A. Grovogui, J. J. Kuo, S. Anand, T. P. Bailey, M. Wood, C. Uher, G. J. Snyder, V. P. Dravid and M. G. Kanatzidis, *Energy & Environmental Science*, 2020, **13**, 1509-1518.
270. M. Wood, J. J. Kuo, K. Imasato and G. J. Snyder, *Adv. Mater.*, 2019, **31**, 1902337.
271. L.-D. Zhao, G. Tan, S. Hao, J. He, Y. Pei, H. Chi, H. Wang, S. Gong, H. Xu, V. P. Dravid, C. Uher, G. J. Snyder, C. Wolverton and M. G. Kanatzidis, *Science*, 2016, **351**, 141-144.
272. Y. K. Lee, Z. Luo, S. P. Cho, M. G. Kanatzidis and I. Chung, *Joule*, 2019, **3**, 719-731.
273. J. J. Kuo, M. Wood, T. J. Slade, M. G. Kanatzidis and G. J. Snyder, *Energy & Environmental Science*, 2020, DOI: 10.1039/C9EE03921J.
274. V. Carteaux, D. Brunet, G. Ouvrard and G. Andre, *Journal of Physics: Condensed Matter*, 1995, **7**, 69.
275. R. Lefèvre, D. Berthebaud, O. Lebedev, O. Pérez, C. Castro, S. Gascoin, D. Chateigner and F. Gascoin, *Journal of Materials Chemistry A*, 2017, **5**, 19406-19415.
276. Y. Luo, S. Cai, S. Hao, F. Pielnhofer, I. Hadar, Z.-Z. Luo, J. Xu, C. Wolverton, V. P. Dravid, A. Pfitzner, Q. Yan and M. G. Kanatzidis, *Joule*, 2020, **4**, 159-175.
277. C. L. Wan, Y. F. Wang, Y. E. Putri and K. Koumoto, in *Thermoelectric Nanomaterials: Materials Design and Applications*, eds. K. Koumoto and T. Mori, Springer Berlin Heidelberg, Berlin, Heidelberg, 2013, pp. 157-173.
278. C. Wan, Y. Wang, N. Wang and K. Koumoto, *Materials*, 2010, **3**, 2606.
279. J. He, S. N. Girard, J.-C. Zheng, L. Zhao, M. G. Kanatzidis and V. P. Dravid, *Advanced Materials*, 2012, **24**, 4440-4444.
280. Z. Liu, Y. Zhang, J. Mao, W. Gao, Y. Wang, J. Shuai, W. Cai, J. Sui and Z. Ren, *Acta Materialia*, 2017, **128**, 227-234.
281. Y. Zheng, C. Liu, L. Miao, C. Li, R. Huang, J. Gao, X. Wang, J. Chen, Y. Zhou and E. Nishibori, *Nano Energy*, 2019, **59**, 311-320.
282. Y. Luo, J. Yang, G. Li, M. Liu, Y. Xiao, L. Fu, W. Li, P. Zhu, J. Peng and S. Gao, *Advanced Energy Materials*, 2014, **4**, 1300599.
283. S. N. Girard, K. Schmidt‐Rohr, T. C. Chasapis, E. Hatzikraniotis, B. Njegic, E. Levin, A. Rawal, K. M. Paraskevopoulos and M. G. Kanatzidis, *Advanced Functional Materials*, 2013, **23**, 747-757.
284. J. Androulakis, C.-H. Lin, H.-J. Kong, C. Uher, C.-I. Wu, T.

Hogan, B. A. Cook, T. Caillat, K. M. Paraskevopoulos and M. G. Kanatzidis, *Journal of the American Chemical Society*, 2007, **129**, 9780-9788.
285. Y. Pei, J. Lensch‐Falk, E. S. Toberer, D. L. Medlin and G. J. Snyder, *Advanced Functional Materials*, 2011, **21**, 241-249.
286. Z. Dan, B. Hong-Chang, L. Zhi-Liang, W. Jiang-Long, F. Guang-Sheng and W. Shu-Fang, *Chin. Phys. B*, 2018, **27**, 047206.
287. S. N. Girard, J. He, X. Zhou, D. Shoemaker, C. M. Jaworski, C. Uher, V. P. Dravid, J. P. Heremans and M. G. Kanatzidis, *Journal of the American Chemical Society*, 2011, **133**, 16588-16597.
288. C. J. Vineis, A. Shakouri, A. Majumdar and M. G. Kanatzidis, *Advanced Materials*, 2010, **22**, 3970-3980.
289. S. N. Girard, K. Schmidt-Rohr, T. C. Chasapis, E. Hatzikraniotis, B. Njegic, E. M. Levin, A. Rawal, K. M. Paraskevopoulos and M. G. Kanatzidis, *Advanced Functional Materials*, 2013, **23**, 747-757.
290. D. Wu, L.-D. Zhao, X. Tong, W. Li, L. Wu, Q. Tan, Y. Pei, L. Huang, J.-F. Li and Y. Zhu, *Energy & Environmental Science*, 2015, **8**, 2056-2068.
291. S. Gorsse, P. Bauer Pereira, R. Decourt and E. Sellier, *Chemistry of Materials*, 2009, **22**, 988-993.
292. Z. Z. Luo, X. Zhang, X. Hua, G. Tan, T. P. Bailey, J. Xu, C. Uher, C. Wolverton, V. P. Dravid and Q. Yan, *Advanced Functional Materials*, 2018, 1801617.
293. Y. Gelbstein, Y. Rosenberg, Y. Sadia and M. P. Dariel, *The Journal of Physical Chemistry C*, 2010, **114**, 13126-13131.
294. Y. Gelbstein, J. Davidow, S. N. Girard, D. Y. Chung and M. Kanatzidis, *Advanced Energy Materials*, 2013, **3**, 815-820.
295. X. Meng, W. Cai, Z. Liu, J. Li, H. Geng and J. Sui, *Acta Materialia*, 2015, **98**, 405-415.
296. M. Gürth, G. Rogl, V. Romaka, A. Grytsiv, E. Bauer and P. Rogl, *Acta Materialia*, 2016, **104**, 210-222.
297. A. Page, C. Uher, P. F. Poudeu and A. Van der Ven, *Physical Review B*, 2015, **92**, 174102.
298. J. P. A. Makongo, D. K. Misra, X. Zhou, A. Pant, M. R. Shabetai, X. Su, C. Uher, K. L. Stokes and P. F. P. Poudeu, *J. Am. Chem. Soc.*, 2011, **133**, 18843-18852.
299. P. Sahoo, Y. Liu, J. P. A. Makongo, X.-L. Su, S. J. Kim, N. Takas, H. Chi, C. Uher, X. Pan and P. F. P. Poudeu, *Nanoscale*, 2013, **5**, 9419-9427.
300. R. Lu, J. S. Lopez, Y. Liu, T. P. Bailey, A. A. Page, S. Wang, C. Uher and P. F. P. Poudeu, *Journal of Materials Chemistry A*, 2019, **7**, 11095-11103.
301. K. Biswas, J. He, Q. Zhang, G. Wang, C. Uher, V. P. Dravid and M. G. Kanatzidis, *Nature chemistry*, 2011, **3**, 160.
302. Z. Zhou, J. Yang, Q. Jiang, Y. Luo, D. Zhang, Y. Ren, X. He and J. Xin, *Journal of Materials Chemistry A*, 2016, **4**, 13171-13175.
303. L.-D. Zhao, X. Zhang, H. Wu, G. Tan, Y. Pei, Y. Xiao, C. Chang, D. Wu, H. Chi and L. Zheng, *Journal of the American Chemical Society*, 2016, **138**, 2366-2373.
304. Y. Luo, S. Cai, X. Hua, H. Chen, Q. Liang, C. Du, Y. Zheng, J. Shen, J. Xu and C. Wolverton, *Advanced Energy Materials*, 2018, 1803072.
305. Y. Luo, Q. Jiang, J. Yang, W. Li, D. Zhang, Z. Zhou, Y. Cheng, Y. Ren, X. He and X. Li, *Nano Energy*, 2017, **32**, 80-87.
306. Y. Luo, J. Yang, Q. Jiang, W. Li, D. Zhang, Z. Zhou, Y. Cheng, Y. Ren and X. He, *Acta Materialia*, 2017, **127**, 185-191.
307. Y. Luo, J. Yang, Q. Jiang, L. Fu, Y. Xiao, W. Li, D. Zhang, Z. Zhou and Y. Cheng, *Nano Energy*, 2015, **15**, 709-718.
308. A. Bhardwaj and D. Misra, *Journal of Materials Chemistry A*, 2014, **2**, 20980-20989.
309. Y. Cheng, J. Yang, Q. Jiang, D. He, J. He, Y. Luo, D. Zhang, Z. Zhou, Y. Ren and J. Xin, *Journal of Materials Chemistry A*, 2017, **5**, 5163-5170.
310. J. Xin, Q. Jiang, Y. Wen, S. Li, J. Zhang, A. Basit, L. Shu, X. Li and J. Yang, *Journal of Materials Chemistry A*, 2018, **6**, 17049-17056.
311. Y. Zhang, L. Wu, J. Zhang, J. Xing and J. Luo, *Acta Materialia*, 2016, **111**, 202-209.
312. P. F. P. Poudeu, J. D'Angelo, A. D. Downey, J. L. Short, T. P. Hogan and M. G. Kanatzidis, *Angew. Chem. Int. Ed.*, 2006, **45**, 3835-3839.
313. T. J. Slade, J. A. Grovogui, S. Hao, T. P. Bailey, R. Ma, X. Hua, A. Guéguen, C. Uher, C. Wolverton, V. P. Dravid and M. G. Kanatzidis, *J. Am. Chem. Soc.*, 2018, **140**, 7021-7031.
314. S. Li, J. Xin, A. Basit, Q. Long, S. Li, Q. Jiang, Y. Luo and J. Yang, *Advanced Science*, 2020, **7**, 1903493.
315. Y. Luo, J. Yang, Q. Jiang, W. Li, Y. Xiao, L. Fu, D. Zhang, Z. Zhou and Y. Cheng, *Nano Energy*, 2015, **18**, 37-46.
316. Y. Luo, J. Yang, Q. Jiang, W. Li, D. Zhang, Z. Zhou, Y. Cheng, Y. Ren and X. He, *Advanced Energy Materials*, 2016, **6**, 1600007.
317. S. Ahmad, A. Singh, A. Bohra, R. Basu, S. Bhattacharya, R. Bhatt, K. Meshram, M. Roy, S. K. Sarkar and Y. Hayakawa, *Nano Energy*, 2016, **27**, 282-297.
318. K. Favier, G. Bernard-Granger, C. Navone, M. Soulier, M. Boidot, J. Leforestier, J. Simon, J.-C. Tedenac and D. Ravot, *Acta Materialia*, 2014, **64**, 429-442.
319. M. H. Elsheikh, M. F. M. Sabri, S. M. Said, Y. Miyazaki, H. Masjuki, D. A. Shnawah, S. Naito and M. B. A. Bashir, *Journal of Materials Science*, 2017, **52**, 5324-5332.
320. E. B. Kim, P. Dharmaiah, K.-H. Lee, C.-H. Lee, J.-H. Lee, J.-K. Yang, D.-H. Jang, D.-S. Kim and S.-J. Hong, *Journal of Alloys and Compounds*, 2019, **777**, 703-711.
321. G. Constantinescu, A. R. Sarabando, S. Rasekh, D. Lopes, S. Sergiienko, P. Amirkhizi, J. R. Frade and A. V. Kovalevsky, *Materials*, 2020, **13**, 1060.
322. D. Srivastava, C. Norman, F. Azough, M. C. Schäfer, E. Guilmeau and R. Freer, *Journal of Alloys and Compounds*, 2018, **731**, 723-730.
323. A. V. Kovalevsky, S. Populoh, S. G. Patrício, P. Thiel, M. C. Ferro, D. P. Fagg, J. R. Frade and A. Weidenkaff, *The Journal of Physical Chemistry C*, 2015, **119**, 4466-4478.
324. F. Ren, H. Wang, P. A. Menchhofer and J. O. Kiggans, *Applied Physics Letters*, 2013, **103**, 221907.
325. B. Trawiński, B. Bochentyn, N. Gostkowska, M. Łapiński, T. Miruszewski and B. Kusz, *Mater Res Bull*, 2018, **99**, 10-17.
326. J. Lei, D. Zhang, W. Guan, Z. Ma, Z. Cheng, C. Wang and Y. Wang, *Applied Physics Letters*, 2018, **113**, 083901.
327. F. Chu, Q. Zhang, Z. Zhou, D. Hou, L. Wang and W. Jiang, *Journal of Alloys and Compounds*, 2018, **741**, 756-764.
328. Y. Zhang, H. Ma, B. Sun, B. Liu, H. Liu, L. Kong, B. Liu, X. Jia and X. Chen, *Journal of Alloys and Compounds*, 2017, **715**, 344-348.
329. K. Yin, X. Su, Y. Yan, H. Tang, M. G. Kanatzidis, C. Uher and X. Tang, *Scripta Mater*, 2017, **126**, 1-5.
330. L. Wang, Z. Zhang, L. Geng, T. Yuan, Y. Liu, J. Guo, L. Fang, J. Qiu and S. Wang, *Energy & Environmental Science*, 2018, **11**, 1307-1317.
331. D. Liu, J. Li, C. Chen and B. Zhang, *J Electron Mater*, 2011, **40**, 992-998.

332. J. Li, Q. Tan, J. F. Li, D. W. Liu, F. Li, Z. Y. Li, M. Zou and K. Wang, *Adv. Funct. Mater.*, 2013, **23**, 4317-4323.
333. P. Qin, Z.-H. Ge and J. Feng, *Journal of Alloys and Compounds*, 2017, **696**, 782-787.
334. R. Inoue, J. Nakano, T. Nakamura, T. Ube, T. Iida and Y. Kogo, *Journal of Alloys and Compounds*, 2019, **775**, 657-666.
335. B. Duan, P. Zhai, P. Wen, S. Zhang, L. Liu and Q. Zhang, *Scripta Mater*, 2012, **67**, 372-375.
336. P. Wen, B. Duan, P. Zhai, P. Li and Q. Zhang, *Journal of Materials Science: Materials in Electronics*, 2013, **24**, 5155-5161.
337. S.-J. Joo, J.-H. Son, B.-K. Min, J.-E. Lee, B.-S. Kim, B. Ryu, S.-D. Park and H.-W. Lee, *J Korean Phys Soc*, 2016, **69**, 1314-1320.
338. S. M. K. N. Islam, M. Li, U. Aydemir, X. Shi, L. Chen, G. J. Snyder and X. Wang, *Journal of Materials Chemistry A*, 2018, **6**, 18409-18416.
339. K. I. Bolotin, K. Sikes, Z. Jiang, M. Klima, G. Fudenberg, J. Hone, P. Kim and H. Stormer, *Solid State Commun*, 2008, **146**, 351-355.
340. M. F. L. De Volder, S. H. Tawfick, R. H. Baughman and A. J. Hart, *Science*, 2013, **339**, 535-539.
341. A. Hirsch, *Nat Mater*, 2010, **9**, 868.
342. Y. Lin, M. Wood, K. Imasato, J. J. Kuo, D. Lam, A. N. Mortazavi, T. J. Slade, S. A. Hodge, K. Xi, M. G. Kanatzidis, D. R. Clarke, M. C. Hersam and G. J. Snyder, *Energy & Environmental Science*, 2020, **13**, 4114-4121.
343. M. Bachmann, M. Czerner and C. Heiliger, *Physical Review B*, 2012, **86**, 115320.
344. L. Zhao, S. M. K. N. Islam, J. Wang, D. L. Cortie, X. Wang, Z. Cheng, J. Wang, N. Ye, S. Dou and X. Shi, *Nano energy*, 2017, **41**, 164-171.
345. R. Nunna, P. Qiu, M. Yin, H. Chen, R. Hanus, Q. Song, T. Zhang, M.-Y. Chou, M. T. Agne, J. He, G. J. Snyder, X. Shi and L. Chen, *Energy & Environmental Science*, 2017, **10**, 1928-1935.
346. H. Tang, F.-H. Sun, J.-F. Dong, Asfandiyar, H.-L. Zhuang, Y. Pan and J.-F. Li, *Nano Energy*, 2018, **49**, 267-273.
347. M. Li, S. M. K. N. Islam, M. Yahyaoglu, D. Pan, X. Shi, L. Chen, U. Aydemir and X. Wang, *InfoMat*, 2019, **1**, 108-115.
348. M. Li, D. L. Cortie, J. Liu, D. Yu, S. M. K. N. Islam, L. Zhao, D. R. G. Mitchell, R. A. Mole, M. B. Cortie, S. Dou and X. Wang, *Nano Energy*, 2018, **53**, 993-1002.
349. D. Suh, S. Lee, H. Mun, S.-H. Park, K. H. Lee, S. Wng Kim, J.-Y. Choi and S. Baik, *Nano Energy*, 2015, **13**, 67-76.
350. K. S. Kim, Y. Zhao, H. Jang, S. Y. Lee, J. M. Kim, K. S. Kim, J.-H. Ahn, P. Kim, J.-Y. Choi and B. H. Hong, *Nature*, 2009, **457**, 706.
351. J. Dong, W. Liu, H. Li, X. Su, X. Tang and C. Uher, *Journal of Materials Chemistry A*, 2013, **1**, 12503-12511.
352. K. T. Kim, S. Y. Choi, E. H. Shin, K. S. Moon, H. Y. Koo, G.-G. Lee and G. H. Ha, *Carbon*, 2013, **52**, 541-549.
353. Y. H. Yeo and T. S. Oh, *Mater. Res. Bull.*, 2014, **58**, 54-58.
354. B. Khasimsaheb, N. K. Singh, S. Bathula, B. Gahtori, D. Haranath and S. Neeleshwar, *Current Applied Physics*, 2017, **17**, 306-313.
355. L. D. Zhao, S. H. Lo, Y. Zhang, H. Sun, G. Tan, C. Uher, C. Wolverton, V. P. Dravid and M. G. Kanatzidis, *Nature*, 2014, **508**, 373-377.
356. D. Zhao, J. Ning, D. Wu and M. Zuo, *Materials*, 2016, **9**, 629.
357. V. Kulbachinskii, V. Kytin, M. Popov, S. Buga, V. Blank and P. Stepanov, *AIP Conf. Proc.*, 2012, **1449**, 283-286.
358. N. Gothard, J. E. Spowart and T. M. Tritt, *physica status solidi (a)*, 2010, **207**, 157-162.
359. Z. Wang, A. Vemishetti, J. I. Ejembi, G. Wei, B. Zhang, L. Wang, Y. Zhang, S. Guo, J. Luo, C. Chepko, Q. Dai, J. Tang and G.-L. Zhao, *Materials Science and Engineering: B*, 2016, **205**, 36-39.
360. V. A. Kulbachinskii, V. G. Kytin, M. Y. Popov, S. G. Buga, P. B. Stepanov and V. D. Blank, *J. Solid State Chem.*, 2012, **193**, 64-70.
361. V. A. Kulbachinskii, V. G. Kytin, V. D. Blank, S. G. Buga and M. Y. Popov, *Semiconductors*, 2011, **45**, 1194.
362. V. D. Blank, S. G. Buga, V. A. Kulbachinskii, V. G. Kytin, V. V. Medvedev, M. Y. Popov, P. B. Stepanov and V. F. Skok, *Phys. Rev. B*, 2012, **86**, 075426.
363. X. Shi, L. D. Chen, S. Q. Bai, X. Y. Huang, X. Y. Zhao, Q. Yao and C. Uher, *J. Appl. Phys.*, 2007, **102**, 103709.
364. T. Itoh, K. Ishikawa and A. Okada, *J. Mater. Res.*, 2011, **22**, 249-253.
365. N. O. Balayeva and Z. Q. Mamiyev, *Mater. Lett.*, 2016, **175**, 231-235.
366. S. Bathula, M. Jayasimhadri, B. Gahtori, A. Kumar, A. K. Srivastava and A. Dhar, *Phys. Chem. Chem. Phys.*, 2017, **19**, 25180-25185.
367. Z.-Y. Li, J.-F. Li, W.-Y. Zhao, Q. Tan, T.-R. Wei, C.-F. Wu and Z.-B. Xing, *Appl. Phys. Lett.*, 2014, **104**, 113905.
368. T. Akao, K. Uya, T. Onda and Z.-C. Chen, *2014*, 2014, 5.
369. Y. Pan, U. Aydemir, F.-H. Sun, C.-F. Wu, T. C. Chasapis, G. J. Snyder and J.-F. Li, *Advanced Science*, 2017, **4**, 1700259.
370. T. Akao, Y. Fujiwara, Y. Tarui, T. Onda and Z.-C. Chen, *J Electron Mater*, 2014, **43**, 2047-2052.
371. L.-D. Zhao, B.-P. Zhang, J.-F. Li, M. Zhou, W.-S. Liu and J. Liu, *Journal of Alloys and Compounds*, 2008, **455**, 259-264.
372. K. Yin, X. Su, Y. Yan, H. Tang, M. G. Kanatzidis, C. Uher and X. Tang, *Scr. Mater.*, 2017, **126**, 1-5.
373. J. Li, Q. Tan, J.-F. Li, D.-W. Liu, F. Li, Z.-Y. Li, M. Zou and K. Wang, *Advanced Functional Materials*, 2013, **23**, 4317-4323.
374. P. Yu, A. Umut, G. J. A., W. I. T., H. Riley, X. Yaobin, W. Jinsong, W. Chao-Feng, S. Fu-Hua, Z. Hua-Lu, D. Jin-Feng, L. Jing-Feng, D. V. P. and S. G. Jeffrey, *Advanced Materials*, 2018, **30**, 1802016.
375. B. Xu, M. T. Agne, T. Feng, T. C. Chasapis, X. Ruan, Y. Zhou, H. Zheng, J. H. Bahk, M. G. Kanatzidis, G. J. Snyder and Y. Wu, *Adv. Mater.*, 2017, **29**, 1605140.
376. B. Xu, T. Feng, M. T. Agne, L. Zhou, X. Ruan, G. J. Snyder and Y. Wu, *Angew. Chem. Int. Ed.*, 2017, **56**, 3546-3551.
377. W. Liu, X. Shi, R. Moshwan, M. Hong, L. Yang, Z.-G. Chen and J. Zou, *Sustainable Materials and Technologies*, 2018, **17**, e00076.
378. B. Du, H. Li, J. Xu, X. Tang and C. Uher, *Journal of Solid State Chemistry*, 2011, **184**, 109-114.
379. Y. Zhao, L. Yang, L. Kong, M. H. Nai, D. Liu, J. Wu, Y. Liu, S. Y. Chiam, W. K. Chim, C. T. Lim, B. Li, J. T. L. Thong and K. Hippalgaonkar, *Advanced Functional Materials*, 2017, **27**, 1702824.
380. Q. Hu, Z. Zhu, Y. Zhang, X.-J. Li, H. Song and Y. Zhang, *Journal of Materials Chemistry A*, 2018, **6**, 23417-23424.
381. C. F. Wu, T. R. Wei, F. H. Sun and J. F. Li, *Advanced Science*, 2017, **4**, 1700199.
382. W.-Y. Zhao, Z. Liang, P. Wei, J. Yu, Q.-J. Zhang and G.-S. Shao, *Acta Mater.*, 2012, **60**, 1741-1746.
383. K. Zhao, H. Duan, N. Raghavendra, P. Qiu, Y. Zeng, W. Zhang,

J. Yang, X. Shi and L. Chen, *Adv Mater*, 2017, **29**, 1701148.
384. T. W. Day, W. G. Zeier, D. R. Brown, B. C. Melot and G. J. Snyder, *Applied Physics Letters*, 2014, **105**, 172103.
385. L. P. Bulat, V. B. Osvenskii and D. A. Pshenay-Severin, *Materials Today: Proceedings*, 2015, **2**, 532-537.
386. M. Hong, Y. Wang, S. Xu, X. Shi, L. Chen, J. Zou and Z.-G. Chen, *Nano Energy*, 2019, **60**, 1-7.
387. H. Ju, M. Kim, D. Park and J. Kim, *Chem. Mater.*, 2017, **29**, 3228-3236.
388. E. Case, *J. Electron. Mater*, 2012, **41**, 1811-1819.
389. K. Biswas, J. He, I. D. Blum, C.-I. Wu, T. P. Hogan, D. N. Seidman, V. P. Dravid and M. G. Kanatzidis, *Nature*, 2012, **489**, 414-418.
390. G. A. Slack and S. Galginaitis, *Physical Review*, 1964, **133**, A253-A268.
391. M. Roufosse and P. G. Klemens, *Physical Review B*, 1973, **7**, 5379-5386.
392. P. Carruthers, *Reviews of Modern Physics*, 1961, **33**, 92-138.
393. G. Chen, T. Zeng, T. Borca-Tasciuc and D. Song, *Materials Science and Engineering: A*, 2000, **292**, 155-161.
394. P. G. Klemens, *Can J Phys*, 1957, **35**, 441-450.
395. G. Tan, F. Shi, S. Hao, L.-D. Zhao, H. Chi, X. Zhang, C. Uher, C. Wolverton, V. P. Dravid and M. G. Kanatzidis, *Nature Communications*, 2016, **7**, 12167.
396. Y. Zheng, X. Y. Tan, X. Wan, X. Cheng, Z. Liu and Q. Yan, *ACS Appl. Energy Mater.*, 2020, **3**, 2078–2089.
397. M. E. Launey and R. O. Ritchie, *Advanced Materials*, 2009, **21**, 2103-2110.
398. Y. Zheng, Q. Zhang, X. Su and X. Tang, *Acs Appl Mater Inter*, 2019, **11**, 40091-40098.
399. R. Schmidt, X. Fan, E. Case and P. Sarac, *J Mater Sci*, 2015, **50**, 4034-4046.
400. S. Wan, X. Huang, P. Qiu, S. Bai and L. Chen, *Mater Design*, 2015, **67:**, 379-384.
401. H. R. Williams, R. M. Ambrosi, K. Chen, U. Friedman, H. Ning, M. J. Reece, M. C. Robbins, K. Simpson and K. Stephenson, *Journal of Alloys and Compounds*, 2015, **626:**, 368-374.
402. N. Satyala, J. S. Krasinski and D. Vashaee, *Acta Materialia*, 2014, **74:**, 141-150.
403. S. Sarkar, X. Zhang, S. Hao, X. Hua, T. P. Bailey, C. Uher, C. Wolverton, V. P. Dravid and M. G. Kanatzidis, *ACS Energy Letters*, 2018, **3**, 2593-2601.
404. J. J. Kuo, M. Wood, T. J. Slade, M. G. Kanatzidis and G. J. Snyder, *Energy & Environmental Science*, 2020, **13**, 1250-1258.
405. Y. Zheng, G. Tan, Y. Luo, X. Su, Y. Yan and X. Tang, *Materials*, 2017, **10**, 617.
406. H. Wu, F. Zheng, D. Wu, Z.-H. Ge, X. Liu and J. He, *Nano Energy*, 2015, **13**, 626-650.
407. H. Tao, M. Zhou, R. Wang, K. Wang, S. Cheng and K. Jiang, *Advanced Science*, 2018, **5**, 1801021.
408. I. J. Beyerlein, M. J. Demkowicz, A. Misra and B. P. Uberuaga, *Progress in Materials Science*, 2015, **74**, 125-210.

Table of Contents

Defect engineering demonstrates great potential for enhancing both thermoelectric and mechanical properties of materials. In this review, the characterization methods of defects are briefly summarized. The recent advances and new insights resulting thereof in applying defect engineering to improving the thermoelectric performance and mechanical properties of inorganic materials are reviewed.